

**DEVELOPMENT OF A NEW ICTAL EEG SOURCE
IMAGING TECHNIQUE USING RECURSIVE APPROACH
FOR PRESURGICAL EVALUATION OF FOCAL EPILEPSY**

ABU HASNAT MOHAMMAD ASHFAK HABIB

**FACULTY OF ENGINEERING
UNIVERSITY OF MALAYA
KUALA LUMPUR**

2018

**DEVELOPMENT OF A NEW ICTAL EEG SOURCE
IMAGING TECHNIQUE USING RECURSIVE
APPROACH FOR PRESURGICAL EVALUATION OF
FOCAL EPILEPSY**

ABU HASNAT MOHAMMAD ASHFAK HABIB

**THESIS SUBMITTED IN FULFILMENT OF THE
REQUIREMENTS FOR THE DEGREE OF DOCTOR OF
PHILOSOPHY**

**FACULTY OF ENGINEERING
UNIVERSITY OF MALAYA
KUALA LUMPUR**

2018

UNIVERSITY OF MALAYA
ORIGINAL LITERARY WORK DECLARATION

Name of Candidate: ABU HASNAT MOHAMMAD ASHFAK HABIB

Registration/Matric No: KHA130077

Name of Degree: DOCTOR OF PHILOSOPHY

Title of Thesis: DEVELOPMENT OF A NEW ICTAL EEG SOURCE IMAGING
TECHNIQUE USING RECURSIVE APPROACH FOR
PRESURGICAL EVALUATION OF FOCAL EPILEPSY

Field of Study: MEDICAL INFORMATICS

I do solemnly and sincerely declare that:

- (1) I am the sole author/writer of this Work;
- (2) This Work is original;
- (3) Any use of any work in which copyright exists was done by way of fair dealing and for permitted purposes and any excerpt or extract from, or reference to or reproduction of any copyright work has been disclosed expressly and sufficiently and the title of the Work and its authorship have been acknowledged in this Work;
- (4) I do not have any actual knowledge nor do I ought reasonably to know that the making of this work constitutes an infringement of any copyright work;
- (5) I hereby assign all and every rights in the copyright to this Work to the University of Malaya ("UM"), who henceforth shall be owner of the copyright in this Work and that any reproduction or use in any form or by any means whatsoever is prohibited without the written consent of UM having been first had and obtained;
- (6) I am fully aware that if in the course of making this Work I have infringed any copyright whether intentionally or otherwise, I may be subject to legal action or any other action as may be determined by UM.

Candidate's Signature

Date:

Subscribed and solemnly declared before,

Witness's Signature

Date:

Name:

Designation:

**DEVELOPMENT OF A NEW ICTAL EEG SOURCE IMAGING
TECHNIQUE USING RECURSIVE APPROACH FOR PRESURGICAL
EVALUATION OF FOCAL EPILEPSY**

ABSTRACT

Electroencephalography source imaging (ESI) is a promising tool for localizing the cortical sources of both ictal and interictal epileptic activities. Although ictal EEG is difficult to analyze, it is believed to be more reliable than interictal ESI. Ictal ESI techniques can be categorized as Independent Component Analysis (ICA) based techniques and less stable non-ICA based classical techniques. Existing ICA-based techniques are highly dependent on visual inspection and user's feedback. This thesis presents the development of a new enhanced automatic ICA-based ictal ESI technique for epileptic focus localization in patients with refractory focal epilepsy. The proposed technique decomposes ictal EEG recursively, eliminates unwanted portion in every recursion cycle, and selects a significant ictal Independent Component (IC) at the final recursion cycle with the help of a unique quantitative feature of decomposed EEG. Back projected EEG is regenerated from that selected IC and epileptogenic focus is estimated from that regenerated EEG. Fifty sets of simulated ictal EEG and 8 patients' real ictal EEG were used for validation. Epileptogenic foci were estimated from those datasets by using the proposed technique and other two ICA-based techniques. Simulated-EEG-sources were compared with a known dipole location and real-EEG-sources were compared with the sites of successful surgery for the performance evaluation of the three techniques. Average distance of the estimated dipole from the original dipole for the proposed technique was 12.86 mm which was shorter than the half of the average distances for other two techniques. The real-EEG-sources estimated by the proposed technique were fully lateralized with the corresponding sites of surgery and the concordance rate (87.50%) was also higher than that of other two techniques (37.5%

and 12.55%). These findings show that the proposed ictal ESI technique may provide a cost-effective substitute for other costly diagnostic modalities.

Keywords: Epilepsy, Epileptogenic zone, Ictal EEG, Source localization, Independent component analysis.

University of Malaya

**PEMBANGUNAN TEKNIK ICTAL EEG SUMBER PENGIMEJAN YANG
BARU MENGGUNAKAN PENDEKATAN REKURSI UNTUK PENILAIAN
PRESURGICAL EPILEPSI FOCAL**

ABSTRAK

Pengimejan sumber electroencephalography (ESI) adalah alat terbukti berkesan untuk menyetempatan sumber kortikal kedua-dua aktiviti epilepsi ictal dan interictal. Walaupun EEG ictal adalah sukar untuk dianalisis, ictal ESI dipercayai lebih berkesan daripada interictal ESI. Teknik Ictal ESI boleh dikategorikan kepada teknik Analisis bebas Component (ICA) dan teknik klasik bukan ICA yang kurang stabil. Teknik berasaskan ICA yang sedia-ada amat bergantung pada pemeriksaan visual dan maklum balas pengguna. Tesis ini membentangkan pembangunan teknik ESI baru berasaskan teknik ICA ictal yang lebih automatik untuk epilepsi penumpuan penyetempatan pada pesakit dengan epilepsi tumpuan refraktori. Teknik yang dicadangkan merupakan uraian EEG ictal secara rekursif, yang menghapuskan bahagian yang tidak diinginkan dalam setiap kitaran rekursi, dan memilih ictal Komponen bebas (IC) yang ketara pada kitaran rekursi akhir dengan bantuan ciri kuantitatif unik daripada uraian EEG. Unjuran kebelakang EEG dijana semula daripada IC yang dipilih dan tumpuan epileptogenic adalah dianggarkan daripada EEG yang dibentuk semula. Lima puluh set EEG ictal simulasi dan ictal sebenar EEG daripada 8 pesakit telah digunakan untuk pengesahan. Tumpuan epileptogenic dianggarkan daripada set data tersebut dengan menggunakan teknik yang dicadangkan dan dua lagi teknik yang berasaskan ICA. Sumber-EEG daripada simulasi dibandingkan dengan satu lokasi dipole yang diketahui dan sumber-EEG-nyata pula dibandingkan dengan kawasan pembedahan yang berjaya untuk penilaian prestasi daripada tiga teknik tersebut. Jarak purata dipole-anggaran dari dipole-asal bagi teknik yang dicadangkan adalah 12.86 mm dan merupakan lebih pendek daripada separuh daripada jarak purata bagi dua teknik yang lain. Anggaran

sumber-EEG-nyata dengan teknik yang dicadangkan adalah lateralized sepenuhnya dengan kawasan pembedahan dan kadar konkordans (87.50%) juga lebih tinggi daripada dua teknik yang lain (37.50% dan 12.50%). Penemuan ini menunjukkan bahawa teknik ESI ictal yang dicadangkan boleh menjadi pengganti yang kos efektif untuk kaedah diagnostik mahal yang lain.

Kata kunci: Epilepsi, Zon epileptogenik, EEG ictal, Penyetempatan sumber, Analisis komponen bebas.

University of Malaya

ACKNOWLEDGEMENTS

All praise is to Allah, the Lord of the worlds, who gave me the opportunity and strength to accomplish this work.

I would like to express my sincere gratitude to my supervisors Prof. Ir. Dr. Fatimah Ibrahim, Prof. Dr. Lim Kheng Seang and Dr. Mas Sahidayana Mohktar for their constant support, invaluable guidance, and appreciable patience. Working with them have been a very fruitful learning and research experience. It was a great fortuity to work under their supervision as they always encouraged me to work hard and guided me with thoughtful advice and constructive comments.

My sincere gratitude also goes to my family members, namely, my parents, wife, brothers and sister for the unwavering love, heartfelt prayers, and unconditional sacrifices they have made to ensure the completion of this work. It would never have been possible for me to take this work to completion without their incredible support and encouragement.

I wish to thank my fellow lab-mates (Karunan Joseph, Aung Thiha, Bashar Yafouz, Mahdi Aeinehvand, Shah Mukim Uddin, and others) in the Centre for Innovation in Medical Engineering (CIME) and my colleague Mr. Tofael Ahmed for their valuable cooperation and moral support during these years of hard work.

This study is a part of the Malaysian Elders Longitudinal Research (MELoR) project which is funded by the High Impact Research (HIR) grant (UM.C/625/1/HIR/MOHE/ASH/02) from University of Malaya and Ministry of Higher Education (MOHE), Malaysia. I would like to extend my gratitude to these funding bodies and the principle investigator of the MELoR project, Prof. Dr. Shahrul Bahyah Kamaruzzaman, for supporting this study.

TABLE OF CONTENTS

Abstract	iii
Abstrak	v
Acknowledgements	vii
Table of Contents	viii
List of Figures	xii
List of Tables.....	xiv
List of Symbols and Abbreviations.....	xv
List of Appendices	xvii
CHAPTER 1: INTRODUCTION.....	1
1.1 Overview.....	1
1.2 Problem Statement.....	4
1.3 Thesis Objective	5
1.4 Scope of Work	6
1.5 Thesis Organization	7
CHAPTER 2: BACKGROUND AND LITERATURE REVIEW.....	8
2.1 Introduction.....	8
2.2 Physiological Origin of EEG	8
2.3 Overview of EEG Source Imaging Technique	12
2.3.1 Anatomical and Spatial Data Preprocessing	13
2.3.1.1 Head Model	13
2.3.1.2 Source Distribution Model	15
2.3.1.3 Channel Positions	16
2.3.2 Forward Solution	17

2.3.3	Functional Data Preprocessing	19
2.3.3.1	Artifact Rejection	20
2.3.3.2	Filtering	20
2.3.3.3	Regression	20
2.3.3.4	Blind Source Separation	21
2.3.3.5	Independent Component Analysis	22
2.3.3.6	Other Denoising Techniques	23
2.3.4	Inverse Solution	24
2.3.4.1	Parametric Methods	24
2.3.4.2	Non-parametric Methods	25
2.4	Software Tools for Realistic Head Model Generation	27
2.5	Ictal EEG Source Imaging	30
2.6	ICA Based Ictal EEG Source Imaging	33
2.7	Summary	35
CHAPTER 3: METHODOLOGY		37
3.1	Introduction	37
3.2	Outline of the Strategy	37
3.3	Primary Investigation on Various Aspects of Neurological Disorders	38
3.4	Software Tool Selection for Realistic Head Model Generation	39
3.4.1	Dataset	40
3.4.2	Comparison Based on Stated Features	40
3.4.3	Comparison Based on Real Data Analysis	40
3.5	Evaluation of the Clinical Utility of Ictal ESI Using Open-Source Tools	41
3.5.1	Patients	41
3.5.2	Anatomical Data Acquisition	42
3.5.3	Functional Data Acquisition	43

3.5.4	Nuclear Image Acquisition.....	43
3.5.5	Electroencephalographic Source Analysis	44
3.5.5.1	Data Pre-processing.....	44
3.5.5.2	Epoching and Averaging	44
3.5.5.3	Head Modelling.....	45
3.5.5.4	Source Localization.....	47
3.5.5.5	Stability of Estimated ESI Results	48
3.5.5.6	Performance Measure.....	49
3.6	Investigation of the Effects of Noise	49
3.6.1	Ictal EEG Generation	49
3.6.2	Decomposition of Ictal EEG	52
3.6.3	Dipole Source Localization of Independent Components.....	52
3.7	Design and Implementation of the RIDICS Technique.....	53
3.7.1	A Quantitative Feature of Ictal EEG Decomposition.....	53
3.7.2	Recursive ICA Decomposition for Ictal Component Selection	56
3.7.3	Simulated Ictal-EEG Generation.....	59
3.7.4	Validation Using Simulated Data.....	62
3.7.5	Patients and data acquisition	63
3.7.6	Validation Using Real Data.....	64
CHAPTER 4: RESULTS AND DISCUSSIONS		66
4.1	Introduction.....	66
4.2	Comparison of Software Tools for Head Model Generation.....	66
4.2.1	Comparison Based on Stated Features	66
4.2.2	Comparison Based on Real Data Analysis	67
4.2.3	Head Modelling Tool Selection.....	71
4.3	Clinical Utility of Ictal ESI.....	72

4.3.1	Source Estimation.....	72
4.3.2	Inverse Solution Selection.....	75
4.3.3	Stability Analysis	76
4.3.4	Analysis of Findings.....	76
4.3.5	Advantages of Ictal ESI over Ictal SPECT.....	77
4.4	Effects of Noise on the Features of Decomposed Ictal EEG.....	78
4.4.1	Topographic Maps.....	78
4.4.2	Activity Power Spectra.....	80
4.4.3	Dipole Residual Variance.....	80
4.4.4	Findings of Noise-Effect Analysis	81
4.5	Validation Results of the RIDICS Technique	82
4.5.1	Validation of RIDICS Technique Using Simulated Data	82
4.5.2	Validation of RIDICS Technique Using Real Data	84
4.5.3	Analysis of Outcomes	87
4.6	Summary.....	93
CHAPTER 5: CONCLUSION AND FUTURE WORK		96
5.1	Conclusion	96
5.2	Summary of Contributions	98
5.3	Limitations.....	98
5.4	Recommendation for Future Work.....	100
References		101
List of Publications and Papers Presented		114
Appendix		121

LIST OF FIGURES

Figure 2.1: Schematic representation of a neuron.....	9
Figure 2.2: Electrochemical process of information transmission between neurons.....	10
Figure 2.3: Neuron modelled as a current dipole. (a) The directions of the primary current and secondary current in a neuron. (b) A pair of current sink and current source and their equivalent current dipole.....	11
Figure 2.4: Block diagram of basic ESI technique.	12
Figure 2.5: Single-shell, two-shell, three-shell, and four-shell spherical head models. .	14
Figure 2.6: (a) MRI scan of a subject. (b) BEM meshes of brain, skull and scalp of the same subject.	15
Figure 2.7: Volumetric Source Distribution.....	16
Figure 2.8: (a) Head model and template electrodes without being aligned. (b) Electrodes and the head model after manual alignment.....	17
Figure 2.9: Scalp potentials as a mixture of the cortical source potentials.	21
Figure 3.1: Workflow diagram that shows the major steps in developing the improved ESI technique.	38
Figure 3.2: Ictal epochs acquisition. (a) Ictal EEG of patient 2, (b) Power spectrum density in the region of interest, (c) EEG segment of interest with centre time points of selected epochs. The channel highlighted in <i>red</i> is the prominent channel.	46
Figure 3.3: Average maps of selected ictal (a) and interictal (b) EEG events of patient 1. Highlighted channel holds the highest amplitude and the time duration from t_1 to t_2 is considered as the event duration. Estimated source at t_0 has been used for final result analysis while stable results have been obtained for all the time points between t'_1 and t'_2	48
Figure 3.4: (a) Three different views of dipole location and orientation. (b) Source waveform. (c) 2D topographic map.	50
Figure 3.5: (a) Noise free simulated EEG (N0). (b) Simulated EEG (N10) with coherent noise.	51
Figure 3.6: (a) Equivalent dipole sources for the ICs of noise free EEG set N0. (b) Equivalent dipole sources for the ICs of N10 having 1 μ V of noise.	53
Figure 3.7: Simplified flow chart of RIDICS technique.	57

Figure 3.8: (a) Three different views of the location and orientation of the dipole. (b) Changes of MSE signals with the increase of added noises. (c) The SNRs (in decibel) of the MSE signals of the simulated EEG datasets.	60
Figure 4.1: MRI scan of a subject (3rd dataset).	69
Figure 4.2: Surfaces generated from 3rd MRI dataset.	70
Figure 4.3: SPECT results and corresponding ESI results of two patients (patient 2 and patient 3). ESI sources, estimated by using volumetric source space and surface source space, have been presented on magnetic resonance imaging and simulated cortical surfaces respectively. Cortical regions with red color represent the estimated epileptic foci.....	73
Figure 4.4: 2D topographic maps for all the ICs of (a) N0 and (b) N10. Locations and orientations of corresponding equivalent dipole sources are shown. Color bars next to the maps indicate the magnitude and polarity.....	79
Figure 4.5: Activity power spectrum for (a) IC1 of N0 and (b) IC2 of N100.	80
Figure 4.6: (a) Dipole residual variances of all the ICs of all the EEG data sets. (b) Changes of average residual variances with noise levels.....	81
Figure 4.7: Euclidean distance between the original current dipole location D and the estimated current dipole location D_{BIC} , modeled from each BIC.	82
Figure 4.8: Zero-lag cross-correlation values that were estimated between noiseless dataset E and each back-projected dataset E_{BIC} regenerated from the BIC of each simulated ictal EEG dataset.	83
Figure 4.9: Independent Component time-courses of E_{23} dataset and the topographic maps of the BICs (highlighted with Magenta) obtained from (a) the RIDICS technique, (b) the PSDICS technique, and (c) the TFRICS technique.	88
Figure 4.10: Independent Component time-courses of E_{41} dataset and the topographic maps of the BICs (highlighted with Magenta) obtained from (a) the RIDICS technique, (b) the PSDICS technique, and (c) the TFRICS technique.....	89
Figure 4.11: Euclidean distance between the locations of D and D_{BIC} for the modified implementation of RIDICS, PSDICS and TFRICS techniques.	91
Figure 4.12: Zero-lag cross-correlation values that were estimated between E and E_{BIC} for the modified implementation of RIDICS, PSDICS and TFRICS techniques.	91
Figure 4.13: Execution time required for every ICA-decomposition.	92

LIST OF TABLES

Table 3.1: Demographics and Clinical Characteristics.	42
Table 3.2: Demographics and diagnosis results of the patients.	64
Table 4.1: System requirements of the selected tools.	67
Table 4.2: Input and output file formats.	68
Table 4.3: Cortical locations of MRI lesions, SPECT-foci and the ESI-foci of all the patients.	74
Table 4.4: Concordance or discordance of ESI results with ictal SPECT.	75
Table 4.5: Surgery sites and corresponding epileptic foci estimated by 3 ESI techniques and for 8 patients. Red cortical areas denote ictal EEG source analyzed using various techniques.....	85
Table 4.6: Concordance or discordance of ESI results with surgery sites	86

LIST OF SYMBOLS AND ABBREVIATIONS

A	:	Mixing matrix
a	:	A column of matrix A
BEM	:	Boundary element method
dSPM	:	Dynamic Statistical Parametric Mapping
EEG	:	Electroencephalogram
ESI	:	Electroencephalogram source imaging
\mathcal{F}	:	Discrete Furrier transform outcomes
f	:	Ictal rhythm frequency
f_s	:	Sampling frequency
GFP	:	Global field power
IC	:	Independent component
ICA	:	Independent component analysis
k	:	Index of discrete values in frequency domain
MEG	:	Magnetoencephalography
MRI	:	Magnetic resonance imaging
MTS	:	Mesial Temporal Sclerosis
m	:	Number of independent components
n	:	Number of electrodes
PSD	:	Power spectral density
PSDICS	:	PSD-based ictal component selection
p	:	Index of independent component
q	:	Index of EEG electrode
RIDICS	:	Recursive ICA-decomposition for ictal component selection
sLORETA	:	Standardized low-resolution brain electromagnetic tomography

SNR	:	Signal-to-noise ratio
SPECT	:	Single-photon emission computed tomography
T	:	Number of samples in EEG signals
t	:	Index of discrete values in time domain
t_0	:	Examination time point
\mathbf{U}	:	IC time course
\mathbf{u}	:	A row of matrix \mathbf{U}
wMNE	:	Weighted minimum norm estimate
\mathbf{X}	:	EEG dataset
\mathbf{X}^p	:	Back projected EEG from p^{th} IC
\mathbf{x}_q^p	:	EEG signal of q^{th} electrode in \mathbf{X}^p
\mathbf{Y}	:	Input rhythm magnitude
\mathbf{Y}^p	:	Back-projected rhythm magnitude
\mathbf{Z}	:	Zero-lag cross-correlation between \mathbf{Y} and each of \mathbf{Y}^p matrices

LIST OF APPENDICES

Appendix A: Data Used for Producing Figure 4.7 & Figure 4.8.....	121
Appendix B: MATLAB Code for Implementing the RIDICS Technique with Simulated Ictal EEG Data.....	122
Appendix C: MATLAB Code for Implementing the PSDICS Technique with Simulated Ictal EEG Data.....	132
Appendix D: MATLAB Code for Implementing the TFRICS Technique with Simulated Ictal EEG Data.....	136

CHAPTER 1: INTRODUCTION

1.1 Overview

Epilepsy is a common chronic neurological disorder that affects people of all ages. Around 65 million people worldwide have epilepsy (Moshe, Perucca, Ryvlin, & Tomson, 2015; Ngugi, Bottomley, Kleinschmidt, Sander, & Newton, 2010; Thurman et al., 2011). It refers to chronic, recurrent, unprovoked seizure that is defined as “a transient occurrence of signs and/or symptoms due to abnormally excessive or synchronous neuronal activity in the brain” (Fisher et al., 2005). Depending on the involved cortical areas, it is commonly divided into two broad divisions: generalized epilepsy (involves the whole cortex) and partial or focal epilepsy (provoked by limited brain regions, the so-called epileptogenic zone or epileptic foci). Focal epilepsy is the most common form of epilepsy (approximately 60% of all epilepsy) and around 15% of all focal epilepsy are uncontrolled or of the refractory type (Rosenow & Luders, 2001). Around half of the patients with refractory focal epilepsy (Engel, 1993), i.e. approximately 4.5% of all patients with epilepsy, are potential candidates for surgical resection (Rosenow & Luders, 2001). The goal of epilepsy surgery is to resect or disconnect the epileptogenic zone completely (Brodbeck et al., 2011) and the success of surgery depends largely on the proper localization of epileptogenic zone. Therefore, precise localization of epileptogenic zone is obligatory for seizure freedom.

Different diagnostic techniques, such as non-invasive scalp electroencephalogram (EEG), intracranial EEG (iEEG), magnetoencephalography (MEG), magnetic resonance imaging (MRI), functional magnetic resonance imaging (fMRI), positron emission tomography (PET), and single photon emission computed tomography (SPECT) are used for the presurgical evaluation of focal epilepsy. These techniques are used to identify and measure the epileptogenic zone, as defined in (Luders, Najm, Nair, Widdess-Walsh, & Bingman, 2006). Among all these techniques, scalp EEG is used

most commonly for epilepsy evaluation because of its high temporal resolution, suitability for long-term monitoring, non-invasiveness and low cost.

The widely accepted diagnostic technique, EEG, measures and records the scalp potentials resulting from the neuronal ionic current flow within the brain. These scalp potentials contain valuable information about the underlying cerebral electromagnetic sources of the observed EEG events. In case of any epileptic EEG event, the corresponding cerebral source resembles the epileptogenic zone. Proper identification of such cortical sources of EEG is crucial for the diagnosis and management of various neurological disorders and also for the understanding of the brain functions in neuroscience research. Traditionally, EEG recordings are interpreted through visual inspection. Such interpretations of scalp EEG often are misleading, because they follow the simplistic principle that the electrodes recording the clearest epileptic event overlie the seizure focus (Assaf & Ebersole, 1997) and do not consider the volume conduction effect that arises due to the series of layers: scalp, skull, cerebrospinal fluid (CSF), etc. (He & Ding, 2013; Nunez & Srinivasan, 2006). Simple visual inspection of EEG is therefore not adequate for the precise localization of the epileptogenic zone.

Electroencephalogram source imaging (ESI) is comparatively a new model-based computational technique that can localize and depict the possible cortical sources of EEG activities (Kaiboriboon, Lüders, Hamaneh, Turnbull, & Lhatoo, 2012). It is a multilayer head model-based EEG source localization solution that considers the volume conduction effect and can use different conductivities for different head layers. It utilizes both temporal and spatial aspects of scalp EEG to estimate their underlying cortical sources. Visual interpretation of EEG provides a coarse approximation of the underlying cortical sources, whereas ESI can provide a more refined sublobar prediction of the cerebral origin of scalp EEG (Assaf & Ebersole, 1997; Koessler et al., 2010).

Furthermore, ESI can provide information on corticocortical propagation during the short period of an interictal spike or seizure onset that is not easily obtained from the traditional visual inspection of the EEG waveforms. Due to the above-mentioned advantages of ESI over conventional visual inspection method, ESI is considered as a promising tool for localizing the cortical sources of EEG events.

This promising diagnostic tool (i.e. ESI) has important applications in both cognitive neuroscience and clinical neuroscience. The cognitive neuroscience utilizes ESI techniques mostly for investigating the temporal aspects of neural processing by analyzing event related potentials (Michel et al., 2004). The state and progression (i.e. cognitive decline) of a common cognitive disorder, Alzheimer's disease, can be evaluated by ESI analysis of the resting state EEG rhythms (Babiloni et al., 2007; Babiloni et al., 2014). The clinical neuroscience includes neurology, psychiatry psychopharmacology, etc. It uses ESI for analyzing the sources of sensory or motor evoked potentials, for localizing the EEG sources in certain frequency bands, but most often for localizing the epileptogenic zones from the epileptic EEG events (Michel et al., 2004).

Two different types of epileptic events can be recorded through two varieties of scalp EEGs that are known as ictal EEG and interictal EEG. The scalp EEG recorded during a seizure, which is a sudden surge of electrical activity in the brain that lasts for several seconds to a few minutes and is characterized by rhythmic activities, is known as ictal EEG. Interictal EEG is recorded in between seizures and contains both normal neural activities and brief epileptic events (known as interictal spikes) that occur in irregular intervals. Both ictal and interictal EEG can be analyzed independently (or jointly) for ESI-based epileptogenic cortical source estimation, but both have their corresponding pros and cons.

Ictal EEG measures cortical seizure discharges superposed with large amount of artifacts, external noises and other background brain oscillations (Urrestarazu et al., 2004). These unwanted portions of ictal EEG decrease its Signal to Noise Ratio (SNR). Such low SNR values makes ictal-EEG-based source imaging (i.e. ictal ESI) highly challenging (Kaiboriboon et al., 2012), although ictal EEG contains valuable information regarding the underlying epileptogenic zone. On the contrary, interictal EEG contains less noise, but interictal-spike-origin can be separate from the epileptogenic zone (Rosenow & Luders, 2001) and the obtained source may not reflect the actual source because of the fast propagation of interictal epileptiform activity (Wennberg, Valiante, & Cheyne, 2011). Therefore, ictal EEG is believed to be more reliable than interictal EEG for epileptogenic zone localization (Jayakar, Duchowny, Resnick, & Alvarez, 1991).

1.2 Problem Statement

The major obstacle for ictal ESI is to eliminate the unwanted portions of the ictal EEG before using it for source estimation. Various tools and techniques including digital filters, averaging of the ictal events, ICA and principal component analysis (PCA) have been used to increase the SNR of ictal EEG. Among all those techniques, ICA is the most useful tool for separating the unwanted portions of ictal EEG. It uses a statistical technique to decompose a mixed dataset into a set of statistically independent components (ICs). In the context of EEG signals, ICA can decompose each set of EEG into a series of spatially fixed and temporally independent components (Yang, Wilke, Brinkmann, Worrell, & He, 2011). Independent components from extracerebral origin (e.g. muscle artifacts, eye movements, and power line noise, etc.) are removed for denoising (McMenamin et al., 2010), whereas the components that display ictal nature (i.e. the ictal components) are extracted for epileptogenic zone localization. Proper identification of such ictal component(s) is the major challenge for ICA-based ictal ESI

techniques. All the existing ictal ESI techniques are highly dependent on visual inspection process for selecting the ictal component(s). In this context, it becomes an important and interesting issue to develop an improved ictal ESI technique with less dependency on visual inspection.

1.3 Thesis Objective

The objective of this thesis is to develop a new ICA-based ictal ESI technique that uses recursive approach for automatic identification of ictal component, which leads to better estimation of epileptogenic zone and therefore has potential application in the presurgical evaluation of refractory focal epilepsy. To accomplish this key objective the following sub-objectives are pursued:

- I. To implement a classical ictal ESI technique with open-source or free software tools for examining their clinical utility for epileptic zone localization in patients with refractory focal epilepsy and for selecting the suitable tools for the proposed technique.
- II. To develop and implement a new ICA-based ictal ESI technique by using those selected software tools and a unique quantitative feature of decomposed ictal EEG, so that the proposed technique reduces the dependability on visual inspection for ictal component selection, as well as for better estimation of epileptogenic zone.
- III. To evaluate the practicality and clinical usability of the proposed ictal ESI technique by using both simulated ictal EEG datasets and real ictal EEG datasets that were recorded in a conventional clinical setup.

1.4 Scope of Work

This study focused on the presurgical evaluation of focal epilepsy only. Utilization of ESI for other diseases, such as generalized epilepsy (Holmes, Brown, & Tucker, 2004) and Alzheimer's diseases (Babiloni et al., 2007), are out of the scope of this work.

This thesis utilized ictal EEG and developed an improved ictal EEG based source imaging technique. Interictal EEG based source imaging was used for comparative analysis only.

Instead of MEG based source imaging, this study considered EEG based source imaging. Although, MEG is an available epilepsy diagnosis technique and the principles of ESI apply equally to the MEG-based source imaging (Plummer, Harvey, & Cook, 2008), MEG-based source imaging is not within the scope of this study. Advantages of Ictal ESI over MEG-Based Source Imaging are listed in (Habib et al., 2016).

The terms *source localization* and *source imaging* are often used interchangeably (Kaiboriboon et al., 2012; Michel et al., 2004), but some articles (Mosher, Baillet, & Leahy, 1999; Scherg, 1994) distinguish them based on the source model used in the analysis. A small set of current dipoles with unknown locations and moments are considered as the source model for the source localization techniques, whereas the source imaging techniques consider a large number of current dipoles with fixed locations and orientations. This thesis mostly focused on the so called source imaging techniques. However, similar to the relevant literatures, both the terms (source localization and source imaging) were used interchangeably.

Accuracy of an ESI technique can be improved by using high density EEG (Lantz, Grave de Peralta, Spinelli, Seeck, & Michel, 2003), but the standard medical EEG systems comprise between 19 and 32 electrodes (Becker, 2014). This study focused on

developing an ESI technique that supports both low density and high density EEG and performs better with low density EEG.

1.5 Thesis Organization

The rest of the thesis is organized as follows:

Chapter 2 presents a literature review starting from the fundamentals to the pros and cons of modern ictal ESI techniques. It describes the physiological origin of scalp EEG and presents an outline of the basic ESI technique. It also examines the expanding research literature and provides an overview of the recent research findings on the ictal ESI. At the end of this chapter, an issue related to the present state of ESI is presented.

Chapter 3 describes the research methodology and procedures to accomplish the defined objectives. It includes the major steps for the development of the proposed improved ESI technique for the noninvasive presurgical evaluation of refractory focal epilepsy.

Chapter 4 presents the research findings that include the discussion on the results that obtained in this study. The results are organized according to the sequence of the major steps discussed in chapter 3.

Chapter 5 presents an overall conclusion, along with a summary of the original contribution. After that, few limitations of the current project are highlighted. Finally, some suggestions for possible future work are proposed.

CHAPTER 2: BACKGROUND AND LITERATURE REVIEW

2.1 Introduction

The German psychiatrist Hans Berger invented EEG around 90 years ago (Berger, 1929; Khanna, Pascual-Leone, Michel, & Farzan, 2015). Since then, the clinical use of EEG, especially in the evaluation of epilepsy, has increased exponentially. History of ESI is almost as old as that of EEG (Jayakar et al., 1991) because the art of localization was initially described in 1934 (Adrian & Matthews, 1934; Compston, 2009). A large number of studies have already been carried out but the ESI problem is still open for finding more reliable solution with better accuracy. The reason behind this long investigation lies in the proof of Helmholtz (Helmholtz, 1853). He proved that an active current source of a particular position inside a conductive medium can produce unique potential on the outer surface of the medium, but the same surface potential can be obtained for an infinite number of internal locations of such current sources. So finding a unique source in the brain from a given potential map on the scalp is not a trivial problem. Acceptable solutions can be obtained through proper a priori assumptions of the source space and the volume conductor. This chapter describes the physiological origin of scalp EEG and presents an overview of the basic ESI technique. It also examines the expanding research literature and provides an exhaustive review of the recent research findings on the ictal ESI with emphasis on the ICA based ictal ESI techniques.

2.2 Physiological Origin of EEG

The brain serves as the center of the nervous system and processes a large amount of information with the help of billions of nerve cells (Pelvig, Pakkenberg, Stark, & Pakkenberg, 2008), namely neurons and glial cells. Neurons are the core components of the brain. These cells are electrically excitable and can process as well as transmit information by using electrochemical signals. A typical neuron consists of three parts:

dendrite, soma and axon (see Figure 2.1). The dendrites receive stimuli from thousands of other cells. The cell body, known as soma, contains the nucleus. The axon transmits the electrochemical nerve impulses through the neuron. The connection points at which stimuli are transmitted between the axon of one neuron and the dendrites of neighboring neurons are called synapses.

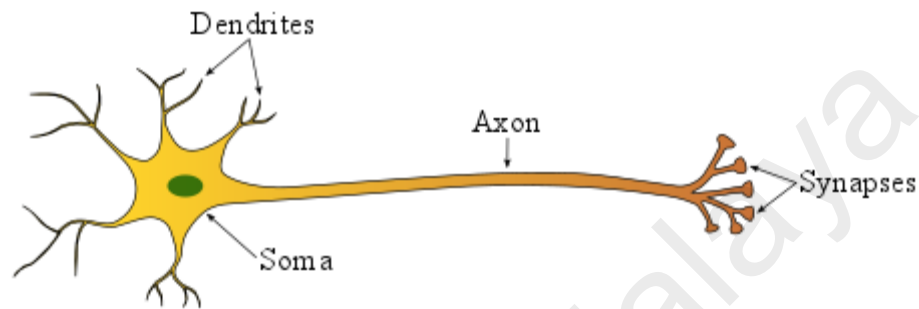


Figure 2.1: Schematic representation of a neuron.

Neurons communicate through an electrochemical process as illustrated in Figure 2.2. The presynaptic neuron releases neurotransmitters due to the excitations from other cells. The neurotransmitters then bind to the receptors at the dendrites of the neighboring neurons (the postsynaptic neuron) and enables ions to get into the postsynaptic neuron through its ion channels. These ions increase the electric potentials at the cell membranes of the postsynaptic neuron. Once the electric potential reaches a certain threshold value, a so-called action potential is generated and an electric impulse is sent along the membrane of the axon. It triggers the release of more neurotransmitters. These neurotransmitters then bind to the next postsynaptic neurons and lead to a change of the post-synaptic potentials at the postsynaptic cell membranes and so on.

An interior current flows within each postsynaptic cell due to the post-synaptic potentials. This current is called the intra-cellular (or primary) current. In order to counterbalance this current another current (extra-cellular or secondary) flows outside

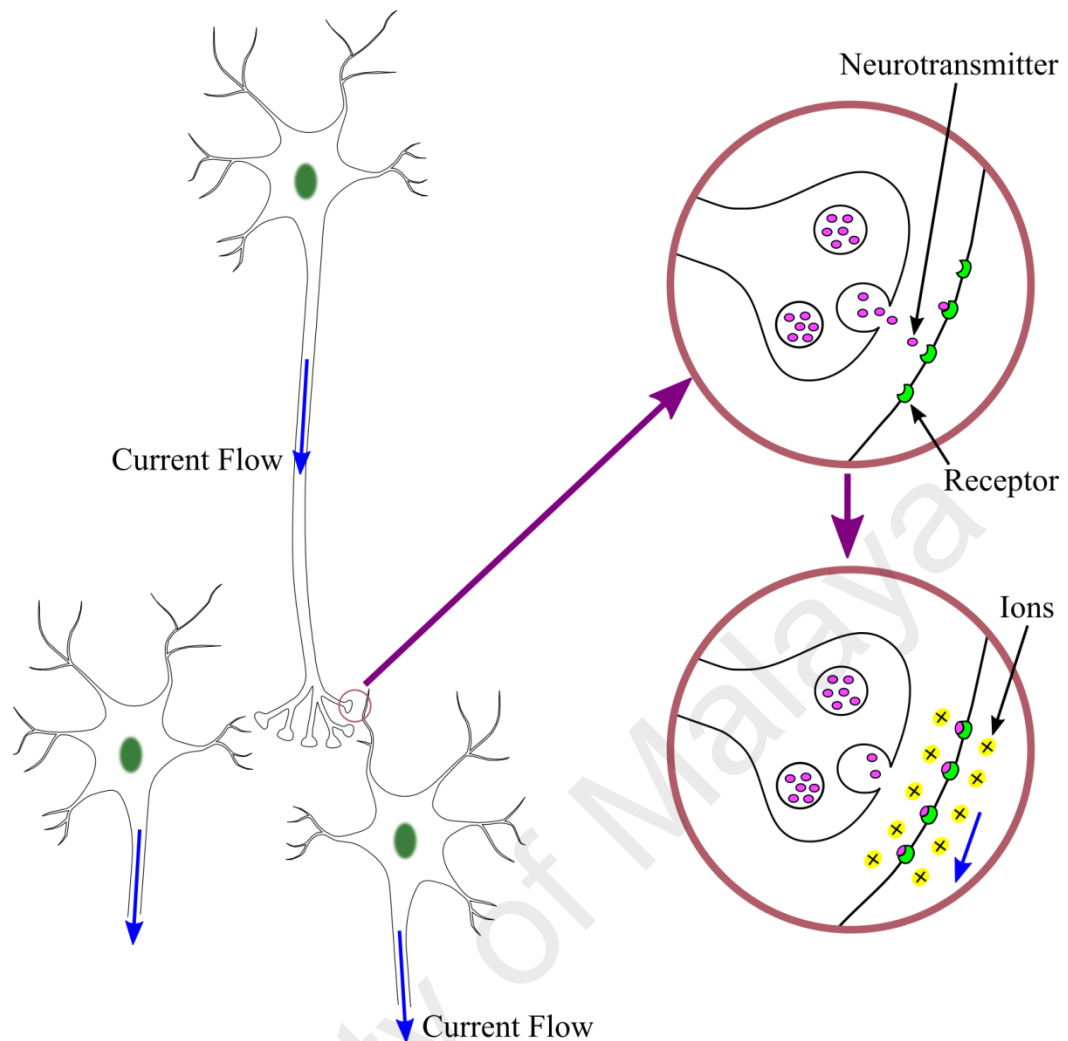


Figure 2.2: Electrochemical process of information transmission between neurons.

the cell membrane and in the opposite direction. Figure 2.3a illustrates the intra-cellular and extra-cellular currents of a neuron. Extra-cellular current causes electric potential at the surface of the head. More negative extracellular environment occurs at the synapse end while the axonal end of the postsynaptic neuron becomes more positive. Therefore, the synapse end and the axonal end are considered as the current sink and current source respectively. Such a pair of current sink and source can be modeled by a current dipole as illustrated in Figure 2.3b, which is oriented along the dendrite of the cell, and constitutes the basis for mathematical models of brain activity (Hallez et al., 2007).

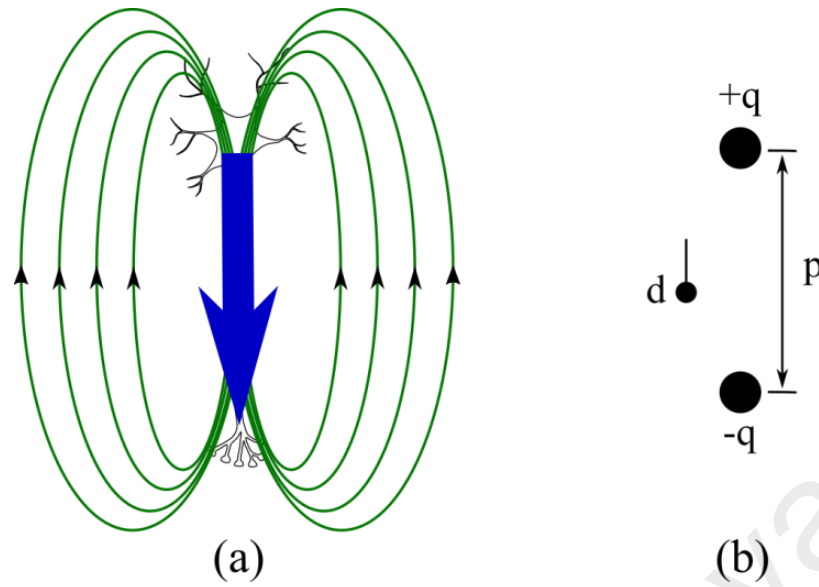


Figure 2.3: Neuron modelled as a current dipole. (a) The directions of the primary current and secondary current in a neuron. (b) A pair of current sink and current source and their equivalent current dipole.

If the point charges $+q$ and $-q$ are accumulated in the source and sink respectively and if they are separated by a distance p then the magnitude d of the dipole moment \mathbf{d} is the product of q and p . If a unit vector \mathbf{e} represents the direction of the dipole moment, which is directed from the sink to the source, then \mathbf{d} can be expressed as:

$$\mathbf{d} = dq\mathbf{e} \quad (2.1)$$

The amplitude of current in a single neuron is very small and therefore a current dipole represents the synchronized activity of a group of neurons localized to a small cortical region. For producing detectable potential on the scalp thousands or millions of neurons should act synchronously and they should have similar spatial orientation (Nunez & Srinivasan, 2006). It is commonly believed that the neurons that are responsible for producing scalp potential are located in the gray matter and are oriented perpendicular to the cortical surface (Becker, 2014).

2.3 Overview of EEG Source Imaging Technique

The aim of ESI is to identify the cortical regions that are responsible for producing electrical potentials on the scalp. It deals with the solutions for two fundamental problems: forward problem and inverse problem (Hallez et al., 2007; Jatoui, Kamel, Malik, Faye, & Begum, 2014; Plummer et al., 2008). The forward problem involves the estimation of scalp potentials from the given current sources in the brain. These estimated potentials are necessary to solve the inverse problem that identifies the unknown cortical current sources from the recorded scalp potentials (i.e. the EEG). Other than finding the solutions for forward and inverse problems, ESI techniques also need preprocessing of the functional and structural data. A block diagram of a basic ESI technique is illustrated in Figure 2.4.

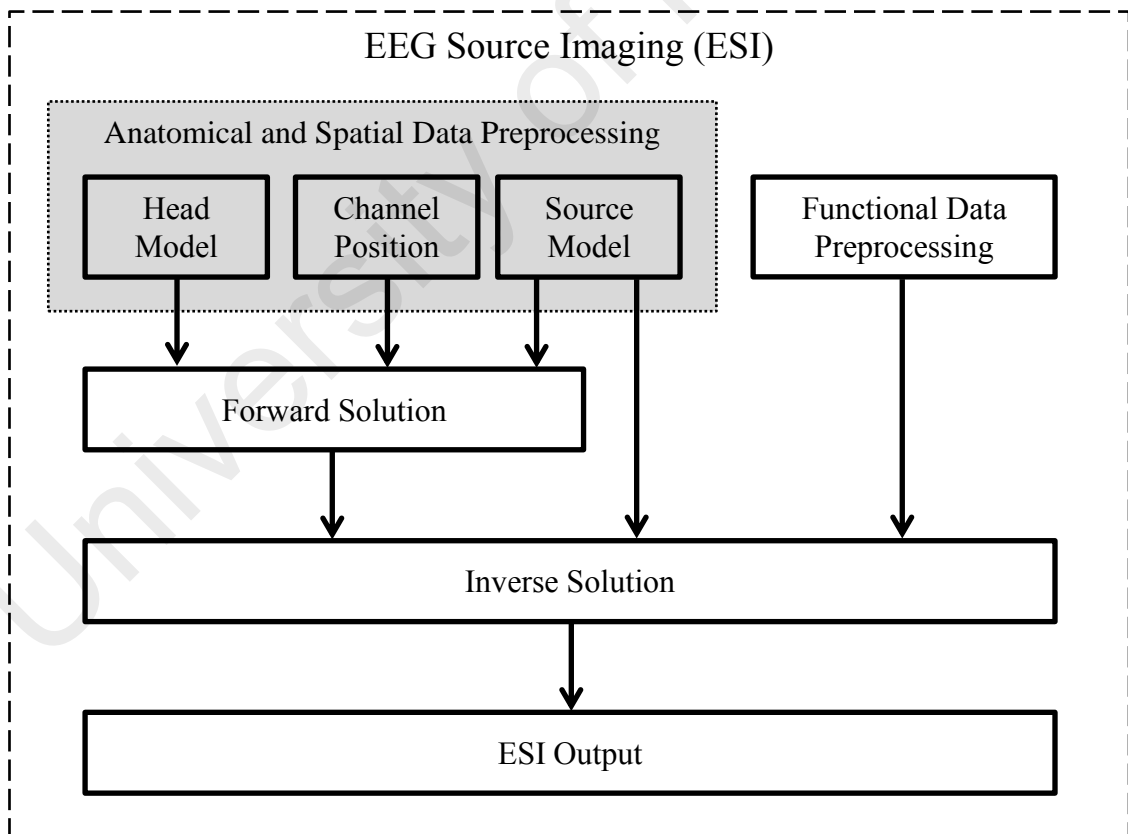


Figure 2.4: Block diagram of basic ESI technique.

2.3.1 Anatomical and Spatial Data Preprocessing

In order to solve the forward problem a structural model of subject's head, the locations of the known sources inside the head volume, and the EEG electrodes positions on the head surface are required. These anatomical and spatial data need to be preprocessed before use in forward solution. The techniques for preprocessing these three sets of data are discussed below.

2.3.1.1 Head Model

An appropriate computer generated head model is required for connecting the neuronal electrical activities to the scalp potentials. Mainly two types of head models, spherical and realistic, are used for EEG source estimations (Kaiboriboon et al., 2012; Rosenfeld, Tanami, & Abboud, 1996).

(a) *Spherical Head Model*

The simplified form of head model consists of one or more homogeneous spheres or shells (Fiederer et al., 2016; Frank, 1952). The simplest form of such spherical head model contains only one shell and it assumes uniform conductive throughout the head volume. Since the assumption is unrealistic, the accuracy of single shell head model-based EEG source estimation is limited (Kaiboriboon et al., 2012). Another form of spherical head model, which consists of multiple overlapping concentric shells, is non-homogeneous type. It considers the non-homogeneities of the layers of human head. The overall performance of spherical head model-based ESI solution can be improved by considering multiple shell model and local anisotropies (Kaiboriboon et al., 2012). Single shell model represents the brain whereas a multiple shell model represent different layers of human head, namely brain, CSF, skull, and scalp (Plummer et al., 2008). These spherical head models are illustrated in Figure 2.5. The volume within the inner shell or within two adjacent shells is considered isotropic. The main advantage of

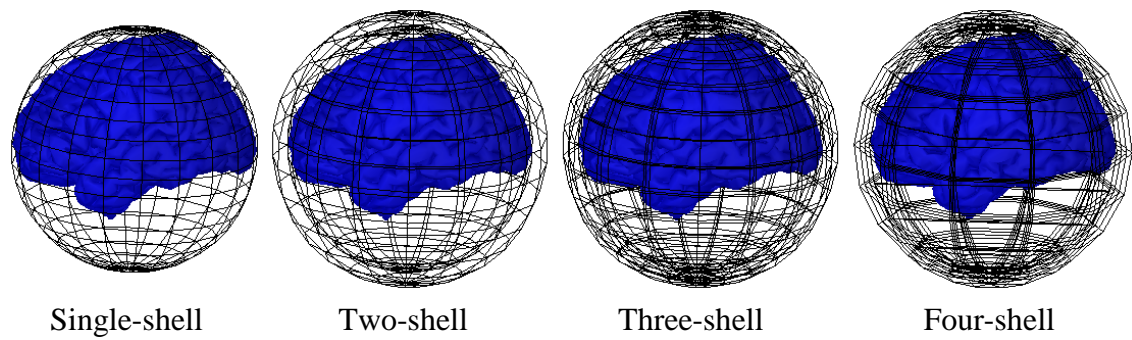


Figure 2.5: Single-shell, two-shell, three-shell, and four-shell spherical head models.

the spherical model is its simplicity. Moreover, spherical head models provide an opportunity to solve the forward problem analytically (Ary, Klein, & Fender, 1981; Koles, 1998).

(b) ***Realistic Head Model***

High-resolution MRI scans of individual patients are used for generating the subject specific realistic head models. These sophisticated models can offer better ESI solutions with respect to the spherical-model-based solutions because real heads are not spherical (Kaiboriboon et al., 2012). Several comparative studies claimed that realistic head models were inevitable to ensure accurate EEG source estimation (Cuffin, 1996; Hämäläinen & Ilmoniemi, 1994; Meijs, Bosch, Peters, & Da Silva, 1987; Menninghaus, Lutkenhoner, & Gonzalez, 1994; Roth, Balish, Gorbach, & Sato, 1993; Stok, 1987; Thevenet, Bertrand, Perrin, Dumont, & Pernier, 1991; Yvert, Bertrand, Echallier, & Pernier, 1995). Three different realistic head models are used with three popular numerical techniques, namely boundary element method (BEM), finite element method (FEM), and finite difference method (FDM) (Kaiboriboon et al., 2012). All these techniques require segmentation of the head volume into various head layers. The first technique uses a geometric model that triangulates the surfaces of the segmented layers and considers isotropic conductivity for each layer (Hämäläinen & Sarvas, 1989; He et al., 1987). The second technique allows tessellation of the segmented head layers and

thus can consider individual anisotropic conductivity for each layer (Michel et al., 2004; Miller & Henriquez, 1990). The third technique can also consider anisotropic conductivity. It divides the head volume into cubic grids so that different cubic element can hold different conductivity (Kaiboriboon et al., 2012; Lemieux, McBride, & Hand, 1996).

Although FEM and FDM provide more realistic models, these methods consume more computation time and memory (Hallez et al., 2007). Therefore the implementation of FEM and FDM toolboxes are mostly done in experimental level. In this context BEM generated head models were mostly used in the ESI based clinical studies. An MRI scan of a subject and the corresponding realistic BEM meshes are illustrated in Figure 2.6.

2.3.1.2 Source Distribution Model

Most of the EEG source estimation techniques require an explicit definition of a source model that describes the locations and orientations of a set of current dipole sources. These source models are taken into consideration during source estimation. Various hypotheses on the number, location, orientation, and magnitude of the dipole

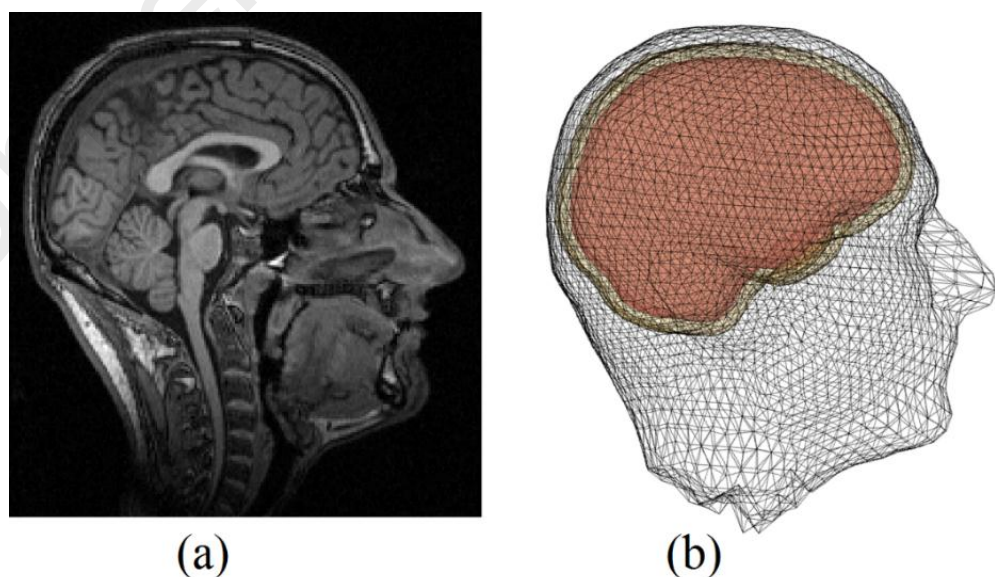


Figure 2.6: (a) MRI scan of a subject. (b) BEM meshes of brain, skull and scalp of the same subject.

sources can be raised (De Munck, 1990; Grech et al., 2008; Rodríguez-Rivera, Van Veen, & Wakai, 2003) and, based on the location of dipole sources, the suggested source models can be categorized into two types: volumetric (or pointwise) source models and surfacic source models. The volumetric (or pointwise) source models define the dipole positions on a 3-dimensional grid (sometimes as shown in Figure 2.7), whereas the surfacic source models define the source distribution over a 3-dimensional mesh surface (typically on the cortical surface) (Gramfort, Papadopoulos, Olivi, & Clerc, 2011).

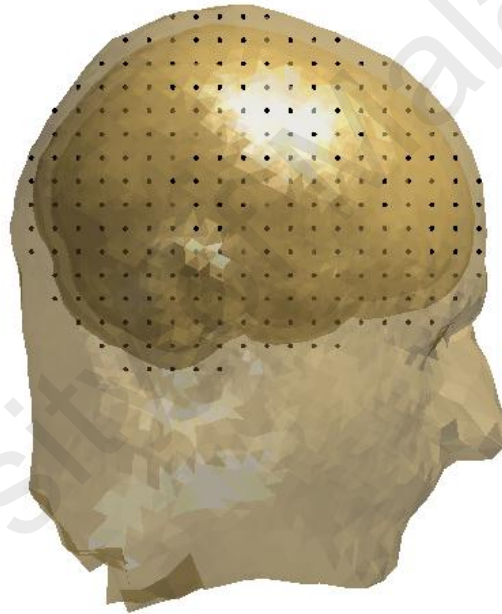


Figure 2.7: Volumetric Source Distribution.

2.3.1.3 Channel Positions

The cortical sources are estimated relative to the scalp electrode positions and precise source estimation requires the exact positions of electrodes in the digitized form (Wang & Gotman, 2001). Commercial 3D digitizer, such as Polhemus FASTRAK, can acquire the digitized locations of EEG electrodes, but due to high cost and rare use in conventional EEG data acquisition, very few studies used such commercial digitizer. An

alternate solution, that is well accepted, is to use the template sets of digitized electrode-positions with necessary alterations.

Moreover, accurate source estimation requires co-registration of all the geometrical descriptions (electrode positions, head model and source model) with same coordinate system and unit. If the relative anatomical landmarks for both head-model and electrode-set are known, then automatic techniques can be applied, otherwise interactive or manual techniques are used. Figure 2.8a illustrates a head model and the template set of electrodes before being aligned. Relative anatomical landmarks were not known. Therefore, the head model and the electrodes were manually aligned as represented in Figure 2.8b.

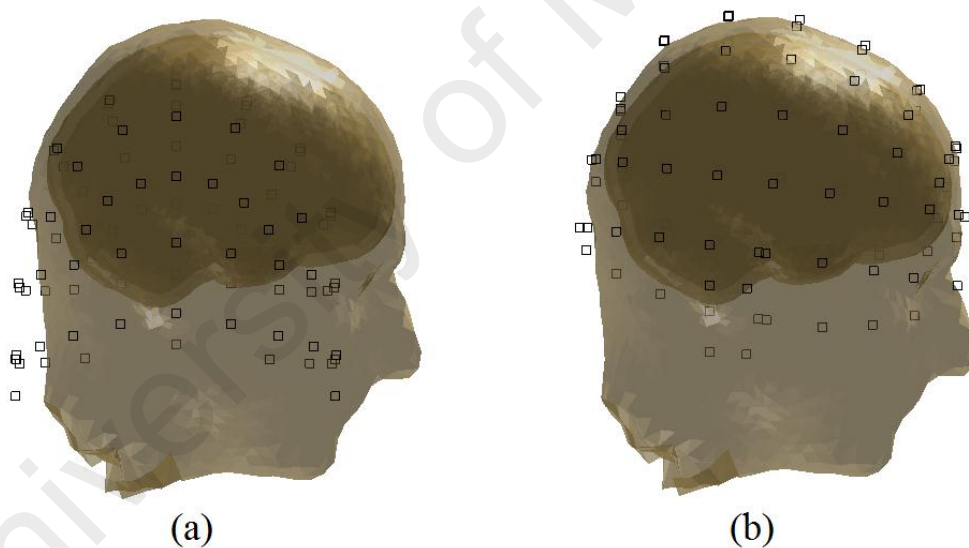


Figure 2.8: (a) Head model and template electrodes without being aligned. (b) Electrodes and the head model after manual alignment.

2.3.2 Forward Solution

In physical world, predicting the error-free values of the observed parameters by using some known parameters and a model is known as forward problem (Tarantola, 2005), while its solution is considered as forward solution. Mathematical formulation of forward problem is given below.

In symbolic terms, the EEG forward problem is that of finding, in a reasonable time, the scalp potential $g(\mathbf{r}, \mathbf{r}_{dip}, \mathbf{d})$ at an electrode positioned on the scalp at \mathbf{r} due to a single dipole with dipole moment $\mathbf{d} = d\mathbf{e}_d$ (with magnitude d and orientation \mathbf{e}_d , see Equation 2.1), positioned at \mathbf{r}_{dip} . This amounts to solving Poisson's equation to find the potentials $V(\mathbf{r})$ on the scalp for different configurations of \mathbf{r}_{dip} and \mathbf{d} . For multiple dipole sources, the electrode potential would be $V(\mathbf{r}) = \sum_i g(\mathbf{r}, \mathbf{r}_{dip_i}, \mathbf{d}_i) = \sum_i g(\mathbf{r}, \mathbf{r}_{dip_i}, \mathbf{e}_{d_i})d_i$. In practice, one calculates a potential between an electrode and a reference (which can be another electrode or an average reference).

For N electrodes and p dipoles:

$$V = \begin{bmatrix} V(\mathbf{r}_1) \\ \vdots \\ V(\mathbf{r}_N) \end{bmatrix} = \begin{bmatrix} g(\mathbf{r}_1, \mathbf{r}_{dip_1}, \mathbf{e}_{d_1}) & \cdots & g(\mathbf{r}_1, \mathbf{r}_{dip_p}, \mathbf{e}_{d_p}) \\ \vdots & \ddots & \vdots \\ g(\mathbf{r}_N, \mathbf{r}_{dip_1}, \mathbf{e}_{d_1}) & \cdots & g(\mathbf{r}_N, \mathbf{r}_{dip_p}, \mathbf{e}_{d_p}) \end{bmatrix} \begin{bmatrix} d_1 \\ \vdots \\ d_p \end{bmatrix}$$

$$= G(\mathbf{r}_j, \mathbf{r}_{dip_i}, \mathbf{e}_{d_i}) \begin{bmatrix} d_1 \\ \vdots \\ d_p \end{bmatrix}$$

where $i = 1, \dots, p$ and $j = 1, \dots, N$. Here V is a column vector. For N electrodes, p dipoles and T discrete time samples:

$$V = \begin{bmatrix} V(\mathbf{r}_1, 1) & \cdots & V(\mathbf{r}_1, T) \\ \vdots & \ddots & \vdots \\ V(\mathbf{r}_N, 1) & \cdots & V(\mathbf{r}_N, T) \end{bmatrix} = G(\mathbf{r}_j, \mathbf{r}_{dip_i}, \mathbf{e}_{d_i}) \begin{bmatrix} d_{1,1} & \cdots & d_{1,T} \\ \vdots & \ddots & \vdots \\ d_{p,1} & \cdots & d_{p,T} \end{bmatrix}$$

$$= G(\mathbf{r}_j, \mathbf{r}_{dip_i}, \mathbf{e}_{d_i}) \mathbf{D}$$

where V is now the matrix of data measurements, G is the gain matrix and D is the matrix of dipole magnitudes at different time instants. More generally, a noise or perturbation matrix \mathbf{n} is added,

$$V = GD + n \quad (2.2)$$

Hallez et al. (2007, p. 12)

2.3.3 Functional Data Preprocessing

In addition to the cerebral activities, scalp EEG also records electrical activities from various surrounding sources other than the brain. Any portion of the EEG whose origin is not from the brain is known as the artifact. Due to these artifacts EEG can be misinterpreted and any analysis of EEG can produce misleading results. (Benbadis and Tatum, 2003; Krauss et al., 2005). Therefore; their recognition, identification, and eventual elimination are very important. This subsection is concerned with the preprocessing steps that are applied in dealing with these artifacts before the actual source localization.

There are mainly two types of artifacts, namely physiological artifacts and non-physiological artifacts (Ebersole & Pedley, 2003; Fisch & Spehlmann, 1999). The first type of artifacts usually arises from various sources within the body other than the brain whereas the other type arises outside the body. Common sources of physiological artifacts are: cardiac activity, eye blinks, ocular movements, muscular activity etc. (Daly, Nicolaou, Nasuto, & Warwick, 2013; Romero, Mañanas, & Barbanoj, 2008; Urigüen & Garcia-Zapirain, 2015). In contrast external sources, such as power line, electronic components, electrical equipment, electrodes, environment, etc., causes non-physiological artifacts. Various methods were proposed for artifact removal from EEG records. Each method focused on removing very few types of artifacts because of the diverse characteristics (Urigüen & Garcia-Zapirain, 2015) and combination of two or more methods are mostly applied for cleaning the EEG records. Some common methods are discussed briefly in the following sub-subsections.

2.3.3.1 Artifact Rejection

This is the easiest artifact removal technique, in which poor quality EEG epochs are identified and removed. This technique removes easily detectable artifacts that last for a short period of time. Simply rejecting contaminated EEG epochs results in a considerable loss of collected information. Moreover some artifacts (such as line power artifact) are distributed throughout the entire recordings, so such epoch rejection may not give clean EEG data for analysis.

2.3.3.2 Filtering

One of the common artifact removal techniques is filtering and low pass, band pass, and high pass filters are the classical filters used. These filters can remove artifacts effectively from EEG records when the frequency band of interference is different from brain signals (Sweeney, Ward, & McLoone, 2012). In case of ictal EEG spectral overlap is very common. Other specialized filters, such as adaptive filter (Correa, Laciari, Patiño, & Valentinuzzi, 2007), Wiener filter, Bayes filter, etc., are useful for such EEG records with spectral overlapping. Another advantage is that these filters can be automated (Sweeney, Ayaz, et al., 2012; Urigüen & Garcia-Zapirain, 2015).

2.3.3.3 Regression

Regression-based techniques require one or more reference signals, such as electrooculogram (EOG), electrocardiogram (ECG), etc., along with the EEG signals. They use regression analysis for defining the amplitude relation between the reference signal(s) and the EEG signal of every channel. An estimated portion of the reference signal(s) are subtracted from the EEG signals for artifact correction. These techniques are mostly used for correcting ocular artifacts (Croft & Barry, 2000; Wallstrom, Kass, Miller, Cohn, & Fox, 2004) and cardiac artifacts (Waser & Garn, 2013). One limitation of these techniques is the bidirectional contamination among brain signal and reference

signal (Wallstrom et al., 2004). It means both the signals can contaminate each other and correction based on one (reference) may not be appropriate. Another limitation is their dependency on one or more reference channels. Due to these limitations regression-based techniques are replaced by other modern techniques (Urigüen & Garcia-Zapirain, 2015).

2.3.3.4 Blind Source Separation

Blind Source Separation (BSS) technique separates individual source components from their mixtures that are recorded at multiple sensors. It is a widely used model (Sarvas, 1987; Urigüen & Garcia-Zapirain, 2015) and it considers the scalp recorded potentials as linear mixtures of brain signals and unwanted noise signals as shown in Figure 2.9. The mathematical representation of this model is given in Equation 2.2 where V is the EEG data matrix and D is the source matrix. The gain matrix G can be considered as the mixing matrix. It does not need a reference signal for estimating the sources D from the recorded dataset V by using Equation 2.2. The success of BSS depends on proper estimation of source and correct separation of the brain sources from the artifacts (Urigüen & Garcia-Zapirain, 2015). As little information on the underlying sources is available a priori, ESI is a typical application for BSS methods (Vigario & Oja, 2008). While studying BSS problems, scholars proposed a number of classic met-

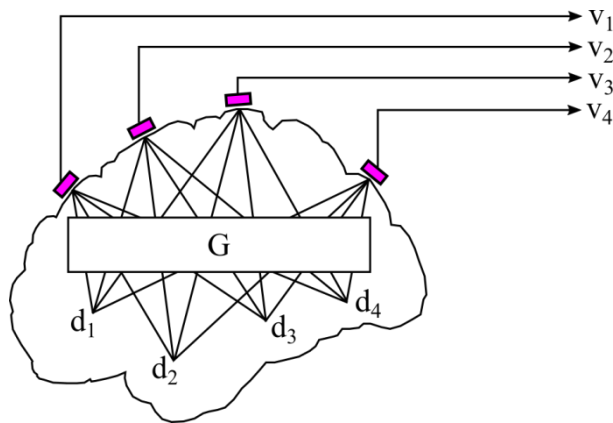


Figure 2.9: Scalp potentials as a mixture of the cortical source potentials.

-hods: PCA, projection pursuit, factor analysis, and ICA. Since ICA is widely used in ESI solutions, more details of ICA are discussed in the next sub-subsection.

2.3.3.5 Independent Component Analysis

This method emerged as a useful extension of PCA method. The major problem with PCA is its assumption of orthogonality between brain activity and physiological artifacts which does not generally hold (Uriguen & Garcia-Zapirain, 2015). ICA assumes that the source signals are statistically independent and most authors agree with this idea (James & Hesse, 2005; T. P. Jung et al., 2000; Vigário, 1997).

The mathematical formulation for ICA model is given below, as discussed in (Onton, Westerfield, Townsend, & Makeig, 2006). *The data submitted to ICA are simply the recorded EEG channel data arranged in a matrix of n channels (rows) by t time points (columns). No channel location information at all is used in the analysis. ICA performs a blind separation of the data matrix (X) based only on the criterion that resulting source time courses (U) are maximally independent. Specifically, ICA finds a component ‘unmixing’ matrix (W) that, when multiplied by the original data (X), yields the matrix (U) of independent component (IC) time courses:*

$$U = WX \quad (2.3)$$

where X and U are $n \times t$ matrices, and W is $n \times n$ matrix. By simple matrix algebra, Equation 2.3 implies that:

$$X = W^{-1}U$$

Here, W^{-1} is the $n \times n$ component ‘mixing’ matrix whose columns contain the relative weights with which the component projects to each of the scalp channels, i.e., the IC

scalp map. The portion of the original data (X) that forms the i th IC (X_i) is the (outer) product of two vectors, the i th column of W and the i th row of U ,

$$X_i = W_i^{-1} U_i$$

and the whole data (X) are the sum of the (back-projected) ICs (X_i):

$$X = \sum X_i, \quad \text{where } i = 1, 2, \dots, n.$$

Each component is projected to the EEG electrodes according the weights of the corresponding column in the mixing matrix (W^1). These weights can also be used for generating the topographic maps that help to visualize the scalp projection of each component. “Thus, the IC activations (U), can be regarded as the EEG waveforms of single sources, although obtaining their actual amplitudes at the scalp channels requires multiplication by the inverse of the unmixing matrix (W^1)” (Onton et al., 2006).

2.3.3.6 Other Denoising Techniques

Only a few common techniques are discussed above. Other solutions for artifact correction are also available but less frequently used. Some examples are: principal component analysis (PCA) (Berg & Scherg, 1991; Fitzgibbon, Powers, Pope, & Clark, 2007), discrete wavelet transform (DWT) (Krishnaveni, Jayaraman, Anitha, & Ramadoss, 2006), empirical mode decomposition (EMD) (Safieddine et al., 2012), nonlinear mode decomposition (NMD) (Iatsenko, McClintock, & Stefanovska, 2015), etc. Another basic technique, that is used very commonly, is the averaging of the similar EEG events for improving the SNR. It first detects several similar events and then extracts segments of same size around each event and finally averages the segments.

2.3.4 Inverse Solution

In case of a volume conductor, the problem of finding the internal source of a given set of surface potentials is known as inverse problem and any technique for solving this problem is known as inverse solution. Since, an infinite number of internal sources can produce the same surface potential, the inverse problem has no unique solution and it is an ill-posed problem (Helmholtz, 1853; Kaiboriboon et al., 2012). Various a priori assumptions are used to solve the inverse problem (Van Oosterom, 1991).

With respect to Equation 2.2, the inverse solution uses the gain matrix G , the electrode positions and the scalp potentials V to estimate \hat{D} of the dipole magnitude matrix D (Grech et al., 2008). Inverse solution also records the locations of the estimated dipoles. More specifically the inverse solution usually estimates six parameters that specify a dipole: three spatial coordinates (x, y, z) and three dipole moment components (orientation angles (θ, φ) and strength d). Parametric and non-parametric methods are the two main approaches that are followed in the inverse solution.

2.3.4.1 Parametric Methods

Parametric Methods require an a priori assumption on the number of dipoles. This number ranges from a single dipole in a spherical head model, to a large number of dipoles (ten or more) in a realistic head model. Parametric Methods are also known as Equivalent Current Dipole Methods or Spatio-Temporal Dipole Fit Models or Concentrated Source. These methods search for the best dipole position(s) and orientation(s).

(a) *Single Dipole Model*

This model considers every instant of the scalp potential as an activity of a single dipole located in an infinitely small cortical region (Pascual-Marqui, Sekihara,

Brandeis, & Michel, 2009). This assumption is not very realistic and does not represent the biological facts. Therefore single dipole model is useful for a limited number of clinical conditions. Appreciable outcomes were recorded for using this model in epileptic spikes and auditory evoked potential analysis (Ebersole & Hawes-Ebersole, 2007; Pascual-Marqui et al., 2009). Despite this limitation single dipole model is the most commonly used model (Kaiboriboon et al., 2012). Besides, it has another variety—the so-called moving dipole model (Darcey, Ary, & Fender, 1980; Schneider, 1972).

(b) *Multiple Dipole Model*

This model assumes that any intent of the scalp-recorded potentials represents activities from more than one cortical source. One example of such advanced dipole models is the spatiotemporal multiple source model (Scherg & Von Cramon, 1985). In contrast to the moving single dipole model, multiple dipole model identifies the lowest number of dipoles that can explain the measured scalp potential (Ebersole & Hawes-Ebersole, 2007). Some approaches that use multiple dipole model include multiple signal classification (MUSIC) (Mosher, Lewis, & Leahy, 1992), recursively applied and projected multiple signal classification (RAP-MUSIC) (Mosher & Leahy, 1998), common spatial pattern decomposition (Koles, Lind, & Soong, 1995), a combination of ICA and RAP-MUSIC (Kobayashi, Akiyama, Nakahori, Yoshinaga, & Gotman, 2002), and the first principle vector (FINES) approach (Xu, Xu, & He, 2004).

2.3.4.2 Non-parametric Methods

The inverse solutions that use non-parametric methods are also known as distributed source models or distributed inverse solutions. In contrast to the parametric methods these methods do not need a priori assumption on the number of dipoles and assume that multiple sources of multiple cortical locations can act simultaneously at any given

time (Plummer et al., 2008). Dipole sources are assumed to have fixed locations and possibly fixed orientations and are distributed throughout the cortical surface. The inverse solutions estimate the strength (and orientation) of these dipole sources.

Since inverse problem is an ill-posed problem various assumptions are needed to identify the 'optimal' or 'most likely' solution (Michel et al., 2004). Different choices and implementations of these assumptions were introduced in the literature. The low-resolution electromagnetic tomography (LORETA) algorithm assumes that the neighboring neurons are more likely to discharge synchronously than the non-neighboring neurons (Pascual-Marqui, Michel, & Lehmann, 1994). This algorithm, therefore, tends to estimate a broader source region because the neighboring sources are assumed to have similar strength. The idea of normalization was used in the standardized low resolution brain electromagnetic tomography (sLORETA) method (Pascual-Marqui, 2002). The minimum norm estimate (MNE) approach (Hämäläinen & Ilmoniemi, 1994) assumes minimum overall intensity for the 3D current distribution. The solution can be considered unique in the sense that only one source combination can have the lowest overall intensity as well as fit the data exactly. This MNE approach has the tendency to identify the superficial cortical sources. In order to minimize this tendency, weighting strategy was introduced in weighted minimum norm estimate (wMNE) technique (Lin et al., 2006). The local autoregressive average (LAURA) method (de Peralta Menendez, Murray, Michel, Martuzzi, & Andino, 2004) uses electromagnetic theory of Maxwell equation and assumes that the activity will fall off (or regress) while moving away from the source. Several other inverse solutions was proposed and each method has their own sets of a priori assumptions. Some examples are: focal underdetermined system solution (FOCUSS) (Gorodnitsky, George, & Rao, 1995), EPIFOCUS (de Peralta Menendez, Andino, Lantz, Michel, & Landis, 2001), dynamical statistical parametric mapping (dSPM) (Dale et al., 2000), variable resolution

electric-magnetic tomography (VARETA) (Valdes-Sosa, Marti, Garcia, & Casanova, 2000), etc.

2.4 Software Tools for Realistic Head Model Generation

A computer generated model of human head is inevitable for the automatic localization of EEG sources. Anatomically realistic and subject specific head models are essential for the accurate localizations of EEG sources. Realistic head model of a subject can be generated from the MRI scans of subject's head. A variety of software solutions, both free (Acar & Makeig, 2010; Cointepas, Mangin, Garnero, Poline, & Benali, 2001; Dale, Fischl, & Sereno, 1999; Oostenveld, Fries, Maris, & Schoffelen, 2011; Shattuck & Leahy, 2002) and commercial (e.g. BrainVoyager QX, BESA MRI, and CURRY), are available for generating realistic subject specific head models from individual subject's MRI scans. Commercial tools can generate ESI results independently, but those tools have limited functionalities and cannot be customized for special needs. On the contrary, open-source solutions are neither independent nor complete, but multiple tools can produce the ESI solutions jointly. Moreover, the open-source tools are customizable and can offer customized solutions with broader range of functionalities. Therefore open-source tools are useful for the studies that intend to develop and implement any new technique. Each software tool has certain advantages and limitations. Critical comparisons of these software tools are very important for selecting the most suitable one for a particular use.

A few studies compared the software tools that are used for MRI segmentation and surface generation. Tsang et al. (2008) provided a quantitative analysis and comparison of the segmentation algorithms of two software tools, namely Statistical Parametric Mapping (SPM) (Ashburner & Friston, 2005) and FMRIB Software Library (FSL). Another study (Klauschen, Goldman, Barra, Meyer-Lindenberg, & Lundervold, 2009)

compared three widely used brain volumetry methods available in the software packages FSL, SPM5, and FreeSurfer (Dale et al., 1999). They evaluated the performance using simulated and real brain MRI data sets and their study was focused on the accuracy of volume measurements and the robustness against changes of image quality. Recently, Kazemi and Noorizadeh (2014) investigated the accuracy of three software packages SPM, FSL and BrainSuite (Shattuck & Leahy, 2002) for brain tissue segmentation. All of these comparative studies were mostly focused on the underlying algorithms and concepts of the software tools and were less concerned about the usability issue.

Head MRI segmentation is an image processing operation that should be performed before implementing any numerical head model generation technique. Its goal is to separate each MRI scan of a subject into a number of different homogeneous regions where each region corresponds to a particular type of tissue of the subject's head. Automatic MRI segmentation tools, used for EEG or MEG source localization, usually separate three or more types of tissues. Typically segmented tissue types are scalp, skull, CSF, white matter (WM) and grey matter (GM). Mesh generation modules of the head modelling tools use the outcomes of the segmentation step and create triangular meshes that fit the boundaries of the segmentation. Some software tools are briefly introduced below.

FieldTrip (Oostenveld et al., 2011) is an open-source MATLAB-toolbox for source analysis of oscillatory electromagnetic activity (MEG and EEG) of brain and was developed by the Donders Institute for Brain, Cognition and Behaviour, University Nijmegen, Netherlands. This software package can be downloaded from <http://fieldtrip.fcdonders.nl/download>.

Neuroelectromagnetic Forward Head Modeling Toolbox (NFT) (Acar & Makeig, 2010) is also an open-source MATLAB toolbox. It can generate realistic head models from available data (MRI and/or electrode locations) and can compute numerical solutions for the forward problem of EEG or MEG source localization. NFT uses some third party tools and libraries for segmentation and mesh generation: ASC for triangulation of 3D volumes, Qslim for mesh coarsening and Matitk - MATLAB interface to the ITK image processing toolkit. Source code of NFT is available at <http://sccn.ucsd.edu/nft/install.html>.

Another tool called BrainVISA offers several features such as: Workflows and pipelines, Graphical user interface, Visualization, Massive computation facilities, Toolboxes (Cointepas et al., 2001; Geffroy et al., 2011). Application field of BrainVISA is extremely wide, because virtually any software can be integrated with this software tool (Riviere et al., 2003). It is developed by a French federative research institute: IFR 49. It is an open-source software written in Python script language and can be downloaded from: <http://brainvisa.info/download.html>.

BrainSuite is a collection of image analysis tools designed to process MRI of the human head. It is free but not open source. It can extract cortical surface mesh models from the MRI. It provides tools for registering these surfaces to a labelled atlas, for processing diffusion imaging data, for visualization of these data, and for interactive mapping of regional connectivity. BrainSuite is collaboratively developed by Ahmanson-Lovelace Brain Mapping Center at University of California, Los Angeles and Biomedical Imaging Group at University of Southern California, Los Angeles. The latest version of BrainSuite is available for download from <http://brainsuite.org/download/>.

FreeSurfer Software Suite is an open source software suite for processing and analyzing human brain MRI images. Skull stripping, image registration, subcortical segmentation, cortical surface reconstruction, cortical segmentation, cortical thickness estimation, longitudinal processing, fMRI analysis, tractography, FreeView visualization GUI, etc. are the mentionable features of FreeSurfer. This software tool was developed at the Martinos Center for Biomedical Imaging by the Laboratory for Computational Neuroimaging. FreeSurfer executables are available for download from <http://surfer.nmr.mgh.harvard.edu/fswiki/DownloadAndInstall>.

2.5 Ictal EEG Source Imaging

The process of estimating the epileptogenic zone by using an ESI technique and by analyzing the ictal EEG is known as ictal ESI. Very few studies (Assaf & Ebersole, 1997, 1999; Beniczky et al., 2006; Boon et al., 2002; Ding, Worrell, Lagerlund, & He, 2007; Holmes et al., 2010; Jung et al., 2009; Koessler et al., 2010; Kovac et al., 2014; Lantz et al., 1999; Lu, Yang, Worrell, Brinkmann, et al., 2012; Lu, Yang, Worrell, & He, 2012; Merlet & Gotman, 2001; Petros et al., 2017; Praveen et al., 2018; Yang et al., 2011) evaluated the performance of ictal ESI. More than one-third of these reviewed techniques (Assaf & Ebersole, 1997, 1999; Jung et al., 2009; Lantz et al., 1999; Merlet & Gotman, 2001; Petros et al., 2017) used multilayer spherical head models whereas five other studies (Beniczky et al., 2006; Holmes et al., 2010; Kovac et al., 2014; Praveen et al., 2018; Yang et al., 2011) used template MRI based realistic head models for epileptogenic focus estimation. Such generalized head models have significant anatomical differences with their corresponding real heads. Therefore, from the surgical point of view, it is obvious that such strategies of ESI do not necessarily provide correct solutions. Only six (Boon et al., 2002; Ding et al., 2007; Koessler et al., 2010; Lu, Yang, Worrell, Brinkmann, et al., 2012; Lu, Yang, Worrell, & He, 2012; Petros et al., 2017) out of sixteen articles on ictal ESI used patient specific realistic head models for

their studies. Since, sensitivity of ESI can be increased by using patient specific realistic head models (Brodbeck et al., 2011), further studies on ictal ESI are expected to use such realistic models.

In comparison with extratemporal lobe epilepsy, ictal events in temporal lobe epilepsy are mostly examined in the ictal ESI studies. Thirteen (Assaf & Ebersole, 1997, 1999; Beniczky et al., 2006; Boon et al., 2002; Ding et al., 2007; Holmes et al., 2010; Jung et al., 2009; Koessler et al., 2010; Lantz et al., 1999; Lu, Yang, Worrell, Brinkmann, et al., 2012; Lu, Yang, Worrell, & He, 2012; Merlet & Gotman, 2001; Yang et al., 2011) out of sixteen reviewed articles on ictal ESI have investigated the ictal events in temporal lobe epilepsy while ten (Boon et al., 2002; Ding et al., 2007; Holmes et al., 2010; Koessler et al., 2010; Lu, Yang, Worrell, Brinkmann, et al., 2012; Lu, Yang, Worrell, & He, 2012; Merlet & Gotman, 2001; Petros et al., 2017; Praveen et al., 2018; Yang et al., 2011) of those sixteen articles have extended their investigations for extratemporal lobe epilepsy patients. One recent article (Kovac et al., 2014) on ictal ESI inspected the ictal events in frontal lobe epilepsy only. Since the presurgical evaluation in extratemporal lobe epilepsy is more complicated than that in temporal lobe epilepsy, more prospective studies on extratemporal epileptic source analysis are required.

Kovac et al. (Kovac et al., 2014) conducted a recent study on ictal ESI which investigated whether ictal ESI, using low density EEG recording of eight patients, can provide better lateralization compared to the visual inspection. Use of template MRI based finite element head model has been mentioned as one of the major limitations of this work. Patient specific realistic head models were used in six ictal ESI studies (Boon et al., 2002; Ding et al., 2007; Koessler et al., 2010; Lu, Yang, Worrell, Brinkmann, et al., 2012; Lu, Yang, Worrell, & He, 2012; Petros et al., 2017) and most of these studies (Boon et al., 2002; Koessler et al., 2010; Lu, Yang, Worrell, Brinkmann, et al., 2012;

Lu, Yang, Worrell, & He, 2012; Petros et al., 2017) validated their ictal ESI results against stereoelectroencephalography (SEEG) and postsurgical outcomes. Although, SEEG can estimate the epileptic focus more precisely than visual analysis of scalp EEG, this invasive modality has several surgical constraints as well. Since ESI is a noninvasive modality for epileptic source localization, it is logical to compare its results with an equivalent modality such as SPECT. Ding et al. (Ding et al., 2007) analyzed seizures from five epilepsy patients and their ictal ESI results were consistent with either MRI lesions or SPECT scans. They proposed a novel but complicated method based upon a combination of the subspace source localization technique and the spectrum-based causal interaction estimation technique. Beniczky et al. (Beniczky et al., 2006) used classical (non-ICA based) method for conducting ictal ESI study and validated the results against corresponding SPECT results. They also performed interictal ESI in the same group of patients as ictal ESI and presented there interrelations. Using template MRI based BEM model is the major limitation of their study.

Although standard medical EEG systems use between 19 and 32 electrodes, high resolution EEG systems include up to 256 electrodes. The electrodes are positioned on the scalp according to a standardized placement system. For 21 electrodes, the original 10-20 system (Jasper, 1958; Klem, Lüders, Jasper, & Elger, 1999) is employed whereas for higher numbers of electrodes, extensions of this system such as the 10-10 and the 10-5 electrode systems are used (Chatrian, Lettich, & Nelson, 1985; Oostenveld & Praamstra, 2001). A study (Srinivasan, Tucker, & Murias, 1998) showed that, in order to sample the electric field properly from the head surface at least 100 electrodes are needed. Another study (Lantz, Grave de Peralta, et al., 2003) highlighted the importance of high density EEG for improving the source reconstruction accuracy. Despite all these advantages, high resolution EEG is less frequently used for the validation of the ESI

techniques. Only six (Holmes et al., 2010; Jung et al., 2009; Koessler et al., 2010; Lu, Yang, Worrell, & He, 2012; Petros et al., 2017; Yang et al., 2011) out of sixteen reviewed studies used high resolution EEG (above 32 channel) for ESI while the other studies used standard EEG for the purpose but without any customization of the ESI technique. In this context, customization of the ESI technique for standard EEG based source localization would be an added advantage, because standard EEG is mostly used for clinical evaluation.

2.6 ICA Based Ictal EEG Source Imaging

It has been mentioned earlier that only few studies (Assaf & Ebersole, 1997, 1999; Beniczky et al., 2006; Boon et al., 2002; Ding et al., 2007; Holmes et al., 2010; Iriarte et al., 2006; Jung et al., 2009; Koessler et al., 2010; Kovac et al., 2014; Lantz et al., 1999; Lu, Yang, Worrell, Brinkmann, et al., 2012; Lu, Yang, Worrell, & He, 2012; Merlet & Gotman, 2001; Nam, Yim, Han, Oh, & Lee, 2002; Petros et al., 2017; Praveen et al., 2018; Yang et al., 2011) have used ictal EEG for cortical source estimation through ESI. Almost all of these studies, except two (Iriarte et al., 2006; Nam et al., 2002), used digital bandpass filters to improve the SNR by minimizing high frequency noises, DC linear trends, movement and muscle artifacts. Even though the effective uses of filters are well-verified, they are inadequate for noise elimination because of their inability to discriminate between artifact and brain waves (Iriarte et al., 2003; Nam et al., 2002). Averaging of the ictal activities is another commonly used technique for the improvement of SNR (Assaf & Ebersole, 1997, 1999; Beniczky et al., 2006; Habib et al., 2016; Kovac et al., 2014; Merlet & Gotman, 2001). Although commonly used, averaging of selected ictal events can eliminate valuable cortical information and thus can lead to inaccuracies in the ESI result (Chitoku et al., 2003). A variety of procedures were proposed to correct ocular artifacts but those are not very popular in ictal ESI studies due to their failure to deal with other noises. Rather than using these procedures,

sometimes visible artifacts are screened through visual inspection (Holmes et al., 2010) in addition to bandpass filters. Another well-known technique for signal and noise subspaces separation is the principal component analysis (PCA). None of the ictal ESI studies applies PCA because of its unrealistic assumption of orthogonality between neural activity and artifact (Delorme & Makeig, 2004; Romero et al., 2008).

Independent component analysis (ICA) is comparatively a more powerful statistical technique that can decompose a mixture of signals into a set of statistically independent components. In the context of EEG signals, ICA can decompose each set of EEG into a series of spatially fixed and temporally independent components (Yang et al., 2011). The ICA-based ictal ESI studies (Iriarte et al., 2006; Jung et al., 2009; Leal, Dias, & Vieira, 2006; Lu, Yang, Worrell, Brinkmann, et al., 2012; Nam et al., 2002; Praveen et al., 2018; Yang et al., 2011) used ICA for EEG denoising and thus extracted the EEG signals of interest. Independent components from extracerebral origin (e.g. muscle artifacts, eye movements, and power line noise, etc.) were removed for denoising (McMenamin et al., 2010), whereas the components that display ictal nature (i.e. the ictal components) were extracted for epileptogenic zone localization. Proper identification of these ictal components is the major challenge for ICA-based ictal ESI techniques. Iriarte et al. (2006) depended only on visual inspection of the component time-courses and their corresponding reconstructed EEGs for selecting the ictal component(s). In addition to visual inspection, Nam et al. (2002) reviewed autocorrelogram for ictal component selection. They also conducted a quantitative analysis and used power spectral density (PSD) for ictal component selection. Components having higher proportion of power in the theta-band (exactly 2-10 Hz) were selected for source estimation. Jung et al. (2009) excluded the ICs of extracerebral origin by visually inspecting activation spectra (i.e. PSD) and scalp voltage topography. They also excluded the ICs with a residual variance of more than 20% before selecting

the ictal components through visual inspection. Three other ICA-based ictal ESI studies (Leal et al., 2006; Lu, Yang, Worrell, Brinkmann, et al., 2012; Yang et al., 2011) utilized time-frequency representation (TFR) in addition to the above mentioned tools and techniques for selecting the ictal components. They also used bootstrap statistical method and surrogate data, with further assistance of visual inspection, to evaluate the significance of the spectral changes in a TFR or to assess the correlation between two different TFRs.

The above review indicates that the existing ictal component selection techniques are highly dependent on the visual inspection and are therefore susceptible to experimenter's judgment or bias. In this context, the aim of this study was to develop a quantitative technique to select the best ictal component (BIC) for EEG source imaging with potential application in presurgical evaluation of refractory focal epilepsy. A recursive approach, using a unique quantitative feature of ictal EEG decomposition, was proposed in this study and was named as the *recursive ICA-decomposition for ictal component selection* (RIDICS) technique. The performance of the RIDICS technique was compared with that of the other two quantitative techniques, namely PSD-based technique and TFR-based technique. All the techniques were implemented on both simulated and real ictal EEG data for validation. The results of simulation-study were validated using the known location of a dipole source, while the results of real-data-analysis were validated by using the known cortical sites of successful clinical surgeries of focal epilepsy patients.

2.7 Summary

Epilepsy is one of the most common neurological disorders and focal epilepsy is the most common form of adult epilepsy. EEG is widely used for the presurgical evaluation of refractory focal epilepsy through identifying the epileptogenic zone but ESI is

comparatively a new computational technique for the precise localization of that cortical zone. Researchers started working for finding the relation between the source of neural activities and its diagnostic potentials before recording the EEG for the first time (Helmholtz, 1853), but the application of those research become practical through ESI in the past two decades (Kaiboriboon et al., 2012; Michel & Murray, 2012).

ESI is a potential tool for localizing the epileptogenic zone by analyzing scalp EEG recorded during both ictal and interictal activities. Ictal EEG is believed to be more reliable than interictal EEG in localizing the epileptogenic focus, but comparatively difficult to analyze by using ESI because of the low Signal to Noise Ratio (SNR), undetectable low strength of ictal events before being spread considerably, difficulties of recording reliable seizure data, and lack of efficient ESI techniques. Therefore there have been very few studies that use ictal EEG for cortical source imaging and the ESI techniques employed are not common. Moreover, the accuracy of an ESI technique improves with the use of high resolution EEG (i.e. a high total number of electrodes over the region of interest), but the standard medical EEG systems comprise between 19 and 32 electrodes. In this context, developing an improved ictal ESI technique, with adequate optimization for low resolution EEG input, for the noninvasive presurgical evaluation of refractory focal epilepsy is an interesting and challenging research problem.

CHAPTER 3: METHODOLOGY

3.1 Introduction

This chapter describes the materials and methods required for developing a new ICA-based ictal ESI technique for the presurgical evaluation of refractory focal epilepsy patients and with the use of standard low resolution medical EEG data. The goal of this study was achieved in few stages. The overall strategy is outlined here with the help of a workflow diagram that highlights the major steps required for designing, implementing and validating the proposed RIDICS technique. Each step is discussed in detail later in this chapter. It also includes the mathematical formulations required for the implementation of the RIDICS technique.

3.2 Outline of the Strategy

Microscopic neuronal ionic current is responsible for the generation of scalp EEG signals and identifying the site of origin of such current source is the common goal of all the ESI techniques. The way of achieving this goal is not straightforward, because it requires the implementation of a number of independent mathematical algorithms as shown in Figure 2.4. Improvement in any of these algorithms concurrently creates positive-effect on the overall performance of the ESI technique. A threefold approach was taken to achieve a better overall performance with the RIDICS technique. Firstly, the subject-specific realistic head models and an appropriate head model generation tool were used in the *Head Model* generation step (see Figure 2.4). The software tool was selected through a comparative evaluation of five open-source software solutions that could generate realistic head models from the MRI images. Secondly, high performance inverse model was used in the *Inverse Solution* step (see Figure 2.4) of the RIDICS technique. The clinical utility of non-ICA based ESI technique and the advantages of ictal ESI over interictal ESI were assessed by the use of open-source software tools, patient-specific realistic forward models and three different linear distributed inverse

models. The best performing inverse model was used in the RIDICS technique. Finally, and most importantly, a new recursive ICA-decomposition technique was introduced in the proposed ESI solution for a substantial improvement in the *Functional Data Preprocessing* step (see Figure 2.4). These key steps of the methodology are illustrated through a workflow diagram as shown in Figure 3.1 and are described in the following sections.

3.3 Primary Investigation on Various Aspects of Neurological Disorders

Various aspects of the neurological disorders, which could be diagnosed and analyzed with the ESI, were explored at the beginning of this study. Although priority

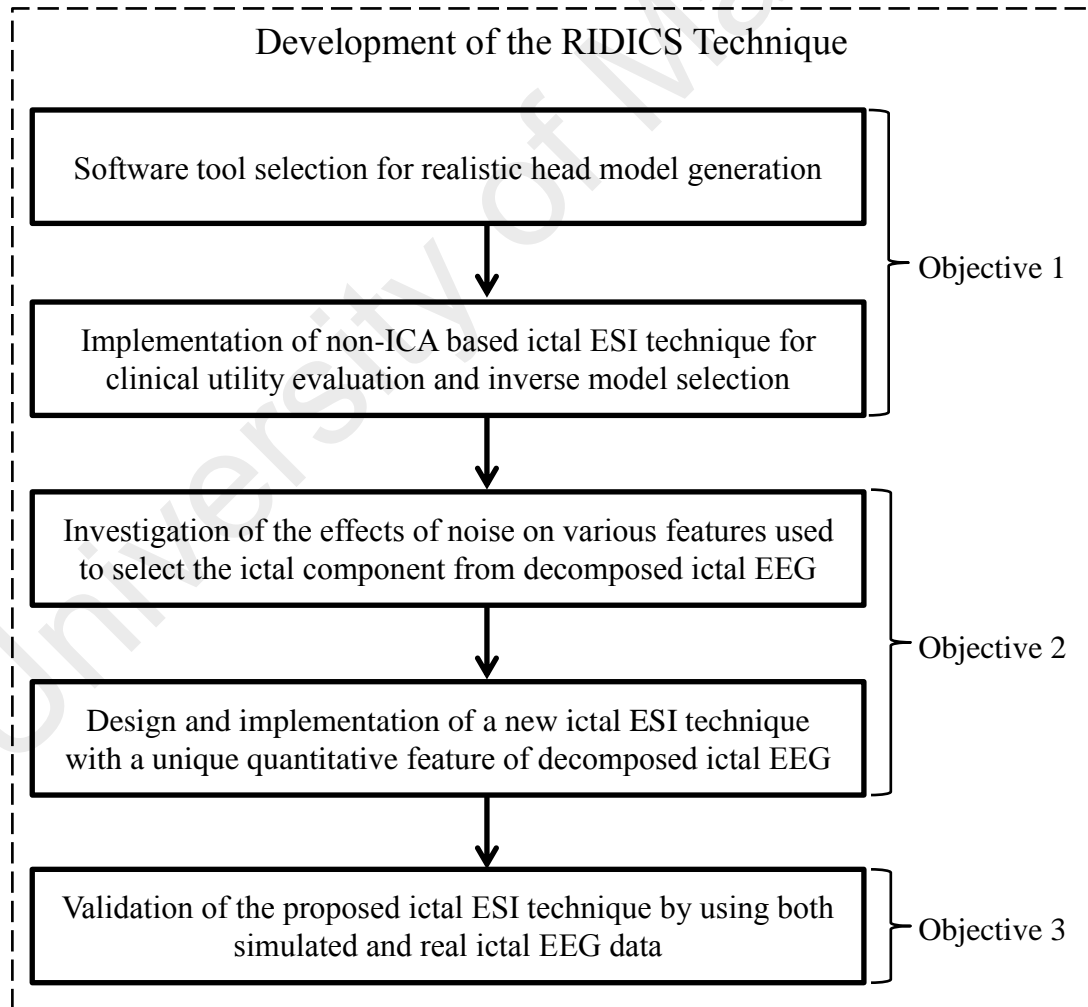


Figure 3.1: Workflow diagram that shows the major steps in developing the improved ESI technique.

was given to Epilepsy, some other neurological disorders (such as Dementia and Alzheimer's disease) were investigated as well. With various disease specific physiological aspects some common aspects are also found and fall is one of them. Many paroxysmal and acute neurological diseases lead to fall since disturbances of stance and gait are frequent symptoms in neurological patients (Stolze et al., 2004). Individuals with epilepsy fall during seizure events due to loss of consciousness (Lawn, Bamlet, Radhakrishnan, O'Brien, & So, 2004), while those with dementia are two to three times more likely to fall than individuals without cognitive impairment (Elliott, Painter, & Hudson, 2009). Since the prevalence of falls among neurological in-patients is very high, facts of falls have been further investigated and the findings were summarized in a review article (Habib, Mohktar, et al., 2014).

3.4 Software Tool Selection for Realistic Head Model Generation

Open-source software tools are useful due to their flexibility to modify according to the actual needs. The usability and practicality of five widely used software tools for head MRI segmentation and surface generation were investigated. Their significant characteristics from normal user's perspective were compared (Habib, Ibrahim, Mohktar, Lim, & Kamaruzzaman, 2014) for selecting the appropriate tool for this study. The selected software packages investigated were: FieldTrip, NFT, BrainVISA, BrainSuite, and FreeSurfer. These software tools were selected because they were open-source and/or free and ran on Windows operating system or Windows based virtual platform (VirtualBox). Surface generation techniques and underlying numerical methods were also considered. Common numerical methods for developing realistic head models were Boundary Element Method (BEM), Finite Element Method (FEM), and Finite Difference Method (FDM) (Schimpf, Haueisen, Ramon, & Nowak, 1998). FEM and FDM provide more realistic models but consume more computation time and memory. Therefore the implementation of FEM and FDM toolboxes are mostly in

experimental level. In this context the software tools that could generate BEM surfaces or meshes of the segmented MRI regions were selected for this comparison.

3.4.1 Dataset

T1 weighted MRI scans of five different subjects (3 females and 2 males and aged between 20 and 40) were used for comparing the performances of the selected software tools. These MRI scans were obtained from website of Neuroimaging Informatics Tools and Resources Clearinghouse Image Repository (NITRC-IR) (<http://www.nitrc.org>). All datasets were anonymous, de-identified and with no protected health information included. Other acquisition parameters were as follows: Field Strength - 3T and Voxel Resolution (mm) - 1.0 x 1.0 x 1.0. File format of all the MRI scans was gz compressed NIFTI-1 image (*.nii.gz).

3.4.2 Comparison Based on Stated Features

Published articles and official webpages of the selected software tools declared various features of those tools. Various features of the selected software tools are listed in their official webpages and also in the relevant published articles. Some of those features that are important for general users are compared. System requirement is an important feature that is needed before starting or even before installing a software tool. The selected tools are compared based on this feature. The MRI scans can come up with various data formats and users should know the supported input and output file formats. Therefore, those file formats of the selected tools are also compared.

3.4.3 Comparison Based on Real Data Analysis

FieldTrip, NIFT and BrainSuite were installed and operated properly under Windows 8.1 operating system (OS). FreeSurfer needed ORACLE VM VirtualBox support, with guest OS Xubuntu 12.04, for running on the same machine. Processor speed and system memory of this machine were 2.40GHz (Intel Core i7) and 16GB respectively. Since

BrainVISA did not run properly on Windows 8.1, it was installed in a different computer having Windows XP platform. That second machine had 1.80GHz Intel Core 2 Duo processor and 2GB system memory. All of the five selected software tools were used for generating BEM meshes/surfaces from each of the five MRI datasets.

3.5 Evaluation of the Clinical Utility of Ictal ESI Using Open-Source Tools

This step evaluates the usefulness of ictal ESI as a diagnostic modality for localizing the epileptogenic focus in patients with refractory focal epilepsy, especially extratemporal lobe epilepsy. It also examines the reliability of using open-source software for such sophisticated diagnosis. Both ictal and interictal ESI were performed by using low resolution EEG data, commonly used ESI techniques (Assaf & Ebersole, 1997, 1999; Beniczky et al., 2006; Holmes et al., 2010; Koessler et al., 2010; Kovac et al., 2014; Merlet & Gotman, 2001), patient specific realistic BEM head models and three different inverse models namely wMNE, dSPM and sLORETA. The results obtained are validated against MRI lesions and ictal SPECT. Then the performance of ictal ESI is compared with that of interictal ESI. The effects of three different inverse modelling algorithms on ictal ESI were also investigated.

3.5.1 Patients

This clinical evaluation was conducted with the use of anonymized retrospective data, and the protocols were approved by the University of Malaya Research Ethics Committee (UMREC), Malaysia. Fifteen patients, who suffered from pharmacoresistant focal epilepsy and underwent pre-surgical evaluation by means of clinical semiology, MRI, ictal SPECT and long-term video-EEG monitoring (both ictal and interictal), were selected primarily from the database of the University of Malaya Medical Centre. Eight patients whose ictal SPECTs were found concordant with the clinical semiology were included in this evaluation study. The patients' demographics and clinical characteris-

Table 3.1: Demographics and Clinical Characteristics.

No.	Gender	Age at Onset	Age at evaluation	Histopathology (based on MRI/HPE)	Surgical Resection	Type of surgery	Engel Class
1	F	15	28	FCD	Yes	Postcentral cortectomy	II
2	M	13	25	FCD	Yes	L parieto occipital cortectomy	I
3	F	12	18	FCD	No	-	N/A
4	M	14	20	FCD	Yes	R occipital cortectomy	I
5	M	13	28	FCD	Yes	L middle temporal cortectomy	I
6	M	2	26	Undetermined	No	-	N/A
7	M	12	58	HS	Yes	R selective amygdalo-hippocampectomy	I
8	M	15	48	HS	Yes	L selective amygdalo-hippocampectomy	I

Engel Class I indicates seizure free after surgery; Engel Class II indicates a decrease in seizures of more than 80% after resection.

MRI, magnetic resonance imaging; HPE, histopathologic examination; F, female; FCD, focal cortical dysplasia; M, male, L, left; N/A, not available; R, right; HS, hippocampal sclerosis.

-tics were summarized in Table 3.1. Five of these 8 patients had extratemporal lobe epilepsy, whereas the 3 patients, namely patient 5, patient 7 and patient 8, had temporal lobe epilepsy.

3.5.2 Anatomical Data Acquisition

Anatomical details of every patient's head were obtained from their corresponding MRI scans. Those details were used for presurgical evaluation as well as for generating patient-specific head models for ESI analysis. All patients' structural MRI scans were performed with a Signa HDxt 3.0T scanner (General Electric Healthcare, Wauwatosa, Wisconsin, USA). Three-dimensional, coronal T1-weighted fast spoiled gradient-recalled images were acquired with the following imaging parameters: slice thickness, 1.4 mm; field of view, 350 mm; echo time, 1.8 milliseconds; and repetition time, 6.8 milliseconds. Axial and sagittal images were reconstructed for review. In six patients,

the structural MRI showed a focal abnormality indicating an epileptogenic lesion; the other 2 patients (patient 4 and patient 6) had normal MRI findings.

3.5.3 Functional Data Acquisition

The functional states of patients' brains were recorded through long-term video-EEG. Recording was performed on all patients with standard clinical EEG setups according to the international 10–20 system with additional 2 electrodes at T1 and T2. All the recordings were captured with NicoletOne EEG/LTM system (Natus Medical Inc., Pleasanton, California, USA). Electrode impedances were kept below 10 k Ω , and sampling rate was set to 512 Hz (with one exception: 256 Hz for patient 6). The long-term EEG recordings captured between 2 and 8 seizures across all patients.

3.5.4 Nuclear Image Acquisition

Regional cerebral blood flow was measured by SPECT by the use of a brain-dedicated gamma camera, BrightView XCT (Philips Electronics N.V., Best, The Netherlands), equipped with low-energy, high-resolution collimators. Imaging was acquired within 60 minutes of the intravenous radiopharmaceutical administration of 25 mCi of ^{99m}Tc-HMPAO (Ceretec; GE Healthcare, Buckinghamshire, UK). An ictal scan was performed by injecting the radiotracer within 30 seconds from the onset of seizure. Datasets were acquired in a 128 \times 128 byte matrix (Q matrix) over 360°, with 120 views obtained at 3° intervals for 40 seconds per view (energy setting of 140 keV). Images were reconstructed with the Astonish advanced reconstruction algorithm with an iterative 3D-ordered subset expectation maximization algorithm and built-in corrections for resolution recovery, scatter correction, and attenuation correction. Images of SPECT were co-registered to MRI fast spoiled gradient-recalled images (when available). Reconstructed transversal, sagittal, and coronal images were visually evaluated blinded to the results of EEG findings. The regions of ictal scans that showed increased

perfusion with respect to other brain regions indicated the lateralization or localization of a primary epileptic focus.

3.5.5 Electroencephalographic Source Analysis

3.5.5.1 Data Pre-processing

Automated quantitative analysis techniques, such as ESI, are influenced negatively by the signal intensity inhomogeneity or bias field effect in MRI. Such inhomogeneity of all the MRI scans was corrected with the Freesurfer image analysis suite. Moreover the software was also used for obtaining uniform voxel size ($1\text{mm} \times 1\text{mm} \times 1\text{mm}$) and Right Anterior Superior (RAS) orientation by revising the raw MRI scans.

One of the major difficulties of source modeling through surface ictal EEG is the inevitable presence of various artifacts. Because most of the ictal rhythmic events are of 3-29Hz (Gotman, 1982; Jung et al., 2009), a narrow band-pass filter of 1 Hz to 30 Hz was used to minimize these obscuring artifacts and thus improve the SNR. No such extra band-pass filter was used for preprocessing the interictal EEG records because the epochs having significant artifacts were excluded from the interictal analysis. With the help of power density spectrum and visual inspection, individual channels (T6 for patient 2, Fp1 and Fp2 for patient 3, C4 for patient 4, and P4 for patient 8) having excessive artifacts were identified and then eliminated from both ictal and interictal source analysis.

3.5.5.2 Epoching and Averaging

The time points of interictal spikes and ictal onset rhythms or spikes, as classified by Foldvary et al. (2001), were determined by an experienced epileptologist through visual inspection of scalp-recorded video-EEGs and their filtered outputs respectively. At least 10 interictal spikes (<70 milliseconds) or sharp waves (<200 milliseconds) that were isolated (i.e. no similar discharge within ± 500 milliseconds), were selected and marked

for each patient's interictal analysis. Epochs of ± 100 milliseconds (Kaiboriboon et al., 2012; Koessler et al., 2010) around those marked time points were used for interictal analysis. Ictal epochs of each patient were acquired from the EEG segment that was recorded during the seizure, had evolution of ictal rhythms, and in which the radioactive tracer for SPECT was injected. The channel with ictal rhythms (or spikes) and maximum power density around the rhythm frequencies was considered as the prominent channel. At least 10 non-overlapping 200-millisecond epochs were included in each patient's ictal analysis so that the center time point of each epoch holds the negative maximum peak of an ictal event of the prominent channel. Figure 3.2a illustrates the ictal EEG of patient 2. The EEG segment within the green box is the region of interest. Ictal events were selected from this region. Power spectrum density of each channel, measured throughout the region of interest, is shown in Figure 3.2b. Ictal rhythm frequency within the region of interest was around 6 Hz and the channel T5 showed the greatest power at 6 Hz; therefore, T5 was considered as the prominent channel for this patient. Figure 3.2c is the magnified view of the region of interest. The vertical lines represent the center time points of the selected ictal events. For the improvement of the SNR, averaging of every selected group of epochs was performed separately (i.e., one average ictal epoch and one average interictal epoch for each patient).

3.5.5.3 Head Modelling

Estimation and imaging of the sources of brain electrical activities comprises the so-called forward modeling and inverse modeling. A known model of head is required for forward modeling. Patient-specific, realistic head models, namely 3-layer BEM head models, were used in this study (Beniczky et al., 2006; Koessler et al., 2010). Necessary segmentation from bias field-corrected MRI scans and thus extraction of scalp, outer skull, inner skull, gray matter and white matter surfaces were performed with BrainSuite

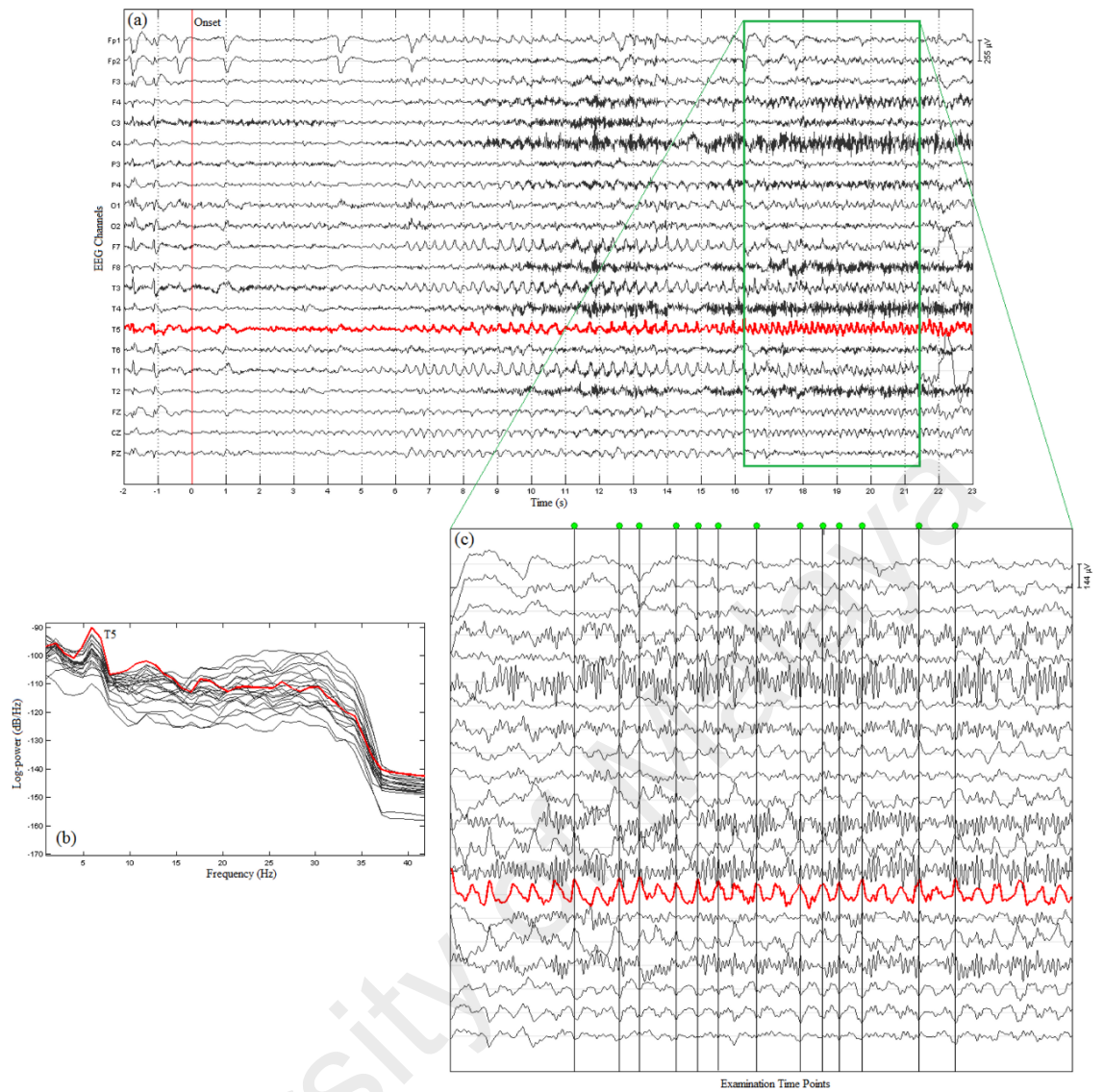


Figure 3.2: Ictal epochs acquisition. (a) Ictal EEG of patient 2, (b) Power spectrum density in the region of interest, (c) EEG segment of interest with centre time points of selected epochs. The channel highlighted in *red* is the prominent channel.

14a (Shattuck & Leahy, 2002). The obtained surfaces of scalp, outer skull, and inner skull were further processed by Brainstorm 3.2 (Tadel, Baillet, Mosher, Pantazis, & Leahy, 2011) to generate nonintersecting BEM meshes with 1922 vertices per layer. Known dipole sources were located in two different source spaces (surface and volumetric) separately. The surface source space considered each vertex of the cortex surface as a dipole source location. On the contrary the volumetric source space used dipole grids that sampled the full brain volume and considered each grid point as a dipole source location. Standard geometrical positions of electrodes, available in

Brainstorm software, were used after manual inspections and necessary alterations according to the surface of each patient's scalp. On the basis of these geometrical descriptions of BEM meshes, source spaces, and the channel positions, two separate forward models (with surface source space and volumetric source space) were computed for each patient with the help of OpenMEEG software (Gramfort, Papadopoulos, Olivi, & Clerc, 2010).

3.5.5.4 Source Localization

Estimation of the unknown sources corresponding to the measured scalp EEG is referred to as inverse modeling. Different inverse modeling approaches were proposed by the scholars, and all of those approaches have some relative merits and drawbacks (Kaiboriboon et al., 2012). Three linear distributed inverse models, known as wMNE, dSPM, and sLORETA were used in this study. Brainstorm implementations of these algorithms were used without any dipole orientation constraint. Source analysis was performed on the average maps of both ictal rhythms (Foldvary et al., 2001) and interictal spikes or sharp waves. The time point at which the source analysis was performed was termed as examination time point (t_0). For ictal and interictal analysis, t_0 represented the time point at which the peak and the 50% rising phase (Ray, Tao, Hawes-Ebersole, & Ebersole, 2007) of the global field power (GFP) occur, respectively. Figure 3.3 illustrates the examination time points on the average maps of selected ictal (Figure 3.3a) and interictal (Figure 3.3b) events of patient 1. Ictal events can be oscillatory-type and spike-type as well (Foldvary et al., 2001). The ictal event of Figure 3.3a is a spike-type ictal event that was selected for the better visualization of various time points.

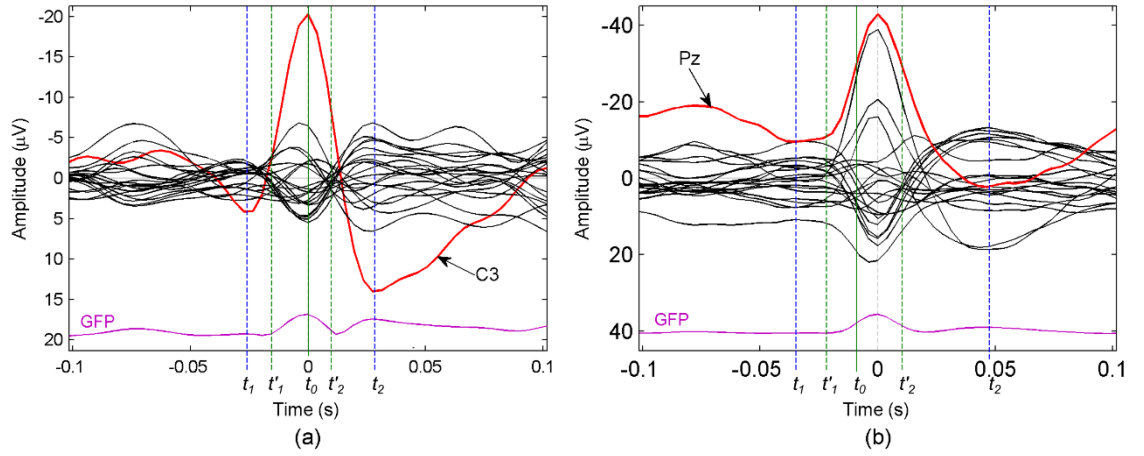


Figure 3.3: Average maps of selected ictal (a) and interictal (b) EEG events of patient 1. Highlighted channel holds the highest amplitude and the time duration from t_1 to t_2 is considered as the event duration. Estimated source at t_0 has been used for final result analysis while stable results have been obtained for all the time points between t'_1 and t'_2 .

3.5.5.5 Stability of Estimated ESI Results

The cortical source of EEG can be estimated for every single time point. An obtained source on a single time point may not be considered as the true source unless the results remain stable for certain duration, because unstable localization can appear in the case of inadequate SNR. Therefore, it is expected that the examination time point and its adjacent time points would estimate the sources in the same or nearby cortical regions. The durations of stable results were measured around the examination time point.

In the average maps of Figure 3.3 the highlighted signals hold the highest amplitude. The time points, t_1 and t_2 , of every average map represent two adjacent local minima of the highlighted signal (around t_0). The time duration from t_1 to t_2 was considered as the event duration. Sources were estimated for every time points starting from t_0 until t'_1 and t'_2 (where $t'_1 \geq t_1$ and $t'_2 \leq t_2$) so that all the estimated sources remained in the same lobe. In addition, the time points next to t'_1 and t'_2 estimated the source in different lobe. The time duration from t'_1 to t'_2 was considered as the duration of stable results.

3.5.5.6 Performance Measure

All the estimated ESI foci were compared with the corresponding SPECT foci. ESI results were considered to be concordant with SPECT results if both ESI focus and SPECT focus were located in the same lobe. Concordance rate was measured as the percentage of concordant results in the total number of considered results. If an estimated ESI focus and the corresponding SPECT focus were found in the same hemisphere, then the estimated result was considered as lateralized.

3.6 Investigation of the Effects of Noise

Ictal EEG measures cortical seizure discharges along with various artifacts, external noises and other background brain oscillations. These signals can be separated from each other using ICA that decomposes ictal EEG into a series of spatially fixed and temporally independent components. The unwanted components are rejected while the ictal components are extracted for EEG source estimation. The ICs for muscle artifacts, eye movement artifacts and line noise have visually noticeable characteristics (T.-P. Jung et al., 2000; Urrestarazu et al., 2004) and comparatively easy to identify, but the identification of other noises and ictal components is not that straightforward. The scalp voltage topography, activity power spectra and dipole residual variances are the features of the decomposed ICs and these features are usually used to categorize the ICs. The aim of this part of the study was to examine the effects of noise on those three features. Simulated ictal EEG with eleven different levels of noises were used for the purpose.

3.6.1 Ictal EEG Generation

Ictal EEG data were generated using a fixed dipole in a four-shell spherical head model (Berg & Scherg, 1994) with radius of 85 mm. A dipole source of 80 nAm was placed in the mesial temporal lobe as shown in Figure 3.4a. A sinusoidal waveform of 5.7 Hz (Figure 3.4b), which typically arise in patients with mesial temporal lobe epilep-

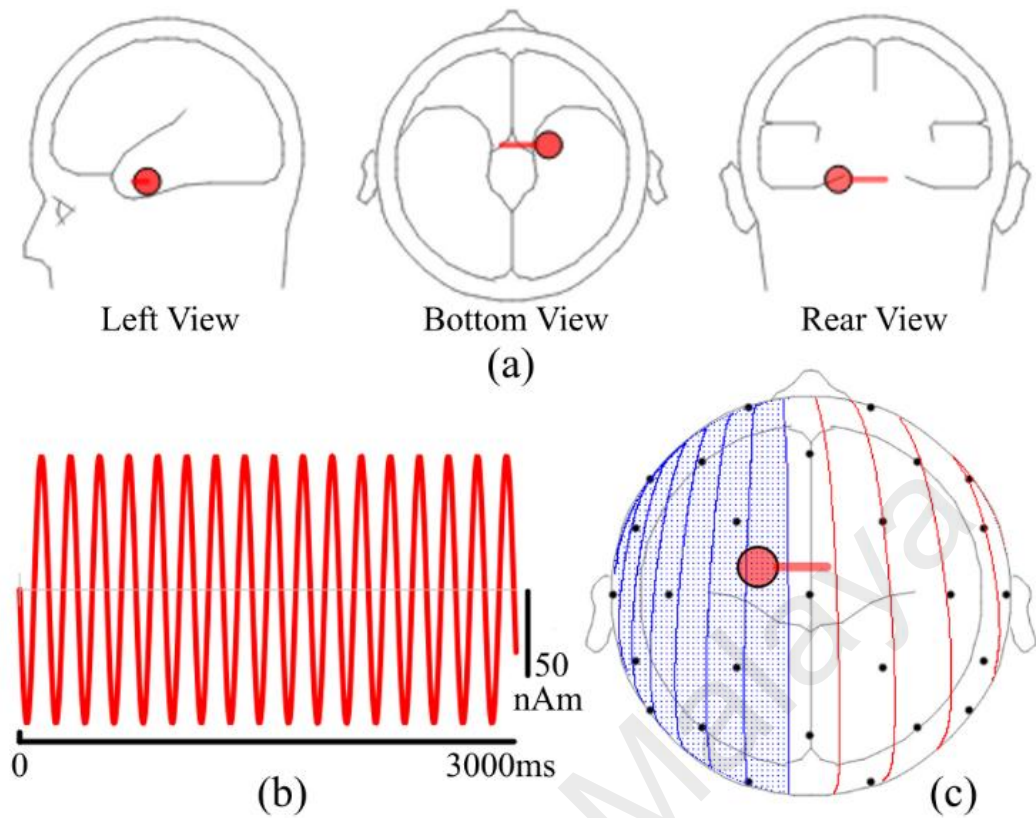


Figure 3.4: (a) Three different views of dipole location and orientation. (b) Source waveform. (c) 2D topographic map.

-sy (De Vos et al., 2007), was used as the source waveform. Thirty three electrodes were used according to 10-10 system. Topographic map of scalp potential distribution, resulting from the dipole source, is illustrated in Figure 3.4c. Scalp potentials on each electrode were obtained by multiplying the source wave by an amplification factor which was computed by solving the forward problem for the dipole source. BESA Simulator and its default values for conductivities and radii of scalp, skull, CSF and brain were used for EEG generation. The simulated EEG data (Figure 3.5a) contained 2 seconds of background EEG followed by 3 seconds of simulated ictal activities. Since no other brain activity or noise was added, initial 2 seconds of EEG were flat. Two seconds of background activities were included because the existing studies (Jung et al., 2009; Lu, Yang, Worrell, Brinkmann, et al., 2012; Yang et al., 2011) on ICA based ictal ESI analyzed both pre and post ictal onset data.

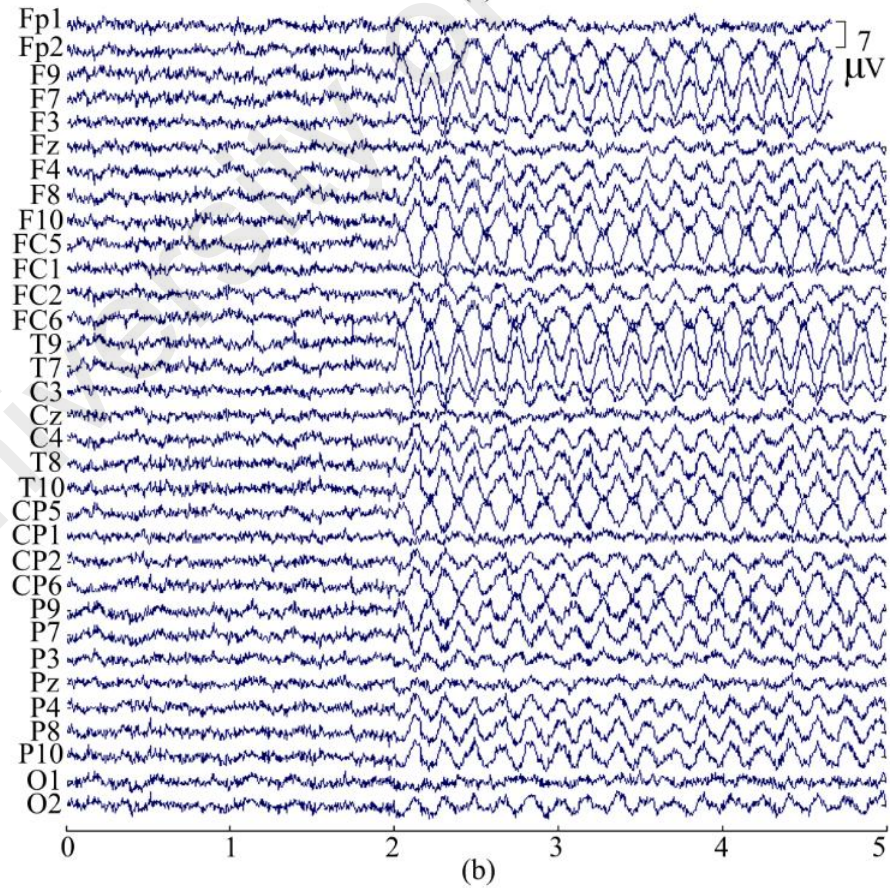
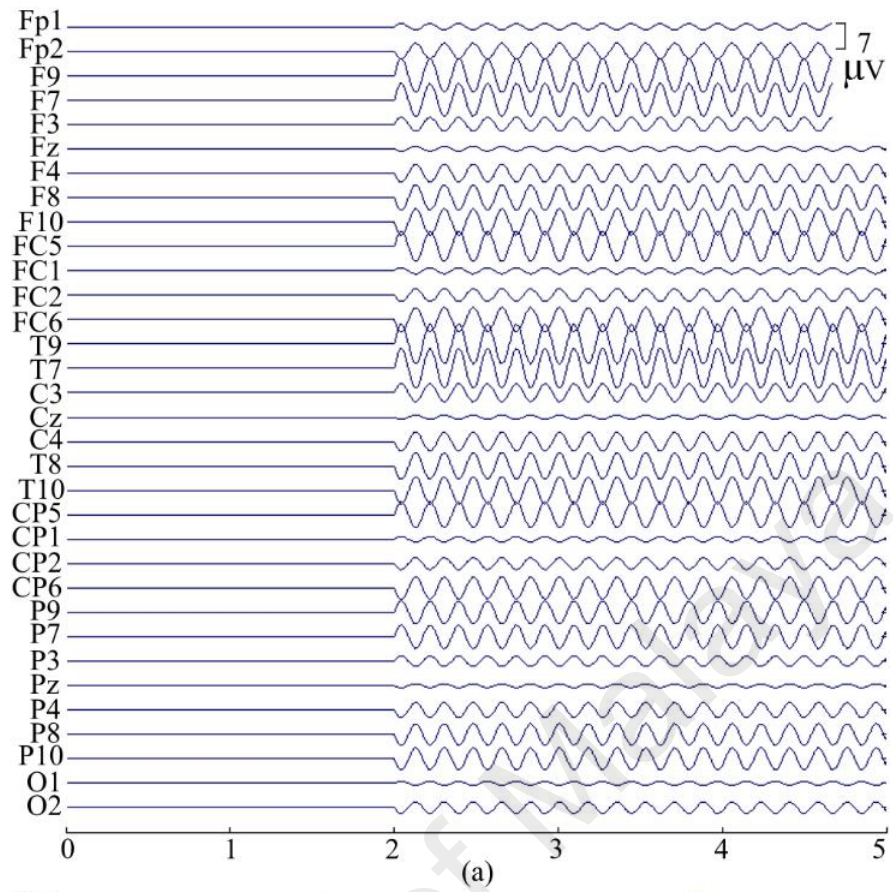


Figure 3.5: (a) Noise free simulated EEG (N0). (b) Simulated EEG (N10) with coherent noise.

The obtained EEG was considered noise free and denoted by N0. The time courses of scalp potentials were stored with sample frequency of 250 Hz. Ten more sets of EEG data were generated in a similar fashion with same dipole source but with ten different levels of coherent noises. The added noises were coherent in the sense that there was quite a high correlation between signal amplitudes from electrodes that were close together. Root mean square values of added noises were 0.1 μV , 0.2 μV , 0.3 μV , 0.4 μV , 0.5 μV , 0.6 μV , 0.7 μV , 0.8 μV , 0.9 μV and 1 μV while the generated EEG signals were termed as N1, N2, N3, N4, N5, N6, N7, N8, N9 and N10 respectively. The last data-set (N10), that contains the highest level of noise, is shown in Figure 3.5b.

3.6.2 Decomposition of Ictal EEG

Each set of simulated ictal EEG was decomposed into 33 temporally independent, but spatially fixed, components. Decomposition was performed by using the open source soft-ware tool EEGLAB Version 13.4.3b (Delorme & Makeig, 2004) and its *runica* algorithm, which was implemented based on the logistic info-max algorithm of Bell and Sejnowski (1995).

3.6.3 Dipole Source Localization of Independent Components

A single equivalent current dipole source and the corresponding residual variance were estimated for each of the ICs by using the DIPFIT function in EEGLAB. A similar head model, as discussed in section 3.6.1, was used for source estimation. The dipoles were plotted on an average MRI template after accomplishing the transposition of dipole locations from the spherical head model to the MRI template. The estimated dipole locations, obtained for the ICs of N0 and N10, are illustrated in Figure 3.6. Since N0 was noise free, its corresponding dipoles overlapped with each other and their residual variances were negligible.

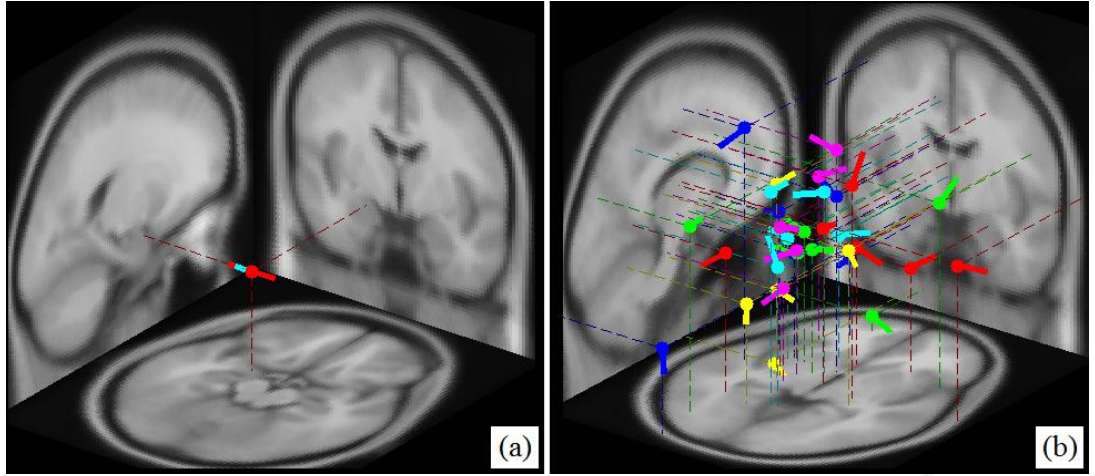


Figure 3.6: (a) Equivalent dipole sources for the ICs of noise free EEG set N0. (b) Equivalent dipole sources for the ICs of N10 having 1 μ V of noise.

3.7 Design and Implementation of the RIDICS Technique

At first a unique quantitative feature of decomposed ictal EEG was derived in this section with necessary mathematical formulations. The RIDICS technique used that new feature and it helped to better identify the ictal components. Detailed description of the RIDICS technique is included in this section. Finally, the proposed technique was validated using both simulated and real ictal EEG data. Validation techniques are explained in this section.

3.7.1 A Quantitative Feature of Ictal EEG Decomposition

The RIDICS technique, aims to find the BIC that has the best correspondence with the rhythmic ictal discharges of the epileptogenic cortical zone. In order to do that, the RIDICS technique uses a unique quantitative feature of ictal EEG decomposition in a number of recursion steps. The background and the mathematical formulations of the quantitative feature are presented below.

An ICA algorithm can decompose the recorded ictal EEG signals (X) into a series of IC time courses (U) as follows:

$$X = AU \quad (3.1)$$

where \mathbf{A} is the “mixing matrix” whose columns contain the relative weights with which the corresponding ICs are projected to the EEG electrodes. If n -electrode EEG records (each having T samples) are considered as the mixtures of m independent components, then \mathbf{X} , \mathbf{A} and \mathbf{U} are the $n \times T$, $n \times m$ and $m \times T$ matrices respectively. The portion \mathbf{X}^p of the ictal record \mathbf{X} is the back-projected EEG for the p^{th} IC and \mathbf{X} is the sum of all such back-projected EEGs:

$$\mathbf{X} = \sum_{p=1}^m \mathbf{X}^p \quad (3.2)$$

According to Equation 3.1 the matrix \mathbf{X}^p is the product of \mathbf{a}_p (the p^{th} column of \mathbf{A}) and \mathbf{u}_p (the p^{th} row of \mathbf{U}) i.e.

$$\mathbf{X}^p = \mathbf{a}_p \mathbf{u}_p \quad (3.3)$$

The above Equation 3.3 implies that the EEG signal of the q^{th} electrode in \mathbf{X}^p can be expressed as the product of the q^{th} element of \mathbf{a}_p and the IC time course \mathbf{u}_p :

$$x_q^p = a_{qp} u_p \quad (3.4)$$

The strength of the ictal rhythm frequency f in \mathbf{x}_q^p can be estimated, using discrete Fourier transform, as follows:

$$\mathcal{F}_{k+1}(\mathbf{x}_q^p) = \sum_{t=0}^{T-1} x_{q(t+1)}^p e^{-2\pi i k t / T} \quad (3.5)$$

where $\mathcal{F}_{k+1}(\mathbf{x}_q^p)$ represents the $(k+1)^{\text{th}}$ discrete value that holds the strength of f in the signal \mathbf{x}_q^p . The symbols k and t are the indices of the discrete values in frequency domain and time domain respectively and both vary from 0 to $T-1$. If the sampling frequency of the signal be f_s , then k can be obtained as $k = fT/f_s$. Moreover, i

represents the imaginary unit ($\sqrt{-1}$). Substituting Equation 3.4 into 3.5 yields the following expression:

$$\mathcal{F}_{k+1}(\mathbf{x}_q^p) = a_{qp} \sum_{t=0}^{T-1} u_{p(t+1)} e^{-2\pi i k t / T}$$

$$\therefore \mathcal{F}_{k+1}(\mathbf{x}_q^p) = a_{qp} \mathcal{F}_{k+1}(\mathbf{u}_p) \quad (3.6)$$

If $\mathcal{F}_{k+1}(\mathbf{X}^p)$ be the column matrix that holds the discrete values of $\mathcal{F}_{k+1}(\mathbf{x}_q^p)$ for all the electrodes ($q = 1, 2, \dots, n$) in \mathbf{X}^p , then according to Equation 3.3 and 3.6:

$$\mathcal{F}_{k+1}(\mathbf{X}^p) = \mathbf{a}_p \mathcal{F}_{k+1}(\mathbf{u}_p) \quad (3.7)$$

Similarly, the strength of f in all the electrodes in \mathbf{X} can be represented by $\mathcal{F}_{k+1}(\mathbf{X})$. Since the Fourier transform is a linear transform, $\mathcal{F}_{k+1}(\mathbf{X})$ can be expressed, on the basis of Equation 3.2, as follows:

$$\mathcal{F}_{k+1}(\mathbf{X}) = \sum_{p=1}^m \mathcal{F}_{k+1}(\mathbf{X}^p) \quad (3.8)$$

If the p^{th} independent component be the BIC, then \mathbf{X}^p contain the highest amount of f -frequency activities with respect to the other portions of \mathbf{X} . If the strength of f is negligible in all the portions of \mathbf{X} , other than \mathbf{X}^p , then Equation 3.8 can be rewritten as:

$$\mathcal{F}_{k+1}(\mathbf{X}) \approx \mathcal{F}_{k+1}(\mathbf{X}^p) \quad (3.9)$$

Substituting Equation 3.7 into 3.9 implies:

$$\mathcal{F}_{k+1}(\mathbf{X}) \approx \mathbf{a}_p \mathcal{F}_{k+1}(\mathbf{u}_p) \quad (3.10)$$

Equation 3.9 and Equation 3.10 show that the strength of ictal rhythm in the BIC-projected EEG has the strongest correlation with that of the recorded ictal EEG.

This quantitative feature has been used in each recursion step of the RIDICS technique. The column matrices $\mathcal{F}_{k+1}(\mathbf{X})$ and $\mathcal{F}_{k+1}(\mathbf{X}^p)$ have been termed as *input rhythm magnitude* (\mathbf{Y}) and *back-projected rhythm magnitude* (\mathbf{Y}^p) respectively for the ease of explanation. Moreover, the term *component rhythm magnitude* (y_p) has been used for representing the discrete value $\mathcal{F}_{k+1}(\mathbf{u}_p)$. All the bold-face symbols including \mathbf{Y} and \mathbf{Y}^p represent arrays while the normal font symbols represent single value.

3.7.2 Recursive ICA Decomposition for Ictal Component Selection

Ideally, the number of independent cortical sources of EEG is nearly unlimited, but practically a limited number of sources, which are large enough, are separated by the ICA decomposition. If the ictal source is not large enough with respect to the noise sources (all sources other than ictal sources), then ictal activities can be either summed into a single IC or distributed into more than one IC (Onton et al., 2006). The RIDICS technique intends to accumulate the majority (or all) of such distributed segments of an ictal component into a single IC by recursive decomposition with noise reduction in each recursion cycle. The major steps of the RIDICS technique are depicted in the simplified flowchart of Figure 3.7.

The recursion base case starts with the EEG epoch that contains mostly (or totally) the post-onset EEG. Pre-onset EEG-inclusion is optional and if included, then the pre-onset data-length needs to be at best one third of the total epoch-length. If necessary, multiple (but as few as possible) segments (with fewer artifacts) of pre-onset and post-onset EEG data can be concatenated for obtaining the input EEG epoch. Initially the input EEG epoch passes through a wideband bandpass (1-45 Hz) filter that removes unwanted signals mostly originated from extracerebral origins. Before decomposing this filtered EEG epoch into ICs, the input rhythm magnitude \mathbf{Y} is computed by using the fast Fourier transform. The electrode with the highest corresponding value in \mathbf{Y} is identi-

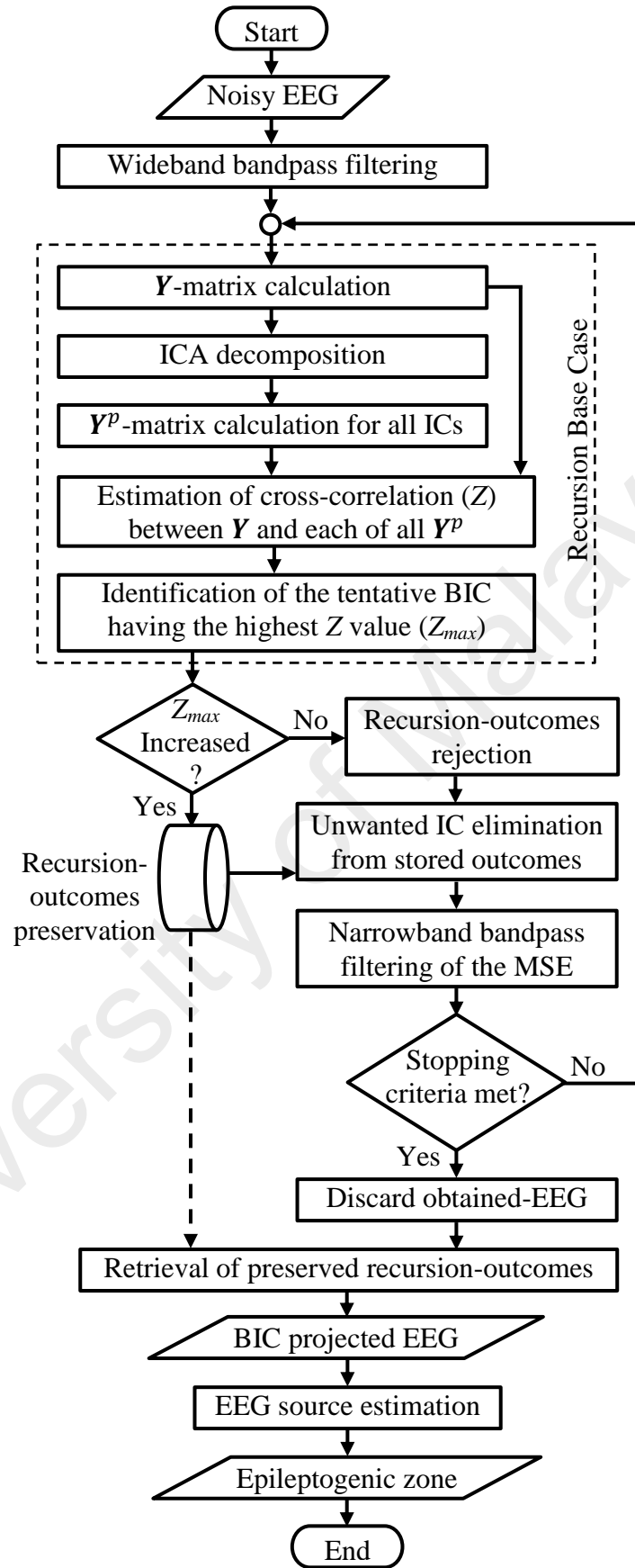


Figure 3.7: Simplified flow chart of RIDICS technique.

-fied and defined as the most significant electrode (MSE). After that the ICA-decomposition is performed. This step decomposes the input dataset into n number of components where the number of electrodes in the input EEG is also n . The next step computes the back-projected rhythm magnitude Y^p for all the components ($p = 1, 2, \dots, n$) by using the Equation 3.6. The zero-lag cross-correlation (Z) between Y and each of Y^p matrices are estimated in the following step. The component with the highest Z value is identified as the tentative BIC at the succeeding step.

This base case is repeated for all other recursion cycles. If there is no improvement in the Z_{max} value with respect to that of the previous recursion cycle, then the decomposition results are discarded, otherwise those are stored for further use. Both conditions lead to an IC elimination step that eliminates one unwanted IC from the stored improved-decomposition results. The MSE of this regenerated back-projected EEG is passed through a narrowband bandpass filter and the resultant-EEG is used as input for the next recursion cycle while not meeting the stopping criteria. The recursion continues until any of the following two conditions (stopping criteria) is met: (1) the Z_{max} value doesn't increase for $(n-1)$ consecutive recursion cycles, where n is the total number of components. (2) the value of Z_{max} exceeds the 75% of the autocorrelation value of Y . Whenever any stopping criterion meets, the last generated EEG dataset is discarded and the last stored decomposition results are retrieved. A set of back-projected EEG, which is used for the epileptogenic zone estimation, is regenerated from the BIC. Finally, the cortical sources of the obtained EEG are estimated by using the sLORETA inverse model. Since the BIC is a temporally independent specially fixed independent component, the inverse solution gives a single cortical source for the whole duration of the BIC projected EEG. The RIDICS technique considers this cortical source as the epileptogenic zone.

In the IC elimination step, an unwanted IC is selected based on the Z values of the ICs. The IC with the lowest Z value is the first discardable component, while the IC with the next lowest Z value is the next discardable component and so on. The first discardable component is eliminated for every improving recursion cycle whereas the first to the r^{th} discardable components are eliminated for the r^{th} cycle of r consecutive deteriorating recursions ($r = 1, 2, \dots, n-1$). In the MSE filtration step, only the signal of MSE is filtered instead of conventional all channel filtration for improving the degraded rank of the regenerated dataset matrix. The bandwidth of the narrowband bandpass filter is chosen to be $\sim 5\text{Hz}$ ($f-2\text{ Hz}$ to $f+2\text{ Hz}$) around the ictal rhythm frequency f . The RIDICS technique was implemented in MATLAB R2013a (MathWorks, Inc., Natick, Massachusetts, USA). Two validations of this technique were carried out: the first for simulated ictal EEG datasets and the other for the real patients' EEG datasets.

3.7.3 Simulated Ictal-EEG Generation

Simulated ictal EEG data were generated by using a fixed dipole in a four-shell spherical head model consisting of scalp, skull, CSF and brain (Berg & Scherg, 1994). Outer radii of these compartments were chosen to be 85, 79, 72, and 71 mm respectively while their conductivities were chosen to be 0.33, 0.0042, 1, and 0.33 mho/m respectively (MacKinnon, Verrier, & Tatton, 2000; Tenke & Kayser, 2015). A dipole source (Figure 3.8a) with 250 nAm moment and rhythmic sinusoidal 6 Hz ictal pattern (Figure 3.8b), which is common in medial temporal lobe epilepsy (De Vos et al., 2007; Nam et al., 2002), was placed in the right temporal lobe. In Cartesian coordinates, the exact location of the dipole was: $x = 58.65$, $y = 16.575$ and $z = -3.91$. Scalp potentials were computed at thirty three electrode-locations, arranged according to 10-10 system, by multiplying the source wave (of the dipole) with an amplification factor that was computed by solving the forward problem for the dipole source. The time courses of the scalp potentials were stored with sampling frequency of 500 Hz.

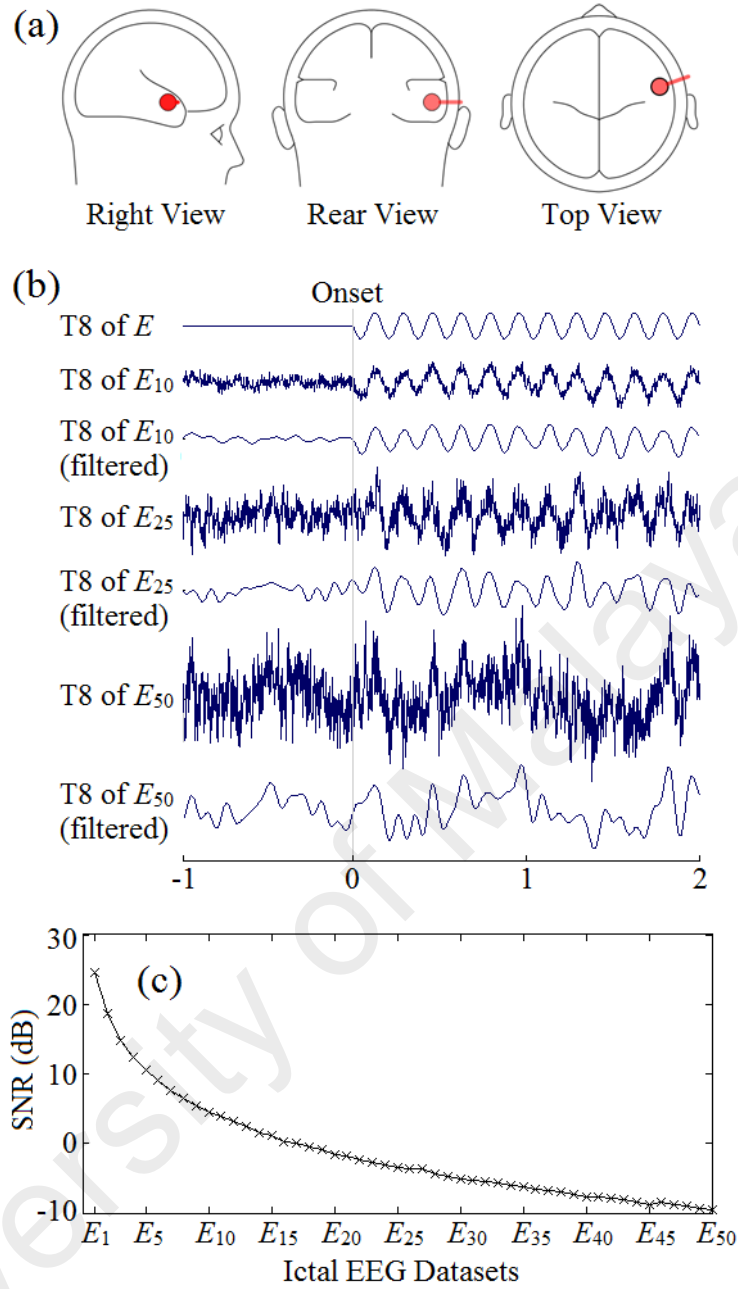


Figure 3.8: (a) Three different views of the location and orientation of the dipole. (b) Changes of MSE signals with the increase of added noises. (c) The SNRs (in decibel) of the MSE signals of the simulated EEG datasets.

In case of n -electrode data at least $k \times n^2$ data points are needed to obtain reliable ICA decompositions, where k is the multiplication factor and the recommended value of k is 20 (Groppe, Makeig, & Kutas, 2009; Onton et al., 2006). Therefore, 22,000 data points or 44s of EEG data were generated for reliable ICA analysis. Since, ictal ESI studies (Jung et al., 2009; Lu, Yang, Worrell, Brinkmann, et al., 2012; Yang et al., 2011) usually use both pre and post ictal onset EEG data, 12 seconds of background EEG

followed by 32 seconds of ictal activities were generated. This initial EEG-dataset E contains no noise therefore the pre-onset background activities were represented by zero potential.

Fifty other sets of EEG were generated in a similar fashion with the same dipole source but with fifty different levels of coherent noises. The noise is coherent in the sense that there is quite a high correlation between signal amplitudes from electrodes that are close to each other. Root mean square (RMS) values of the added noises were varied from 1 μV to 50 μV with a regular interval of 1 μV for generating the ictal EEG datasets $E_1, E_2 \dots$ and E_{50} respectively. Three seconds (1 second before onset and 2 seconds after onset) of EEG data on the most significant electrode (T8) of E is shown in Figure 3.8b. The corresponding ictal EEG from E_{10}, E_{25} and E_{50} datasets along with their filtered (1 to 11 Hz bandpass) waveforms are also included in Figure 3.8b for illustrating the effects of the added different levels of noises. All the signals of Figure 3.8b are in the same scale. Simulated EEG datasets were generated by using the BESA Simulator Version 1.1.0 (BESA GmbH, Germany). Since the simulator cannot produce more than 2000 samples of ictal events without adding any interval, eight different epochs of ictal events were concatenated (Lu, Yang, Worrell, Brinkmann, et al., 2012; Yang et al., 2011) for producing 32s of ictal activities. The SNR was calculated for the MSE of each generated ictal EEG dataset. The MSE of E was considered as the desired signal S for SNR calculation. The SNR of j^{th} dataset E_j was computed with the equation adopted from (Raz, Turetsky, & Fein, 1988).

$$SNR_j = \frac{\sum_{t=1}^T (S(t))^2}{\sum_{t=1}^T (S_j(t) - S(t))^2}$$

where S_j is the MSE of E_j and $j = 1, 2, \dots, 50$. The data point $t = 1, 2, \dots, T$ and the total data points $T = 22,000$ for all the simulated datasets. The SNR values, obtained for all the simulated datasets, are illustrated in Figure 3.8c.

3.7.4 Validation Using Simulated Data

Each of the 50 sets of simulated ictal EEG was decomposed into 33 independent components. The ICA decompositions were carried out by using an extension of the Infomax algorithm of Bell & Sejnowski (Bell & Sejnowski, 1995) as implemented in the *runica* function of the EEGLAB toolbox (Delorme & Makeig, 2004). One BIC for each dataset was individually identified by using RIDICS technique as well as by means of PSD-based and TFR-based techniques. All the Fourier transform operations of RIDICS technique were performed on the ictal activity portion (32s) of each EEG dataset. The PSD-based ictal component selection (PSDICS) technique was adopted from (Nam et al., 2002), where the IC that holds the highest proportion of power in 2-10 Hz bandwidth (for 6Hz ictal rhythm) was considered as the BIC. The TFR-based ictal component selection (TFRICS) technique compares the TFR of each IC with the mean TFR, obtained from the EEG records of three significant electrodes. This technique was adopted from (Yang et al., 2011) where EEG data were passed through a 1–70 Hz band pass filter, and a surrogate method was used for quantifying the significance of the correlation between two TFRs. The ICs that exceed a statistical threshold (p -value) were considered as seizure components. This threshold value is not fixed and it also needs further assistance of visual inspection (Yang et al., 2011). Therefore, instead of using surrogate method, two-dimensional correlation (Rankine, Stevenson, Mesbah, & Boashash, 2005; Reyes, Charleston-Villalobos, Gonzalez-Camarena, & Aljama-Corrales, 2008) has been used in this study to assess the similarity between two TFRs.

The performances of the three selected techniques (RIDICS, PSDICS, and TFRICS) were quantitatively evaluated against two references, namely the noiseless simulated ictal EEG dataset (E) and the original location of the current dipole (D) that produced the simulated ictal activities. The back-projected EEG datasets ($E_{\text{BIC1}}, E_{\text{BIC2}}, \dots, E_{\text{BIC50}}$) were regenerated from the BICs of the corresponding simulated datasets ($E_1, E_2 \dots$ and E_{50} respectively). Each of those back-projected datasets was compared with E through their zero-lag cross-correlations. The BIC that produced higher zero-lag cross-correlation with E was considered as the more accurate BIC. Moreover each selected BIC was modeled as an equivalent current dipole D_{BIC} and the Euclidean distance between D and D_{BIC} was computed. The BIC with shorter distance was considered as the better selection of BIC. The dipole estimations were conducted by using the DIPFIT2 plug-in of EEGLAB. The 4 shell spherical head model that was used for simulated-EEG generation was also used for dipole estimation.

3.7.5 Patients and data acquisition

This study was conducted with the use of anonymized retrospective data, and the study protocols were approved by the University of Malaya Research Ethics Committee (UMREC), Malaysia. Thirty-four patients with drug-resistant focal epilepsy who underwent presurgical evaluation including MRI brain and long-term video-EEG monitoring were selected primarily from the database of the University of Malaya Medical Centre. Eight patients who underwent surgical resections with Engel's class-I surgical outcome were included in this study. The demographics and the diagnosis of the selected patients were summarized in Table 3.2.

Long-term video-EEG recordings were performed with standard EEG setup of 21 electrodes according to the international 10-20 system with additional 2 electrodes at T1 and T2 using NicoletOne EEG/LTM system (Natus Medical Inc., Pleasanton, California

Table 3.2: Demographics and diagnosis results of the patients.

No.	Sex	Age at Onset	Age at Evaluation	Diagnosis
1	M	13	28	Left temporal cortical dysplasia
2	M	12	28	Left MTS
3	M	14	20	Right OLE (lesion negative)
4	M	13	25	Left TLE (lesion negative)
5	M	5	38	Right MTS with bilateral IEDs
6	F	9	42	Left MTS
7	M	12	43	Right MTS
8	M	15	48	Left MTS

-USA). Electrode impedances were kept below 10 k Ω , and sampling rate was set to 500 Hz (250 Hz for patient 6 and patient 8). Seizures range. 1 - 4 were recorded in all patients.

Anatomical details of every patient's head were obtained from their corresponding MRI brain scans. Those details were used for generating patient-specific head models. Structural MRI scans were performed with a Signa HDxt 3.0T scanner (General Electric Healthcare, Wauwatosa, Wisconsin, USA).

3.7.6 Validation Using Real Data

An EEG epoch of at least $20 \times n^2$ data points was accumulated from each seizure of every patient for ICA decomposition. It consists of at most one third pre-onset EEG and at least two third post-onset EEG. Multiple segments of EEG, which contain relatively less eye-blink and movement artifacts, were concatenated for obtaining the EEG epoch. Ictal rhythm frequency f was identified from the post-onset portion of this epoch. Since, both frequency and cortical source location of ictal rhythm may change with time, careful selection of f is very important for the success of the RIDICS technique. In this study, f was selected through PSD analysis of a 2 to 12 second segment of the EEG epoch. Such a segment was selected from that portion of the EEG epoch where ictal rhythm started to become visible (i.e. close to the ictal onset), f remained almost

unchanged and no significant eye blink artifact existed. Three BICs for three selection techniques (RIDICS, PSDICS and TFRICS) were identified for each real dataset and by following the same procedure as discussed for simulation-based validation. Back-projected EEG was regenerated for each of the selected BICs and the obtained EEG datasets were supposed to represent noise free ictal EEG. Those datasets were considered as the preprocessed data while estimating the EEG sources by following the steps as shown in Figure 2.4.

The epileptogenic zone was estimated for each of those regenerated EEG datasets by following the procedure explained in (Habib et al., 2016). Subject specific realistic head models were generated from the corresponding MRI scans by following the procedure explained by Habib, Ibrahim, et al. (2014) and by using the BrainSuite software tool. The source model, channel locations and the forward solution techniques were accomplished according to the approach proposed by (Habib et al., 2016). The linear distributed inverse model sLORETA was used for inverse solution. Epoching and averaging were not necessary, because each EEG dataset was obtained from a single IC that was temporally independent and specially fixed. Therefore, estimated sources remained fixed with respect to time.

All the estimated ESI foci were compared with their corresponding sites of cortical surgery. Each ESI result was considered to be concordant with the surgery site if both ESI focus and surgery site were located in the same lobe. Concordance rate was measured as the percentage of concordant results in the total number of considered results. If an estimated ESI focus and the corresponding surgery site were found in the same hemisphere, then the estimated result was considered as lateralized.

CHAPTER 4: RESULTS AND DISCUSSIONS

4.1 Introduction

This chapter presents the results obtained after accomplishing each of the steps discussed in the previous chapter. The results are organized according to the sequences of the steps. Firstly the comparison results of open-source software tools for head model generation are provided. Next the results obtained from the evaluation of clinical utility of an ictal ESI technique with the application of three different inverse solutions are discussed. Then the outcomes of investigating the effects of noise on the features of decomposed EEG are summarized. After that the validation results of the RIDICA technique are presented. Brief discussions on the results are also included accordingly.

4.2 Comparison of Software Tools for Head Model Generation

Comparative investigation of five selected software tools, for MRI segmentation and surface generation, were carried out (as explained in Section 3.4) based on their declared features and real data analysis. Investigation outcomes are presented below.

4.2.1 Comparison Based on Stated Features

Various features of the software tools were mentioned in their official website and some relevant published articles. Some of those features that are important for general users are compared in this subsection. One of the important features that are needed before working with a software tool is its system requirement. Table 4.1 lists the system requirements of the selected software tools. It shows that all the tools can run on both Windows and Linux OS, but MATLAB should be there for running FieldTrip and NFT. The BrainVISA tool was not tested on the latest versions of Windows. Practically, it was found malfunctioning on Windows 8.1 platform. Moreover NFT and FreeSurfer recommended highest amount of system memory for proper operation.

Table 4.1: System requirements of the selected tools.

Software Tool	Minimum System Requirement	
	Operating System (OS)	System Memory
FieldTrip	Run under MATLAB platform that is running under any OS.	Not specified. Depends on size of data.
NFT	Not specified. Depends on size of data.	At least 2 GB (4-8 GB recommended)
BrainVISA	Tested and found functional on Linux (Ubuntu 10.04, Fedora 4-9, RedHat 9, Mandriva 2007 & 2007) Mac OS (10.4 & 10.5), Windows (XP, NT, 2000).	Not specified. Depends on the size of data.
BrainSuite	Windows and Mac OS. BrainSuite Diffusion Pipeline (bdp) also run under Linux.	bdp requires 6 GB
FreeSurfer	Linux, Mac OS, Windows (via VirtualBox only).	8GB (recommended)

The MRI scans are available in various data formats. Therefore, knowing the supported input and output file formats were also important for the users. Table 4.2 presents the MRI file formats that are supported by the selected tools. It shows that BrainVISA and FreeSurfer provide huge flexibility in MRI data format. In fact these two tools had their own built-in MRI converters. NFT could work on *Analyze* format only and recommended using FreeSurfer's MRI converter for MRI preparation. This table also lists the file formats of the BEM meshes or surfaces generated by the software tools.

4.2.2 Comparison Based on Real Data Analysis

FieldTrip, NFT and BrainSuite worked properly (with the installation and operation) on a machine with Windows 8.1 platform. FreeSurfer needed ORACLE VM VirtualBox support, with the guest operating system Xubuntu 12.04, for functioning on the same Windows machine. Processor speed and system memory of that machine were 2.40 GHz (Intel Core i7) and 16 GB respectively. Since BrainVISA did not run properly on Windows 8.1, it was installed in a different computer having Windows XP OS. That

Table 4.2: Input and output file formats.

Software Tool	Supported MRI Formats	Generated BEM Surface File Format
FieldTrip	CTF - VSM MedTech, NIFTi, Compressed NIFTi, Analyze, DICOM, AFNI, FreeSurfer, MINC, Neuromag – Elekta, ANT, Yokogawa	MATLAB (*.mat)
NFT	Should be in Analyze format and the voxel size should be (mm) 1×1×1.	*.smf & *.mat
BrainVISA	PNG image, XBM image, XPM image, TIFF image, TIFF(.tif) image, PPM image, GIF image, JPEG image, BMP image, PBM image, PGM image, MNG image, SPM image, GIS image, VIDA image, ECAT v image, ECAT i image, DICOM image, MINC image, compressed MINC image, NIFTI-1 image, compressed NIFTI-1 image	*.gii & *.minf
BrainSuite	Works best with NIfTI format, but also provides limited support for DICOM images	*.dfs
FreeSurfer	MGH-NMR COR, MGH-NMR MGH-NMR (compressed), MNI's Medical Imaging NetCDF, 3D analyze, 4D analyze, SPM Analyze, GE Genesis, GE LX, GE XIMG variant, Siemens IMA, generic DICOM, Siemens DICOM, AFNI, MGH-NMR bshort, MGH-NMR bfloat, MGH-NMR Outline, GDF volume, NIfTI-1, compressed NIfTI.	*.curv

machine had 1.80 GHz Intel Core 2 Duo processor and 2 GB system memory. All of the five selected software tools were used for generating BEM meshes or surfaces from each of the five MRI datasets.

BrainSuite and FreeSurfer generated head models for all of the five datasets and without any error message. During outer skull segmentation, NFT removed the eyeball regions from the skull. The eyes were extracted by region growing technique from the user-indicated points (Acar & Makeig, 2010). Since some parts of the eyeball regions of the selected datasets were removed during de-identification process, NFT gave an error message while segmenting the outer skull. Simple modification of NFT code, i.e. by omitting that error message generation instruction, made it functional. After that

modification, NFT performed the segmentation and surface generation tasks for all of the five datasets. FieldTrip crashed while simulating the MRI dataset of the 5th subject only, whereas BrainVISA crashed on processing 2nd and 5th subjects' datasets. The 3rd set of MRI data, which was successfully processed by all of the five software tools, is shown in Figure 4.1.

All the default parameters and settings of the software tools, except the number of vertices of NFT, were kept unchanged during both segmentation and surface generation processes. With default parameters and settings FieldTrip and BrainSuite generated five simulated surfaces (scalp, skull, CSF, WM and GM) for each MRI dataset. White matter was not segmented by NFT. It produced brain surface that actually resembled the GM. BrainVISA and FreeSurfer did not produce surfaces for skull and CSF. Those tools were more concern about cortical surface generation. Figure 4.2 illustrates all the surfaces generated by all of the five software tools from the same MRI dataset that is shown in Figure 4.1. Visual observation provided that the scalp, GM and WM generated by BrainVISA were most realistic. Besides, skull and CSF images produced by NFT were more accurate. FieldTrip-generated surfaces were sometimes incomplete or inaccurate as shown in Figure 4.2.

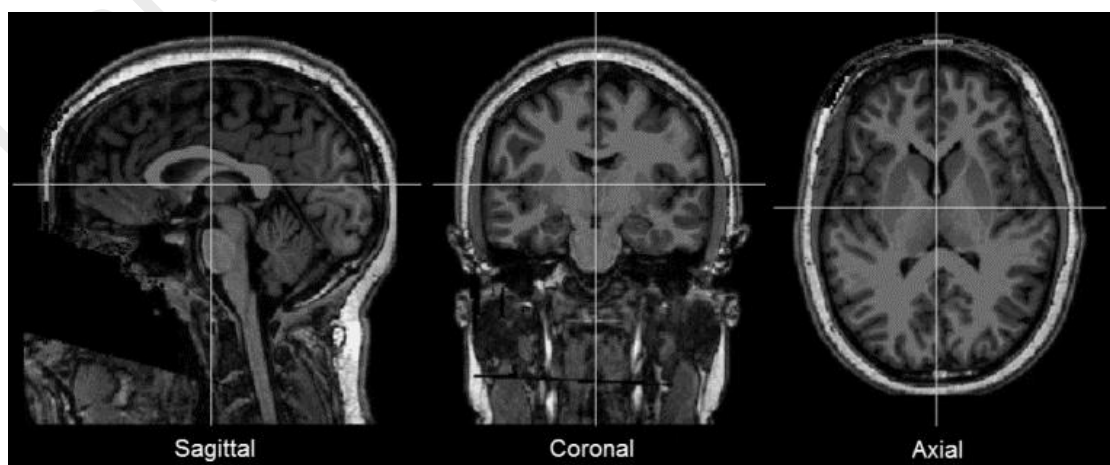


Figure 4.1: MRI scan of a subject (3rd dataset).



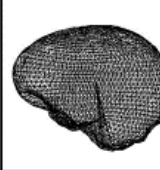
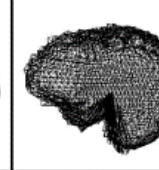
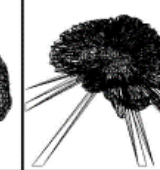
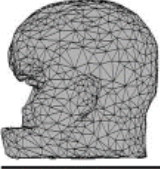
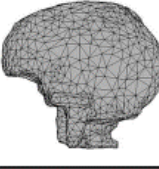
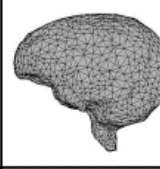
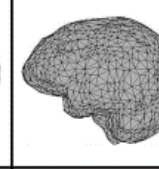
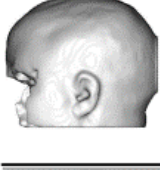
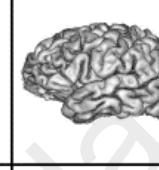
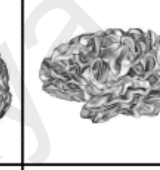

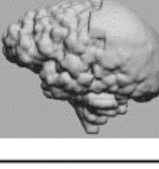
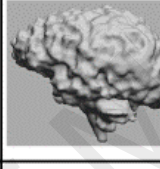
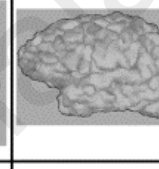
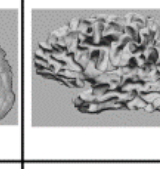
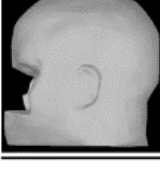
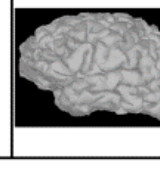
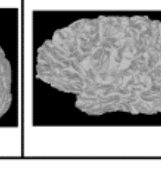
Software Tools	Scalp	Skull	CSF	Grey Matter	White Matter
FieldTrip					
NFT					Not Found
BrainVISA		Not Found	Not Found		
BrainSuite					
FreeSurfer		Not Found	Not Found		

Figure 4.2: Surfaces generated from 3rd MRI dataset.

Among all the software tools, FreeSurfer and BrainSuite performed the MRI segmentation and surface generation processes without any user's feedback. FieldTrip needed user's feedback for finding the orientation of the input MRI. While using NFT for brain segmentation, user had to select the lowest point of the cerebellum and a WM seed point manually. Moreover, for outer skull segmentation, NFT required user's input for identifying the center of eyeballs. In order to use BrainVISA, user had to provide the coordinates of the anterior commissure, posterior commissure, interhemispheric point and the left hemisphere point or had to locate those points on the MRI scan. Execution times of the selected software tools were not included in the comparison, because the tools ran on different hardware and operating systems. Moreover, the number and types of operations were different from one tool to another.

4.2.3 Head Modelling Tool Selection

Five well known free software tools for MRI segmentation and BEM surface generation were compared. The results showed that none of the tools could be considered as the best. Ranking of the tools was found depended on the user's needs. If less resource (hardware and software) were available, then BrainVISA would be the best choice. If higher number of tissue classes was required, then Brainsuite provided the best. Sometimes source code customization is required along with higher number of tissue class analysis. FieldTrip would be the best option for such cases. BrainSuite was not the right choice because it was not an open-source tool. If more accurate skull surface was vital, then NFT would be the best option. Latest application areas mostly need accurate and reliable cortical surface generation. FreeSurfer could meet that need. In order to select the right tool, users should know the strengths and limitations of these tools. So this comparative study of the latest tools with practical implementation results would be a helpful guide for the users. All of the five tools could produce better outputs with adequate adjustments of default parameters and settings, but this study considered the outputs that required minimum expertise and involvements of users.

The RIDICS technique required a software tool that could generate reliable and realistic head models with minimum user-involvement. Higher number of head layers produces more realistic model. Therefore, preference was given to the tools that could provide higher number of surfaces. Another issue that was important for RIDICS technique was the compatibility issue. The RIDICS technique used the head model for forward and inverse solutions; therefore the file format of the head model needed to be compatible for the forward and inverse solution software. Considering all those requirements, BrainSuite was selected for the head model generation step of the RIDICS technique.

4.3 Clinical Utility of Ictal ESI

Epileptogenic foci were estimated from real patients' data by using a classical (non-ICA based) ESI technique and open-source software tools. The results obtained were analyzed from various points of view and the best performing inverse solution was selected for RIDICS technique. All those results and analysis are presented in this section.

4.3.1 Source Estimation

Figure 4.3 illustrates the SPECT results and corresponding ESI results of two patients (patient 2 and patient 3). These two sets of results were selected so that all the ESI results of one patient (patient 2) were fully concordant with SPECT results, whereas the ESI results of the other patient (patient 3) were not in all cases concordant with SPECT result. All the ESI results and the SPECT results of patient 2 showed that the epileptic focus was located in the left occipital lobe. Therefore, all the ESI results of patient 2 were considered concordant with the SPECT result. According to the SPECT results of patient 3, the epileptic focus was located in the right parietal lobe. Obtained ESI results showed that only ictal analysis through dSPM estimated the focus in the same lobe.

The sLORETA analysis of ictal events, which estimated the focus in the lateral sulcus of Sylvius of the same hemisphere, also was considered concordant. Other ESI results of patient 3, although estimated the focus in the adjacent lobe (temporal lobe and insular cortex), were not considered concordant with SPECT result. The volume of ESI focus was threshold dependent. Different threshold values were chosen for different ESI results for better visualization and easier localization of the regions with maximum current density. Therefore, the volumes of ESI foci, highlighted in red in Figure 4.3, did not provide information on the extent of epileptogenic zone. These highlighted regions

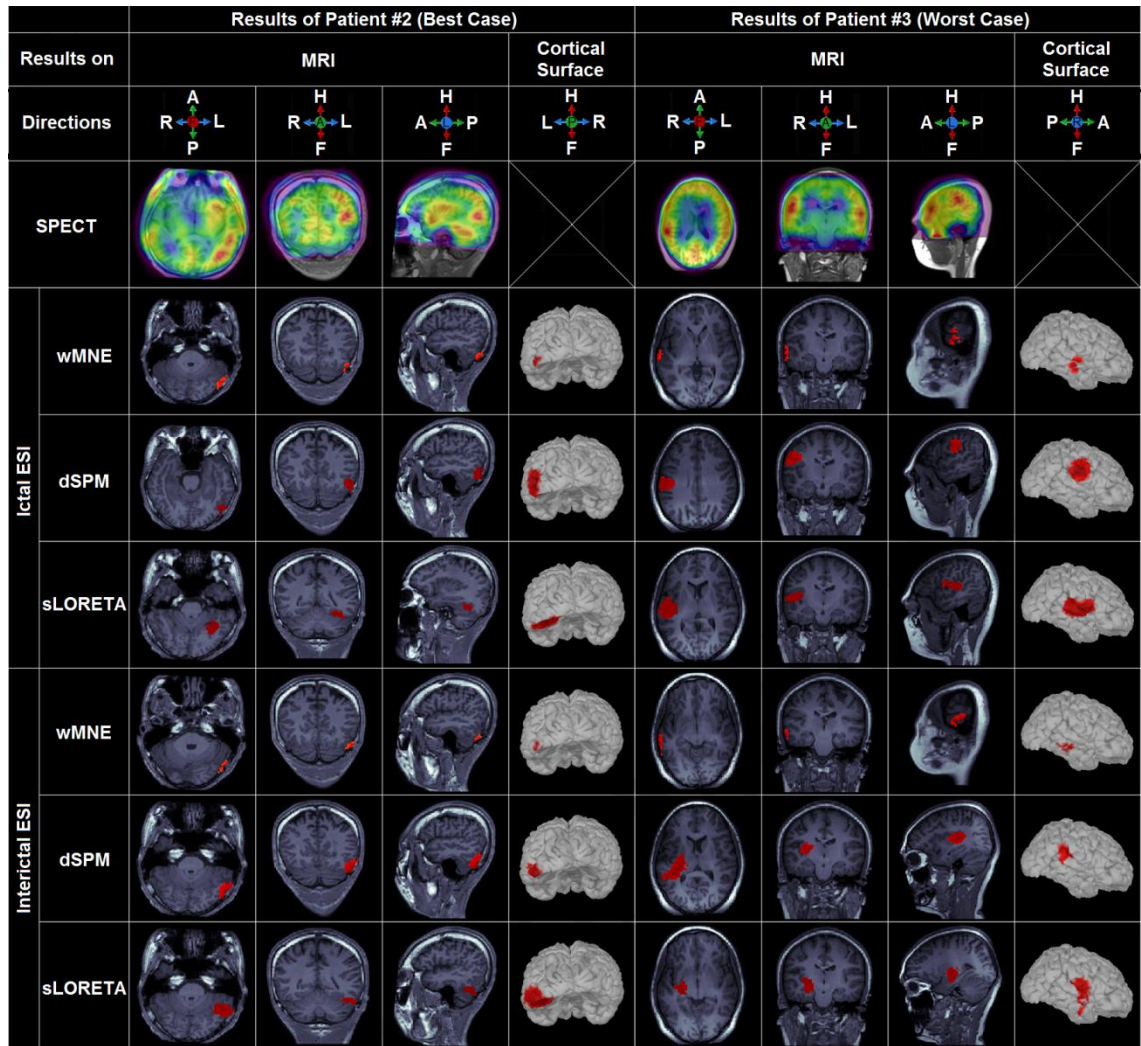


Figure 4.3: SPECT results and corresponding ESI results of two patients (patient 2 and patient 3). ESI sources, estimated by using volumetric source space and surface source space, have been presented on magnetic resonance imaging and simulated cortical surfaces respectively. Cortical regions with red color represent the estimated epileptic foci.

represented the brain volumes that contained the maximum current density sources.

Cortical locations of all the 8 patients' electroencephalographic sources along with the positions of their corresponding SPECT foci and MRI lesions are listed in Table 4.3. ESI with surface source space and volumetric source space estimated the sources in the same sublobe. The only difference was that the surface source space based analysis always estimated the sources on the gray matter whereas the volumetric source space

Table 4.3: Cortical locations of MRI lesions, SPECT-foci and the ESI-foci of all the patients.

#	MRI lesion	SPECT	Ictal ESI			Interictal ESI		
			wMNE (t ₂ ' - t ₁ ')	dSPM (t ₂ ' - t ₁ ')	sLORETA (t ₂ ' - t ₁ ')	wMNE (t ₂ ' - t ₁ ')	dSPM (t ₂ ' - t ₁ ')	sLORETA (t ₂ ' - t ₁ ')
			EEG ictal pattern: Spikes					
1	L Postcentral G	L superior parietal Lo	L superior parietal Lo (23ms)	L superior parietal Lo (23ms)	L superior parietal Lo (39ms)	L superior parietal Lo (27ms)	L cingulate cortex (31ms)	L superior parietal Lo (27ms)
			EEG ictal pattern: Rhythmic activity					
2	L parieto-occipital S	L parieto-occipital S	L preoccipital notch (22ms)	L parieto- occipital S (24ms)	L lateral occipitotemporal G (24ms)	L preoccipital notch (47ms)	L preoccipital notch (50ms)	L lateral occipitotemporal G (28ms)
3	R paracentral Lo	R Inferior Parietal Lo	R middle temporal G (14ms)	R Inferior Parietal Lo (42ms)	R lateral S of Sylvius (20ms)	R middle temporal G (16ms)	R insular cortex (46ms)	R insular cortex (10ms)
4	No lesion	R occipital Lo	R occipital P (24ms)	R cuneus (28ms)	R medial occipitotemporal G (18ms)	R occipital P (40ms)	R occipital P (40ms)	R lateral occipitotemporal G (22ms)
5	L middle temporal G	L superior temporal G	L temporal P (60ms)	L temporal P (42ms)	L temporal P (78ms)	L temporal P (64ms)	L temporal P (64ms)	L temporal P (68ms)
6	No lesion	R inferior parietal Lo	R inferior parietal Lo (42ms)	R intraparietal S (80ms)	R intraparietal S (36ms)	R inferior parietal Lo (20ms)	R intraparietal S (30ms)	R inferior parietal Lo (22ms)
7	R medial temporal Lo	R temporal P	R temporal P (138ms)	R temporal P (136ms)	R temporal P (134ms)	R temporal P (70ms)	R basal ganglia (50ms)	R temporal P (122ms)
8	L medial temporal Lo	L temporal P	L temporal P (27ms)	L temporal P (20ms)	L temporal P (51ms)	L temporal P (66ms)	L temporal P (63ms)	L temporal P (70ms)

#: Patient Number, L: Left, R: Right, G: Gyrus, S: Sulcus, P: Pole, Lo: Lobe/Lobule, $t_2' - t_1'$: duration of stable results.

based ESI often found the sources in the white matter of the corresponding sublobe. Therefore, the results obtained for surface source space and volumetric source space have not been listed separately in Table 4.3.

4.3.2 Inverse Solution Selection

On the basis of the results listed in Table 4.3, concordance and discordance of the obtained ESI results with SPECT results are summarized in Table 4.4. Ictal analysis results showed that dSPM and sLORETA could locate the ESI focus and the SPECT focus in the same lobe for all of the 8 patients (concordance rate 100%), whereas the results of wMNE were not concordant for patient 3 (concordance rate 87.50%). On the other hand, the results obtained from interictal analysis showed that wMNE and sLORETA estimated concordant results for 7 (except patient 3) of 8 patients (concordance rate 87.50%), whereas the dSPM failed for patients 1, 3, and 7 (concordance rate 62.50%). Among the 3 distributed inverse models, sLORETA gave the greatest concordance rate for both ictal and interictal analysis, whereas for individual inverse model the number of concordant results of ictal ESI was either equal to or greater than that of interictal ESI. All the ESI results were lateralized correctly because all estimated ESI sources were found in the same hemisphere as their correspo-

Table 4.4: Concordance or discordance of ESI results with ictal SPECT.

Patient Number	Ictal ESI			Interictal ESI		
	wMNE	dSPM	sLORETA	wMNE	dSPM	sLORETA
1	√	√	√	√	X	√
2	√	√	√	√	√	√
3	X	√	√	X	X	X
4	√	√	√	√	√	√
5	√	√	√	√	√	√
6	√	√	√	√	√	√
7	√	√	√	√	X	√
8	√	√	√	√	√	√

√: Concordant, X: Discordant.

-nding SPECT sources and MRI lesions (see Table 4.3).

4.3.3 Stability Analysis

The durations (in milliseconds) of stable results around the corresponding examination time points are listed in Table 4.3 for all the ESI analysis. These durations indicated that the ictal analysis through sLORETA produced the results with the longest average duration of stability at 50 milliseconds (median, 37.5 milliseconds; range, 18 – 134 milliseconds). The results obtained for ictal analysis through wMNE remained stable for the shortest average duration at 43.75 milliseconds (median, 25.5 milliseconds; range, 14 – 138 milliseconds). Analysis results through rest of the methods of both ictal and interictal analysis remained stable for average duration of 46.13 milliseconds to 49.38 milliseconds. The overall average duration for ictal analysis results (4.71 milliseconds) was slightly longer (1.13 milliseconds) than that of interictal analysis results (46.58 milliseconds), which supported the acceptability of ictal analysis results. However, longer average duration of stable ictal analysis results was expected, because the event duration ($t_2 - t_1$) of ictal events were usually longer than that of interictal events.

4.3.4 Analysis of Findings

The results demonstrated that all the estimated ictal ESI foci and the corresponding clinically evaluated seizure foci were lateralized to the same brain hemisphere. Furthermore, all the ictal ESI results, except one wMNE analysis result, were concordant with the results of at least 2 other diagnostic modalities (MRI and SPECT). These ESI analyses were conducted with the use of MRI scans and EEG data that were acquired within a standard clinical setup for presurgical evaluation of epilepsy. These findings also supported the argument that ictal ESI could be considered as a potential noninvasive diagnostic tool for the presurgical evaluation of focal epilepsy.

Kovac et al. (2014) reported that ictal ESI, through dipole modeling, produced lateralizing results in 8 of 17 seizures (47%). Significantly improved results of ictal ESI were obtained in the current study, and such improvements were rationalized through the use of patient-specific, realistic head models. The greatest concordance rate previously reported (Koessler et al., 2010) is 90%, which is in agreement with the obtained results of this study. The only article that compared the performance of ictal and interictal ESIs (Beniczky et al., 2006) reported a better concordance rate of ictal ESI over interictal ESI, which further supports the greater concordance rate of ictal ESI obtained in this study.

The evidence in support of interictal ESI (Lantz, Spinelli, et al., 2003; Ray et al., 2007) shows the source estimation time point at the 50% rising phase of GFP. However, to the best of our knowledge, there is no study that recommends the best examination time point for ictal source estimation. Koessler et al. (2010) analyzed all the time points of each selected ictal event and the source with the greatest amplitude across time and space was chosen, i.e., the examination time point was not fixed. For ease of analysis, a generalized examination time point, which is the time point at the peak of GFP, was used in this study for ictal source estimation with reasonable stability (see Table 4.3).

4.3.5 Advantages of Ictal ESI over Ictal SPECT

Another noninvasive diagnostic tool used for the presurgical evaluation of refractory focal epilepsy is ictal SPECT. When ictal SPECT is acquired, a costly radioactive tracer is injected during the onset of seizure. In reality, there is always a latency (3 – 260 seconds) from commencement of the seizure to injection (O'Brien et al., 1999), and the tracer takes around 30 seconds to circulate to the region of interest (Foldvary et al., 2001). This circulatory delay allows the ictal activity to spread to the other regions, i.e., the ipsilateral basal ganglia and the motor cortex. Therefore, the area of hyperperfusion

on ictal SPECT doesn't always represent the seizure focus. In addition, an ictal SPECT scan captures one seizure only and has poor temporal resolution (Jung et al., 2009). In contrast, ictal ESI can easily cover multiple seizures and has greater temporal resolution, which can localize the source for every instant (limited by the sampling rate of EEG recordings) of ictal EEG records. Ictal ESI is thought to be able to distinguish the primary source from the secondary source because of its high temporal resolution (Ding et al., 2007). Moreover, obtaining successful SPECT results demands careful monitoring, trained staff for the early injection of radioactive tracer, and specially trained nuclear medicine technologists to acquire the SPECT scans. Ictal ESI does not need these supportive measures and thus remains less expensive.

4.4 Effects of Noise on the Features of Decomposed Ictal EEG

This section examines the effects of coherent noise on three selected features of the decomposed ICs of ictal EEG. The reason behind selecting these features is their frequent use in the ictal component selection step of ictal ESI techniques. The results of this investigation, presented in the following subsections, justify the derivation of a new feature for ictal component selection.

4.4.1 Topographic Maps

A two dimensional (2D) scalp topographic map is generated for each of the ICs. Corresponding equivalent single dipole sources are also included in the maps. Topographic maps of all the ICs of N0 and N10 are shown in Figure 4.4. Potential distributions for all the components of N0 are found similar to that of the original dipole source shown in Figure 3.4c, except the orientation of the dipole. On the other hand only few maps for N10 show similarity with the original source. Considering all the 2D maps, generated from the ICs of 11 sets of EEGs, it is evident that the number of dissimilar maps per set increases with the increase of noise level. 2D maps for other 9 -

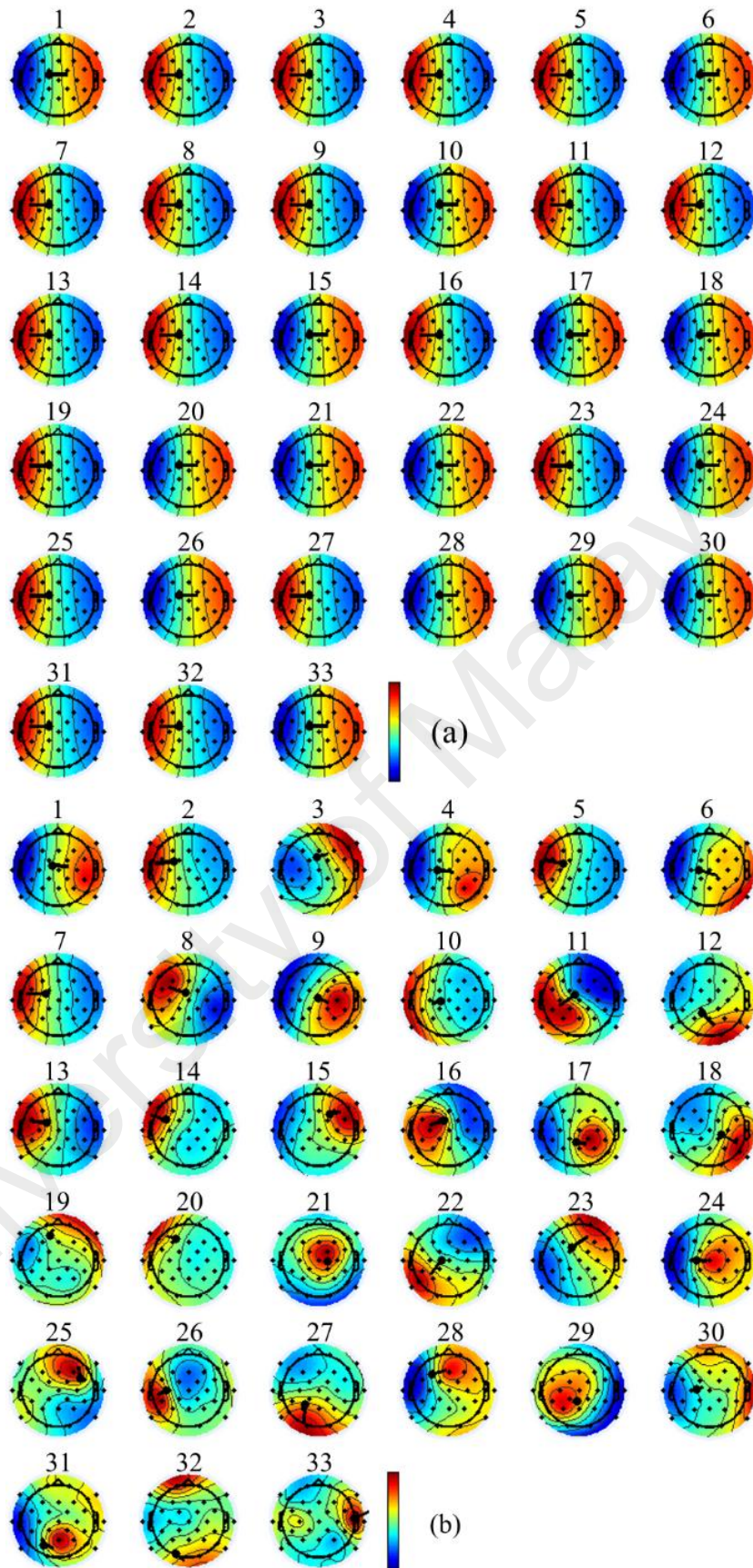


Figure 4.4: 2D topographic maps for all the ICs of (a) N0 and (b) N10. Locations and orientations of corresponding equivalent dipole sources are shown. Color bars next to the maps indicate the magnitude and polarity.

sets of EEGs cannot be included due to space limitation.

4.4.2 Activity Power Spectra

Activity power spectra of ICs exhibit which components contribute most strongly to which frequencies in the data. Power spectra are generated for all the ICs while considering 100% samples and total epoch time range (5 seconds). Component no. 1 of N0 and component no. 2 of N100 has contributed most strongly around the rhythm frequency (5.7 Hz). Power spectra of these two ICs are shown in Figure 4.5. Activity power spectra are generated for all the ICs. The number of ICs that contribute highly around rhythm frequency is found decreasing with the increment of noise.

4.4.3 Dipole Residual Variance

Residual variances are calculated for all the estimated dipole sources of all the ICs and those are shown in Figure 4.6a as a 3D column chart. Higher order ICs are found more likely to have higher residual variances. Average value of the residual variances is also calculated for each set of EEG data and illustrated in Figure 4.6b as a line chart. Although in most of the cases the average residual variance have in-creased with the increment of noise level, opposite relation-ship is also found in few cases.

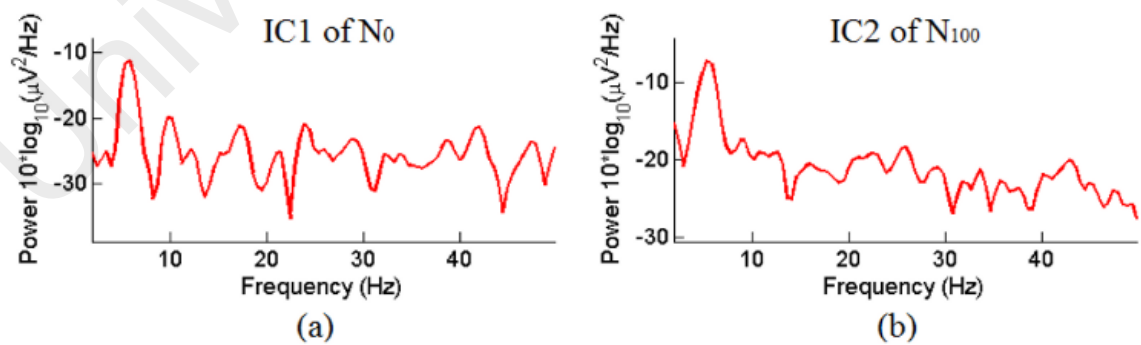


Figure 4.5: Activity power spectrum for (a) IC1 of N0 and (b) IC2 of N100.

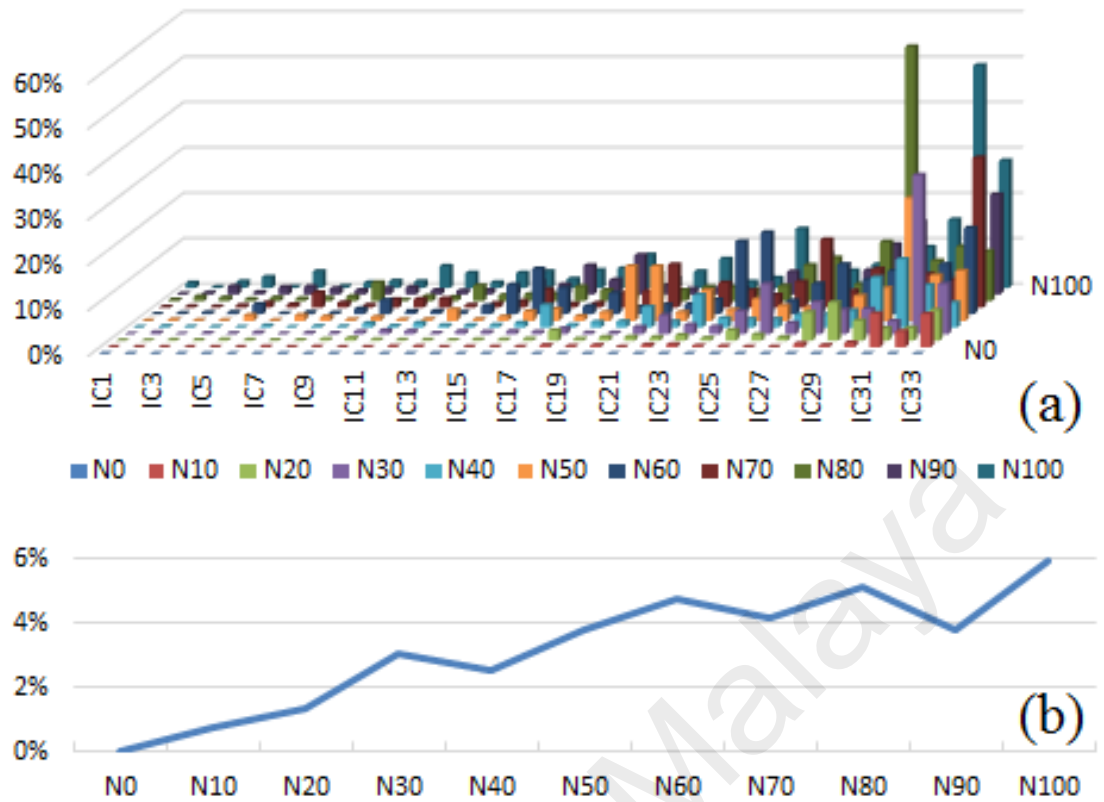


Figure 4.6: (a) Dipole residual variances of all the ICs of all the EEG data sets. (b) Changes of average residual variances with noise levels.

4.4.4 Findings of Noise-Effect Analysis

In parallel with 2D topographic maps, 3D topographic maps can also be used for IC selection. Although 3D maps are more realistic than 2D maps, 2D maps were preferred for this analysis because of their relevance with the spherical head models that is used for EEG generation. This part of this study analyzed the most commonly used features of ICs and the results indicated the significant effects of coherent background noise on these features and with high level of noise these features could not help to identify the ictal components. Therefore, searching for more features or deriving a new effective feature of decomposed ICs for better identification of the ictal components from highly noisy datasets was essential.

4.5 Validation Results of the RIDICS Technique

The RIDICS technique was validated using both simulated and real ictal EEG data. Those validation results are presented in next two subsections respectively.

4.5.1 Validation of RIDICS Technique Using Simulated Data

Figure 4.7 illustrates the Euclidean distance between D and every D_{BIC} that was modeled from each BIC obtained by three different techniques (RIDICS, PSDICS and TFRICS). It indicates that for precise estimation of dipole sources the RIDICS technique performs better than the other two techniques. Shorter distance represents better identification of BIC and consequently better estimation of dipole source. Figure 4.7 shows that the dipoles, estimated by using the RIDICS technique, had shorter distances for both low noise and high noise datasets. Among 50 datasets (E_1 to E_{50}), the RIDICS technique estimated the closest dipole source for 28 datasets. Other two techniques performed well for low noise datasets but could not perform well

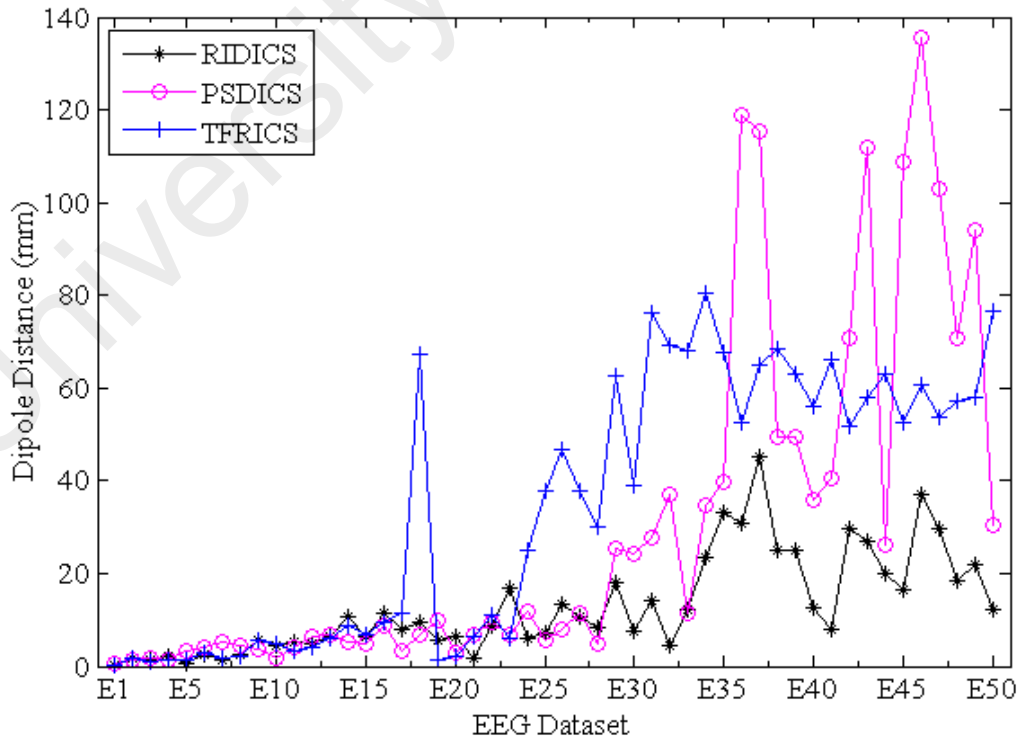


Figure 4.7: Euclidean distance between the original current dipole location D and the estimated current dipole location D_{BIC} , modeled from each BIC.

with higher levels of noises. The PSDICS and the TFRICS techniques estimated the nearest dipole source for 13 and 9 datasets respectively. The estimated average dipole distances were 12.86 mm (minimum 0.29 mm, maximum 45.08 mm), 30.26 mm (minimum 0.39 mm, maximum 135.69 mm), and 34.21 mm (minimum 0.27 mm, maximum 80.41 mm) for the RIDICS, PSDICS and TFRICS techniques respectively. The actual dipole distances, used for producing the graph of Figure 4.7, were listed as a table in Appendix A. The MATLAB codes that were used for implementing the RIDICS, PSDICS, and TFRICS techniques for analyzing simulated ictal EEG data were included in Appendix B, Appendix C, and Appendix D respectively.

Figure 4.8 illustrates the similarities between the original noiseless EEG dataset E and each of the BIC projected datasets (E_{BIC1} , E_{BIC2} , ... and E_{BIC50}) that were obtained

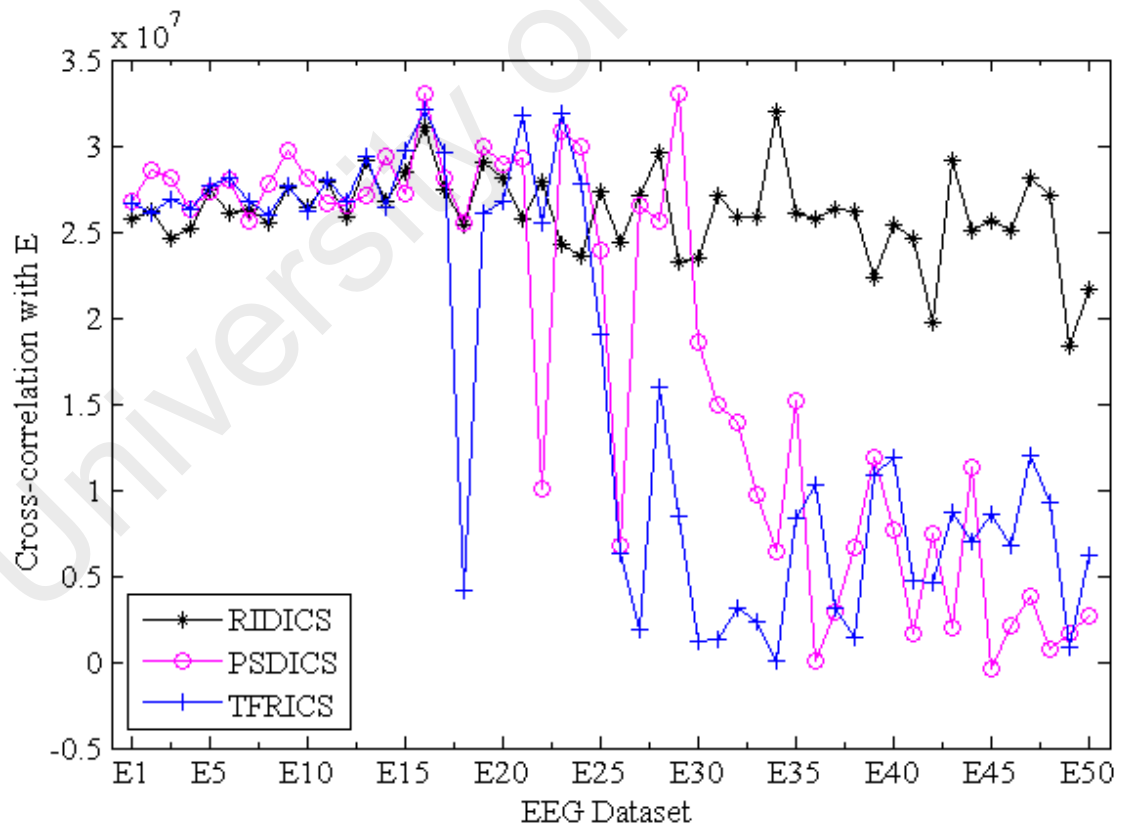


Figure 4.8: Zero-lag cross-correlation values that were estimated between noiseless dataset E and each back-projected dataset E_{BIC} regenerated from the BIC of each simulated ictal EEG dataset.

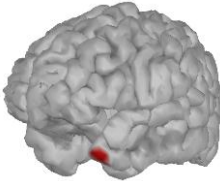
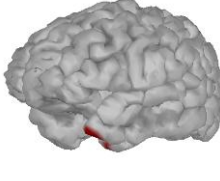
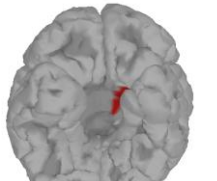
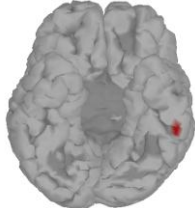
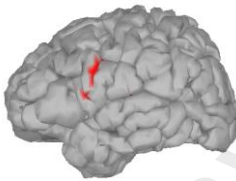
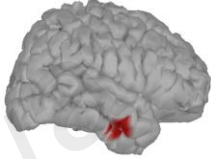

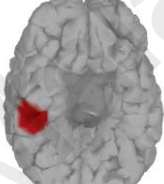
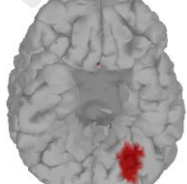
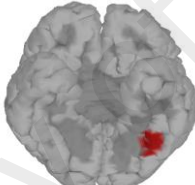
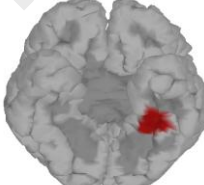
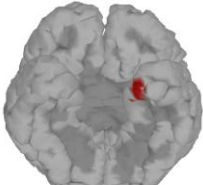
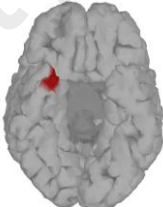
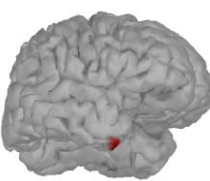
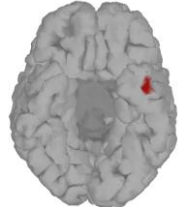
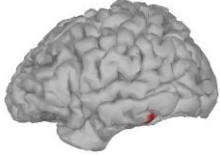
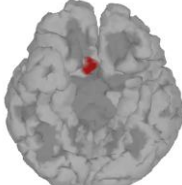
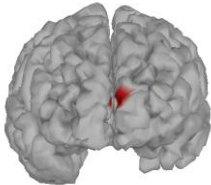
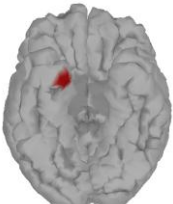
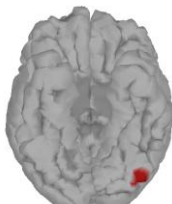
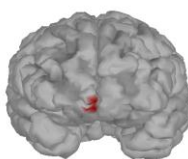

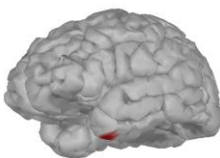
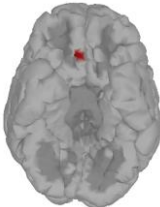
from E_1 , E_2 ... and E_{50} respectively. Cross-correlation value was considered as the similarity measuring metric. Higher cross-correlation value was considered as higher similarity and higher similarity between E and E_{BIC_n} indicated lower noise content in E_n (where $n = 1, 2, \dots 50$). Source estimation from such noise-reduced EEG was expected to give better source localization and the estimated dipole distances (Figure 4.7) supported that expectation. Higher cross correlation value also represented better identification of the corresponding BICs. According to Figure 4.8 the RIDICS technique produced highly correlated back projected EEGs for both low noise and high noise datasets, whereas the PSDICS and TFRICS techniques fail for the highly noisy datasets. In case of the RIDICS technique, 26 datasets produced the highest cross-correlation values for the back projected EEGs, whereas the numbers of such datasets were 14 and 10 for the PSDICS and TFRICS techniques respectively. Moreover the cross-correlation values were more stable for the RIDICS technique with respect to the other two techniques. The corresponding cross-correlation values, used for producing the graph of Figure 4.8, were listed in Appendix A.

The validation study showed that the RIDICS technique performed better with both the performance measuring metrics and with both low-noise and high-noise datasets. Although the other two techniques (PSDICS and TFRICS) performed satisfactorily with low-noise datasets, they could not identify the right BICs from data with high level of noise.

4.5.2 Validation of RIDICS Technique Using Real Data

A cortical source was estimated for each of all selected BICs obtained through the RIDICS, PSDICS and TFRICS techniques and for all of the eight subjects. Table 4.5 presents those ESI estimated sources. On the basis of the results listed in Table 4.5, concordance and discordance of the obtained ictal ESI results with the corresponding

Table 4.5: Surgery sites and corresponding epileptic foci estimated by 3 ESI techniques and for 8 patients. Red cortical areas denote ictal EEG source analyzed using various techniques.

No.	Surgery	RIDICS	PSDICS	TFRICS
1	Left middle temporal cortectomy			
2	Left antero-medial temporal lobectomy			
3	Right occipital cortectomy			
4	Left parieto-occipital cortectomy			
5	Right antero-medial temporal lobectomy			
6	Left antero-medial temporal lobectomy			
7	Right anterior temporal lobectomy			
8	Left selective amygdalo-hippocampectomy			

surgery sites are summarized in Table 4.6. Those results showed that the estimated results for the RIDICS technique were concordant for 7 out of 8 patients (concordance rate 87.50%). Only for the patient 4 the estimated cortical source was in the temporo-occipital region instead of the parieto-occipital region. Although this result was partially concordant, it was not considered as concordant while calculating the concordance rate. The other two techniques, PSDICS and TFRICS, estimated the concordant results for 3 patients and 1 patient respectively, and their concordance rates were 37.50% and 12.50% respectively. Therefore, among the three ESI techniques, the highest concordance rate was obtained for the RIDICS technique.

Although the RIDICS estimated ictal source for the patient 4 was discordant, that source was lateralized in the same hemisphere as the surgery site. Thus, all the RIDICS-estimated sources were lateralized correctly, whereas two estimations (patient 6 & 7) of the PSDICS technique and four estimations (patient 2, 3, 5, & 8) of the TFRICS technique were not found lateralized.

All the EEG sources of Table 4.5 were estimated from the back projected EEGs that were regenerated from the corresponding BICs. Each BIC was a single IC and each IC was temporally independent and specially fixed. Therefore, any source, estimated from

Table 4.6: Concordance or discordance of ESI results with surgery sites

Patient	RIDICS	PSDICS	TFRICS
1	√	√	√
2	√	X	X
3	√	X	X
4	X	X	X
5	√	√	X
6	√	X	X
7	√	X	X
8	√	√	X

√: Concordant, X: Discordant.

the BIC projected EEG was also temporally independent and specially fixed. Thus, each estimated source remained stable for the total duration of the corresponding BIC projected EEG.

4.5.3 Analysis of Outcomes

Simulation-based validation results (Figure 4.7 and Figure 4.8) showed that the RIDICS technique performed the best with high levels of noises (E_{26} to E_{50}), but with low levels of noises (E_1 to E_{25}) its performance seemed not as good as the other two techniques. Therefore, further investigations were carried out through the visual inspection of the IC time courses and the topographic maps of the BICs for verifying the correctness of the results. Visual inspection results also supported the better source estimation capacity of the RIDICS technique with respect to the PSDICS and the TFRICS techniques.

Figure 4.9 and Figure 4.10 illustrate the IC time-courses, two seconds around the ictal onset, that were obtained by decomposing the E_{23} and E_{41} datasets respectively. Those two datasets were selected purposefully. The first dataset (E_{23}) corresponds to the worst performance of the RIDICS technique, because under low noise condition the RIDICS technique estimated the highest dipole distance while the other two techniques performed better with respect to both dipole distance and cross-correlation values. The other dataset (E_{41}) was chosen because that dataset contained enough amount of noise and the RIDICS technique estimated the shortest dipole-distance and the highest cross-correlation value for that dataset with respect to the other two techniques. Three parts of those figures represented the outcomes of the three techniques. The time-course with magenta color represented the BIC and the topographic map of that BIC was presented on top of the corresponding time-course.

Figure 4.9 shows that the RIDICS technique identified the BIC correctly for the E_{23}

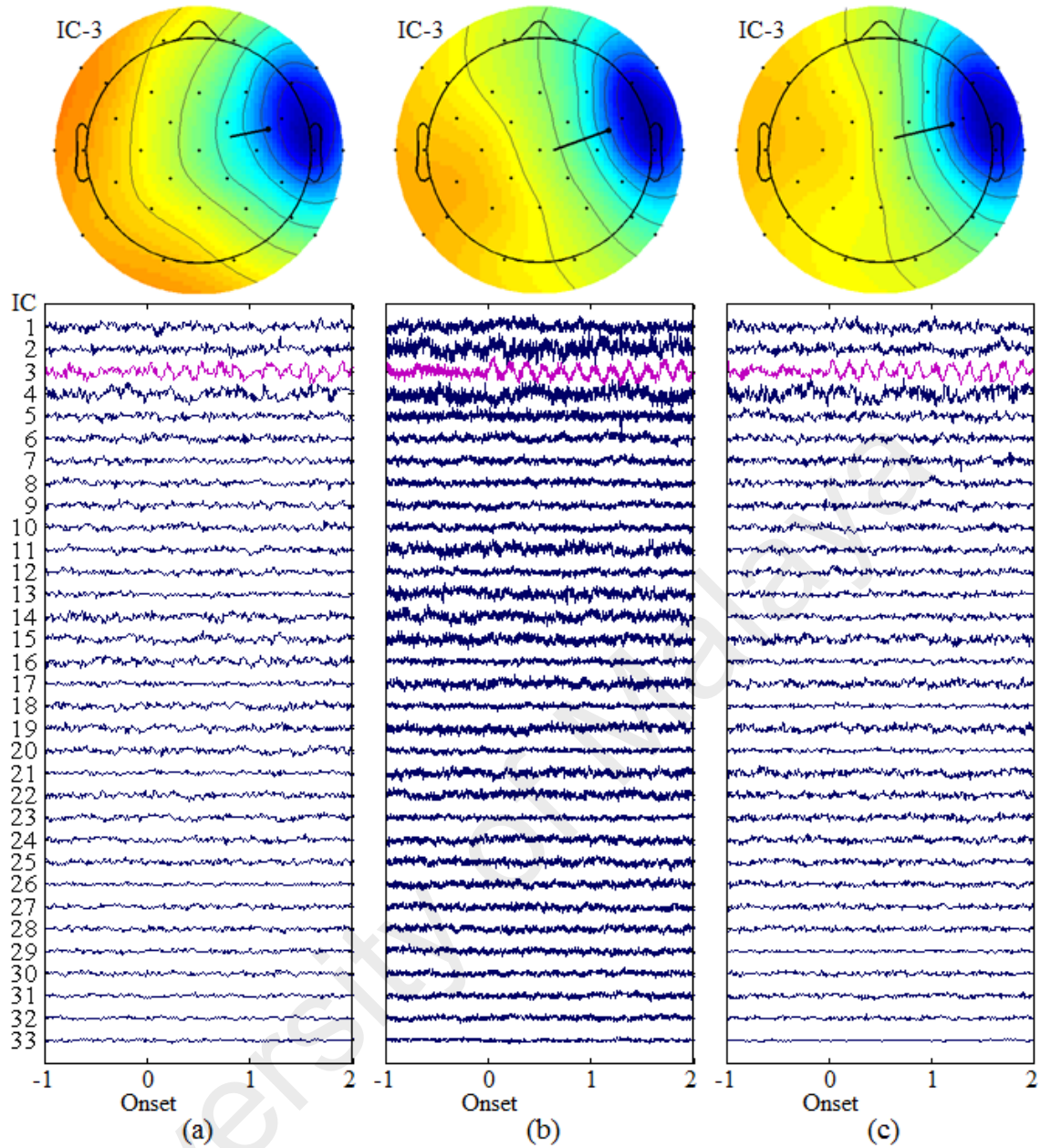


Figure 4.9: Independent Component time-courses of E_{23} dataset and the topographic maps of the BICs (highlighted with Magenta) obtained from (a) the RIDICS technique, (b) the PSDICS technique, and (c) the TFRICS technique.

dataset, but the dipole estimation was not as accurate as the other two techniques. The reason behind the less accurate estimation of the RIDICS technique was that the decomposed ICs, used for the dipole estimation, were not very accurate. The ICA-decompositions were performed by the Infomax ICA algorithm. Figure 4.9 shows that the ICA algorithm produced three different sets of ICs for three different techniques (RIDICS, PSDICS, and TFRICS) and from the same EEG dataset (E_{23}). Since the

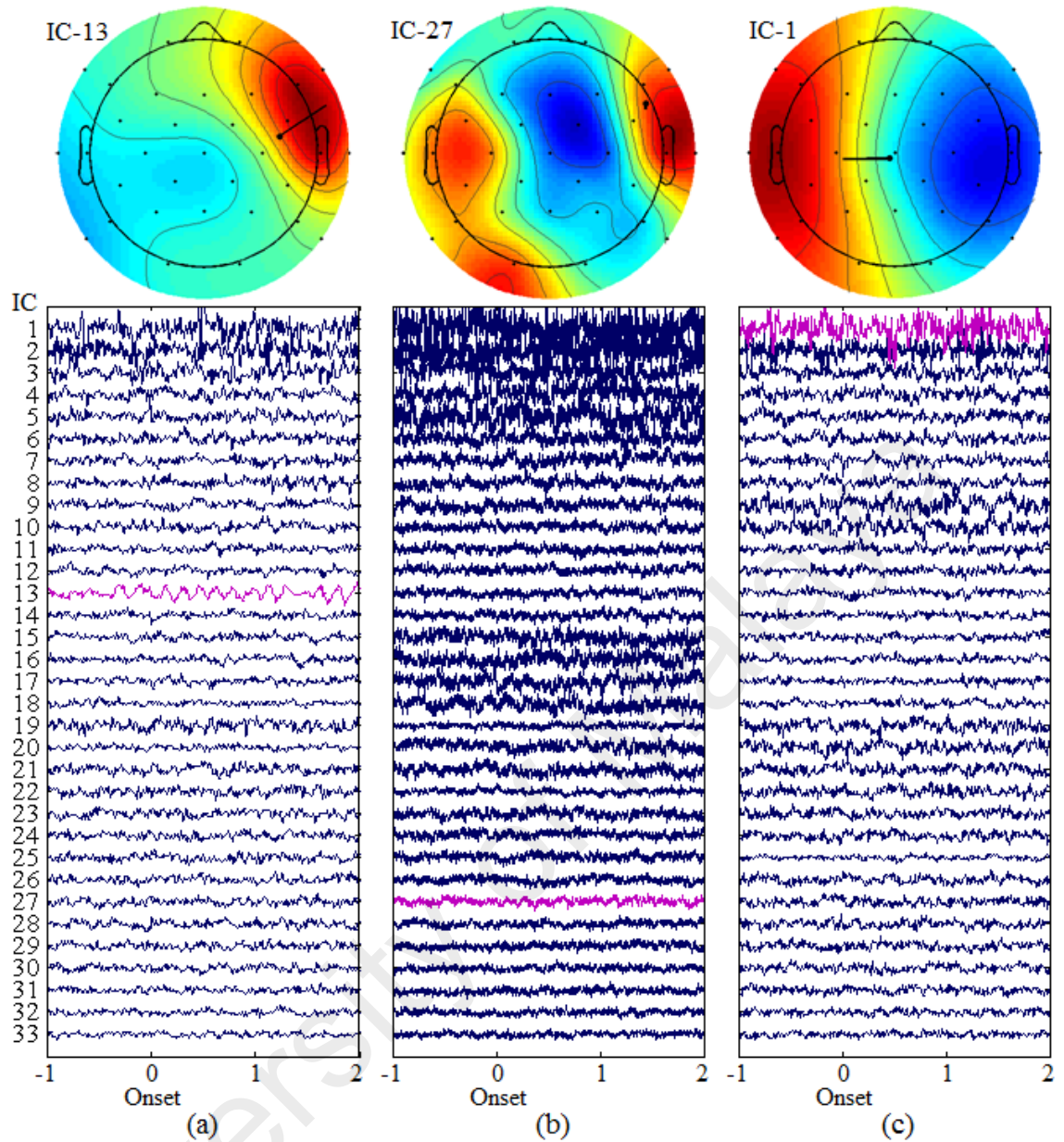


Figure 4.10: Independent Component time-courses of E_{41} dataset and the topographic maps of the BICs (highlighted with Magenta) obtained from (a) the RIDICS technique, (b) the PSDICS technique, and (c) the TFRICS technique.

RIDICS technique identifies the correct BIC for less accurate decomposition, it has the potential to identify the correct BIC for more accurate decomposition as well. Therefore for low noise datasets, proper dipole estimation depends on proper ICA-decomposition.

Figure 4.10 illustrates that the RIDICS technique identified the BIC correctly for the high-noise dataset E_{41} and the topographic map also supports the correctness of the BIC selection. Ictal rhythm is clearly visible in the RIDICS selected BIC, but the rhythm is

not clear in the PDSICS and TFRICS selected BICs. Therefore it is difficult to verify the correctness of the PDSICS and the TFRICS selected BICs. It was also difficult to make any positive decision about the PSDICS and TFRICS results from the topographic maps. The time-courses of Figure 4.10a were obtained after four recursion cycles of the RIDICS technique and in every cycle the amount of noise was reduced. Therefore after four cycles the ictal rhythm became clear in the RIDICS selected BIC. On the contrary, the other two techniques selected the BICs from the original decomposed ICs that contained large amount of noise and as a result the estimated sources from those BICs were less accurate. Therefore, this analysis provided a strong justification for the better performance of the RIDICS technique with the high levels of noises in the datasets.

The time-courses of Figure 4.9 highlighted an important problem, the stochastic behavior, of the ICA-decomposition algorithm. It means that multiple runs of the ICA-decomposition algorithm on the same dataset can produce slightly different results (Himberg, Hyvärinen, & Esposito, 2004; Soldati, Calhoun, Bruzzone, & Jovicich, 2013). The order of the components, their time-courses and their topographic maps may vary from run to run. Therefore, better ICA-decomposition results have an important role on the better estimation of the EEG source.

While producing the results of Figure 4.7 and Figure 4.8, different ICA-decomposition results were used for the three different techniques, because those techniques demanded different ranges of bandpass filtering before decomposing the EEG datasets. The RIDICS and the TFRICS techniques required 1-45Hz and 1-70Hz bandpass filtering respectively, while the PSDICS did not need any filtering before ICA-decomposition. In order to compare the performances of the three techniques for implementing on the same set of decomposed ICs, filtering before ICA-decomposition was avoided. Modified MATLAB code was implemented and similar experimental res-

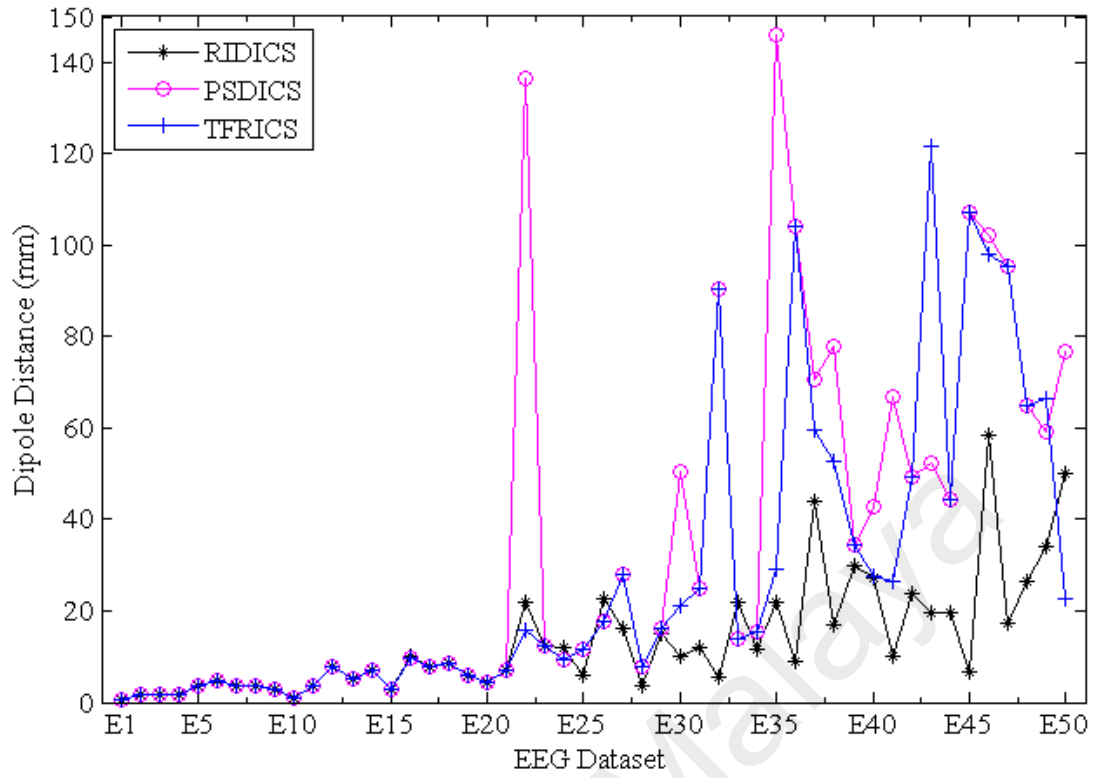


Figure 4.11: Euclidean distance between the locations of D and D_{BIC} for the modified implementation of RIDICS, PSDICS and TFRICS techniques.

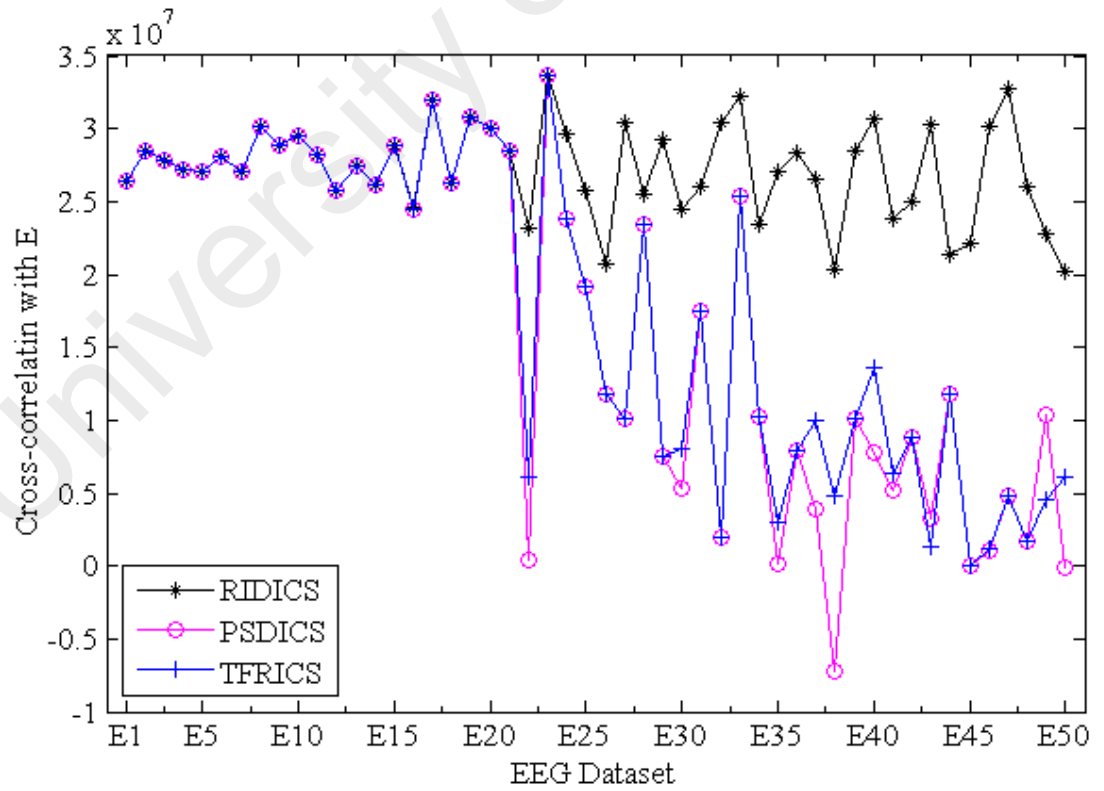


Figure 4.12: Zero-lag cross-correlation values that were estimated between E and E_{BIC} for the modified implementation of RIDICS, PSDICS and TFRICS techniques.

ults as shown in Figure 4.7 and Figure 4.8 were computed. Figure 4.11 and Figure 4.12 illustrate those simulation results. These figures show that all of the three techniques produce same results for most of the low-noise datasets (E_1 to E_{21}). Other datasets reacted almost similar to the experiment done for Figure 4.7 and Figure 4.8. This analysis showed that, despite the stochastic behavior of the ICA-decomposition algorithm, the RIDICS technique performed the best with respect to the PSDICS and the TFRICS techniques.

Another important issue for the RIDICS technique was its execution time. ICA-decomposition itself is a time consuming process, therefore one may assume that the recursive ICA-decomposition may consume unacceptable amount of time. In order to verify the claim, the CPU execution time was recorded for every ICA-decomposition in a single run of the RIDICS technique over 50 sets of simulated ictal EEG data. Those recorded times were presented in Figure 4.13 and it shows that the claim is not true. The average time required for each decomposition phase was 108.92 seconds while the average number of recursion-cycle required for analyzing each dataset was 7.36.

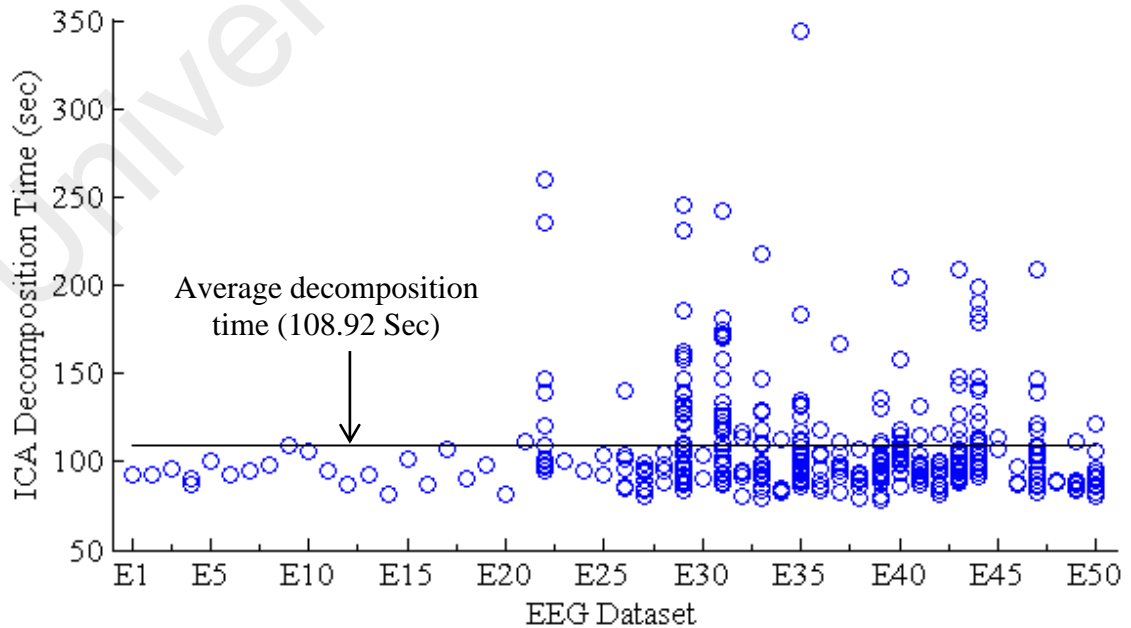


Figure 4.13: Execution time required for every ICA-decomposition.

Therefore, the average time required for the RIDICS analysis of each dataset was 801.65 seconds (i.e. 13.36 minutes), which was quite acceptable with respect to the other diagnostic modalities (e.g. SPECT). The worst case executed 33 recursion cycles and required 4067.11 seconds (67.79 min) and that was also within the acceptable limit. All those time computations as well as all other simulations for this study were performed in a laptop computer with Intel Core i7-4700MQ processor, 32GB DDR3L RAM, and Windows 8.1 operating system.

The RIDICS technique can be used for both low density and high density EEG datasets. Since standard medical EEG systems usually low density type, ESI technique that is customized for low resolution EEG will become more useful and attractive to the clinicians. Success of RIDICS depends on reliable ICA decomposition. Minimum number of data points, required for reliable ICA decomposition, is linearly proportional to the square of the number of electrodes. Therefore, RIDICS requires less data points for low density EEG with respect to high density EEG. Since, the duration of seizure is usually small, it may become difficult to find enough data points from high density EEG. On the contrary, excess data points can be found from low density EEG for better ICA decomposition. Thus, RIDICS may perform better for low density EEG.

4.6 Summary

In this chapter the results of the major development steps, discussed in Section 3.2, of the RIDICS technique were presented. First of all, five free software tools, for realistic head model generation from the MRI scans, were compared and an appropriate tool was selected for the RIDICS technique. The name of the selected tool was BrainSuite. It was selected due to its capacity to generate reliable and realistic head models with higher number of head layers and with minimum user-involvements. Moreover the compatibility of its output file format with the Brainstorm software tool,

used for forward solution and inverse solution, was considered for selecting the BrainSuite software.

Next, a non-ICA based ictal ESI technique was implemented with the help of those two software tools (BrainSuite and Brainstorm) and the clinical utility of the ictal ESI technique with those software tools was validated by analyzing real patients' data. Moreover, three different inverse models were used for EEG source estimation and their results were compared for selecting the best one for the RIDICS technique. The ictal ESI results and their corresponding SPECT results were presented in Table 4.3 and those results were summarized in Table 4.4. The ictal ESI results were found fully lateralized and highly concordant with the corresponding SPECT results. Such good findings supported the clinical usefulness of ictal ESI with the use of free software tools. Those results also showed that the sLORETA inverse model performed better than the other two inverse models. Therefore, sLORETA was chosen for the RIDICS technique.

After that, the effects of noise on three common features of decomposed ICs were analyzed, because the RIDICS technique was supposed to use one of those features for ictal component selection. The analysis outcomes were presented in section 4.4. Those results showed that the topographic map and the activity power spectra needed visual inspection for ictal component selection and the residual variance had no direct relation with the ictal components. Therefore, a new quantitative feature of decomposed ICs was essential for the RIDICS technique.

Finally, a new quantitative feature of decomposed ICs was derived and the RIDICS technique was developed based on that new feature. Validation of the proposed ESI technique, i.e. the RIDICS technique, was carried out by using both simulated and real ictal EEG data. Validation results, using the simulated EEG datasets, were presented in

Figure 4.7 and Figure 4.8. Those results showed the significantly higher performance of the RIDICS technique with respect to the PSDICS and TFRICS techniques. Validation results, using the real data of eight patients, were tabulated in Table 4.5 and were summarized in Table 4.6. The RIDICS results, as well as the PSDICS and TFRICS results, were verified against the corresponding site of successful surgery. Those results showed that the RIDICS results were fully lateralized and highly concordant (concordance rate 87.50%) with the surgery sites. Correctness of those results and the practicality of the RIDICS technique were supported with further analysis. Although RIDICS is a recursive technique, the time analysis showed that the average time required for producing the RIDICS result from a single set of data was not very high compared to other diagnostic modalities.

CHAPTER 5: CONCLUSION AND FUTURE WORK

5.1 Conclusion

The development of a new ICA-based ictal ESI technique, namely the RIDICS technique, has been achieved for epileptogenic focus estimation from ictal EEG. It uses recursive ICA decomposition of ictal EEG and eliminates unwanted component(s) in every recursion cycle. Such elimination of noise helped in better identification of BIC that eventually used to estimate the epileptogenic focus more accurately. Free software tools are used to the implementation of the RIDICS technique mainly for subject specific realistic head model generation, forward solution and inverse solution. Since ictal ESI was comparatively a new computational technique for source estimation, implementation tools were not commercial tools, and various inverse models were available, clinical validations of the existing tools and techniques were essential before implementing the RIDICS technique.

A non-ICA based ESI technique is therefore implemented with free software tools and 3 different linear distributed inverse models and the clinical usefulness of these implementations for epileptic focus localization are examined. Both ictal and interictal ESI are performed on real ictal EEG data and patient-specific realistic head models of 8 selected patients. Lateralization and concordance between ESI-estimated foci and SPECT foci are assessed for the performance evaluation. The results show that the ictal ESI is able to estimate epileptogenic foci more concordantly than the interictal ESI. Moreover, ictal ESI results and ictal SPECT results are found fully lateralized and highly concordant with all 3 different inverse models, and among those inverse models highest number of concordant results are obtained from sLORETA. Therefore, this part of the study strongly justifies the clinical usefulness of ictal ESI with such implementations and also defends the use of free software tools and sLORETA inverse model in the implementation of the RIDICS technique.

In addition to those free software tools and sLORETA inverse model, the RIDICS technique uses a unique quantitative feature of ictal EEG decomposition for selecting the most significant ictal component (i.e. BIC). The epileptogenic focus is estimated from the back projected EEG of that BIC. Therefore, the result remains stable for the total EEG-duration, which is much better than the 10-138ms stable results (Table 4.3) of the non-ICA based ictal ESI technique. The RIDICS technique is implemented on both simulated and real ictal EEG data, and the results are compared with the results of two other ICA-based ictal ESI techniques (PSDICS and TFRICS). Implementation results with simulated EEG are validated with respect to a known dipole location whereas the real-data-analysis results are validated with respect to the known locations of the successful cortical resections. Results are presented in Figure 4.7, Figure 4.8, Table 4.5 and Table 4.6 and those results show the better performance of the RIDICS technique over others. In case of simulated-EEG analysis the dipole estimation error (average distance between the estimated dipole location and the actual dipole location) for the RIDICS technique is less than half of that error for the other two techniques. In case real-data analysis the RIDICS technique estimates fully lateralized and highly concordant results.

In conclusion, a new ICA-based ictal ESI technique, namely the RIDICS technique that is more automatic and less attention-depleting with respect to the existing ESI techniques has been developed. The use of this technique as well as a non-ICA based ictal ESI technique are shown to be feasible in a conventional clinical setup. Moreover, this technique is able to estimate epileptogenic foci more concordantly than two other ICA-based techniques (automated version). Therefore, this study could form a basis for future studies that evaluate the value of the RIDICS technique as a cost-effective substitute for existing costly diagnostic modalities (such as ictal SPECT) for presurgical evaluation of focal epilepsy.

5.2 Summary of Contributions

The following are the major contributions of this work:

- i) A unique quantitative feature of decomposed rhythmic ictal EEG has been formulated for identifying the most significant ictal component. This feature can also be used for other applications where the vital rhythmic component needs to be selected from a mixture of rhythmic activities.
- ii) A new ICA-based ictal ESI technique has been developed for its potential application to presurgical evaluation of refractory focal epilepsy. The originality of this technique consists of using the recursive ICA decomposition approach and a unique quantitative feature for ictal component selection.
- iii) The clinical usefulness of a non-ICA based ictal ESI technique and the RIDICS technique for the epileptogenic focus localization is examined with conventional clinical setup. No special clinical arrangement, such as high resolution EEG, is used for data acquisition.

5.3 Limitations

Although this study developed, implemented and evaluated the RIDICS technique successfully, it has the following limitations:

- i) The RIDICS technique is designed for evaluating the rhythmic ictal activities in the brain signals of focal epilepsy patients, but focal epilepsy may produce irregular ictal spikes as well. Since the RIDICS technique uses the ictal rhythm frequencies for selecting the ictal component, this technique may not work for evaluating the ictal spikes.

- ii) Patients with clear ictal SPECTs and seizure free clinical surgery are included in real-data based validations. Since, the number of such patients is not high, the real-data based validations of this study has small sample size.
- iii) Success of the RIDICS technique is dependent on the success of the ICA decomposition algorithm. If the decomposition algorithm fails (i.e. cannot converge), then the RIDICS technique will also fail.

In this study the sample size was limited to 12 (8 in the first experiment + 8 in the second experiment – 4 common in both experiments) and such small sample size (≤ 12) is very common in ictal ESI studies (Beniczky et al., 2006; Ding et al., 2007; Holmes et al., 2010; Jung et al., 2009; Koessler et al., 2010; Kovac et al., 2014; Lantz et al., 1999; Lu, Yang, Worrell, Brinkmann, et al., 2012; Lu, Yang, Worrell, & He, 2012; Merlet & Gotman, 2001; Yang et al., 2011). The main reasons are discussed below. Ictal ESI studies used both EEG and MRI of a subject for EEG-source estimation and also used iEEG (Assaf & Ebersole, 1997; Boon et al., 2002; Holmes et al., 2010; Lu, Yang, Worrell, Brinkmann, et al., 2012; Yang et al., 2011), site of successful surgery (Assaf & Ebersole, 1999; Boon et al., 2002; Holmes et al., 2010; Jung et al., 2009; Lu, Yang, Worrell, Brinkmann, et al., 2012; Lu, Yang, Worrell, & He, 2012; Yang et al., 2011), ictal SPECT (Beniczky et al., 2006; Ding et al., 2007; Lantz et al., 1999), MRI lesion (Ding et al., 2007; Lantz et al., 1999), etc., of the same subject as the gold standard for evaluating the correctness of the estimated sources. This study used ictal SPECTs and sites of successful surgery as the gold standards for the realizations of objective 1 and objective 3 respectively. Since all patients do not go for ictal SPECT and success rate of epilepsy surgery is low, small sample size is justified.

5.4 Recommendation for Future Work

In future more in-depth analysis of various aspects of this study can be carried out. This paper would lay the foundation of such future work. Some possible future works are listed below:

- i) Validation of the RIDICS technique using real-data of larger patient population.
- ii) Modification of the RIDICS technique for estimating epileptogenic focus not only from the ictal rhythms but also from the ictal spikes.
- iii) Investigate the effects of the discontinuities occur in the RIDICS technique due to the concatenation of multiple selected epochs for preparing the input data set.
- iv) Optimization of the stopping criteria of the RIDICS algorithm for further improvement of its performance.

REFERENCES

- Acar, Z. A., & Makeig, S. (2010). Neuroelectromagnetic forward head modeling toolbox. *Journal of neuroscience methods*, 190(2), 258-270.
- Adrian, E. D., & Matthews, B. H. C. (1934). The Berger rhythm: potential changes from the occipital lobes in man. *Brain*, 57(4), 355-385.
- Ary, J. P., Klein, S. A., & Fender, D. H. (1981). Location of sources of evoked scalp potentials: corrections for skull and scalp thicknesses. *IEEE Trans Biomed Eng*, 28(6), 447-452.
- Ashburner, J., & Friston, K. J. (2005). Unified segmentation. *Neuroimage*, 26(3), 839-851.
- Assaf, B. A., & Ebersole, J. S. (1997). Continuous source imaging of scalp ictal rhythms in temporal lobe epilepsy. *Epilepsia*, 38(10), 1114-1123.
- Assaf, B. A., & Ebersole, J. S. (1999). Visual and quantitative ictal EEG predictors of outcome after temporal lobectomy. *Epilepsia*, 40(1), 52-61.
- Babiloni, C., Cassetta, E., Binetti, G., Tombini, M., Del Percio, C., Ferreri, F., . . . Nobili, F. (2007). Resting EEG sources correlate with attentional span in mild cognitive impairment and Alzheimer's disease. *European Journal of Neuroscience*, 25(12), 3742-3757.
- Babiloni, C., Del Percio, C., Lizio, R., Marzano, N., Infarinato, F., Soricelli, A., . . . Tedeschi, G. (2014). Cortical sources of resting state electroencephalographic alpha rhythms deteriorate across time in subjects with amnesic mild cognitive impairment. *Neurobiology of aging*, 35(1), 130-142.
- Becker, H. (2014). *Denoising, separation and localization of EEG sources in the context of epilepsy*. (Doctoral dissertation), Université Nice Sophia Antipolis.
- Bell, A. J., & Sejnowski, T. J. (1995). An information-maximization approach to blind separation and blind deconvolution. *Neural computation*, 7(6), 1129-1159.
- Beniczky, S., Oturai, P. S., Alving, J., Sabers, A., Herning, M., & Fabricius, M. (2006). Source analysis of epileptic discharges using multiple signal classification analysis. *Neuroreport*, 17(12), 1283-1287.
- Berg, P., & Scherg, M. (1991). Dipole modelling of eye activity and its application to the removal of eye artefacts from the EEG and MEG. *Clinical Physics and Physiological Measurement*, 12(A), 49.
- Berg, P., & Scherg, M. (1994). A fast method for forward computation of multiple-shell spherical head models. *Electroencephalogr Clin Neurophysiol*, 90(1), 58-64.
- Berger, H. (1929). Über das elektrenkephalogramm des menschen. *European Archives of Psychiatry and Clinical Neuroscience*, 87(1), 527-570.

- Boon, P., D'havé, M., Vanrumste, B., Van Hoey, G., Vonck, K., Van Wallegghem, P., . . . De Reuck, J. (2002). Ictal source localization in presurgical patients with refractory epilepsy. *Journal of Clinical Neurophysiology*, 19(5), 461-468.
- Brodbeck, V., Spinelli, L., Lascano, A. M., Wissmeier, M., Vargas, M. I., Vulliemoz, S., . . . Seeck, M. (2011). Electroencephalographic source imaging: a prospective study of 152 operated epileptic patients. *Brain*, 134(Pt 10), 2887-2897.
- Chatrian, G., Lettich, E., & Nelson, P. (1985). Ten percent electrode system for topographic studies of spontaneous and evoked EEG activities. *American Journal of EEG technology*, 25(2), 83-92.
- Chitoku, S., Otsubo, H., Ichimura, T., Saigusa, T., Ochi, A., Shirasawa, A., . . . Rutka, J. T. (2003). Characteristics of dipoles in clustered individual spikes and averaged spikes. *Brain and Development*, 25(1), 14-21.
- Cointepas, Y., Mangin, J.-F., Garnero, L., Poline, J.-B., & Benali, H. (2001). BrainVISA: software platform for visualization and analysis of multi-modality brain data. *Neuroimage*, 13(6), 98.
- Compston, A. (2009). The Berger rhythm: potential changes from the occipital lobes in man, by E.D. Adrian and B.H.C. Matthews (From the Physiological Laboratory, Cambridge). *Brain* 1934: 57; 355–385. *Brain*, 133(1), 3-6.
- Correa, A. G., Laciár, E., Patiño, H. D., & Valentinuzzi, M. E. (2007). Artifact removal from EEG signals using adaptive filters in cascade. *Journal of Physics: Conference Series*, 90(1), 012081.
- Croft, R. J., & Barry, R. J. (2000). Removal of ocular artifact from the EEG: a review. *Neurophysiologie Clinique/Clinical Neurophysiology*, 30(1), 5-19.
- Cuffin, B. N. (1996). EEG localization accuracy improvements using realistically shaped head models. *IEEE Transactions on Biomedical Engineering*, 43(3), 299-303.
- Dale, A. M., Fischl, B., & Sereno, M. I. (1999). Cortical surface-based analysis: I. Segmentation and surface reconstruction. *Neuroimage*, 9(2), 179-194.
- Dale, A. M., Liu, A. K., Fischl, B. R., Buckner, R. L., Belliveau, J. W., Lewine, J. D., & Halgren, E. (2000). Dynamic statistical parametric mapping: combining fMRI and MEG for high-resolution imaging of cortical activity. *Neuron*, 26(1), 55-67.
- Daly, I., Nicolaou, N., Nasuto, S. J., & Warwick, K. (2013). Automated artifact removal from the electroencephalogram: a comparative study. *Clinical EEG and neuroscience*, 44(4), 291-306.
- Darcey, T., Ary, J., & Fender, D. (1980). Spatio-temporal visually evoked scalp potentials in response to partial-field patterned stimulation. *Electroencephalogr Clin Neurophysiol*, 50(5), 348-355.

- De Munck, J. (1990). The estimation of time varying dipoles on the basis of evoked potentials. *Electroencephalography and Clinical Neurophysiology/Evoked Potentials Section*, 77(2), 156-160.
- de Peralta Menendez, R. G., Andino, S. G., Lantz, G., Michel, C. M., & Landis, T. (2001). Noninvasive localization of electromagnetic epileptic activity. I. Method descriptions and simulations. *Brain topography*, 14(2), 131-137.
- de Peralta Menendez, R. G., Murray, M. M., Michel, C. M., Martuzzi, R., & Andino, S. L. G. (2004). Electrical neuroimaging based on biophysical constraints. *Neuroimage*, 21(2), 527-539.
- De Vos, M., Vergult, A., De Lathauwer, L., De Clercq, W., Van Huffel, S., Dupont, P., . . . Van Paesschen, W. (2007). Canonical decomposition of ictal scalp EEG reliably detects the seizure onset zone. *Neuroimage*, 37(3), 844-854.
- Delorme, A., & Makeig, S. (2004). EEGLAB: an open source toolbox for analysis of single-trial EEG dynamics including independent component analysis. *Journal of neuroscience methods*, 134(1), 9-21.
- Ding, L., Worrell, G. A., Lagerlund, T. D., & He, B. (2007). Ictal source analysis: localization and imaging of causal interactions in humans. *Neuroimage*, 34(2), 575-586.
- Ebersole, J. S., & Hawes-Ebersole, S. (2007). Clinical application of dipole models in the localization of epileptiform activity. *Journal of Clinical Neurophysiology*, 24(2), 120-129.
- Ebersole, J. S., & Pedley, T. A. (Eds.). (2003). *Current practice of clinical electroencephalography*: Lippincott Williams & Wilkins.
- Elliott, S., Painter, J., & Hudson, S. (2009). Living alone and fall risk factors in community-dwelling middle age and older adults. *Journal of community health*, 34(4), 301.
- Engel, J., Jr. (1993). Update on surgical treatment of the epilepsies. Summary of the Second International Palm Desert Conference on the Surgical Treatment of the Epilepsies (1992). *Neurology*, 43(8), 1612-1617.
- Fiederer, L. D., Vorwerk, J., Lucka, F., Dannhauer, M., Yang, S., Dümpelmann, M., . . . Wolters, C. H. (2016). The role of blood vessels in high-resolution volume conductor head modeling of EEG. *Neuroimage*, 128, 193-208.
- Fisch, B. J., & Spehlmann, R. (1999). *Fisch and Spehlmann's EEG primer: basic principles of digital and analog EEG*: Elsevier Health Sciences.
- Fisher, R. S., van Emde Boas, W., Blume, W., Elger, C., Genton, P., Lee, P., & Engel, J., Jr. (2005). Epileptic seizures and epilepsy: definitions proposed by the International League Against Epilepsy (ILAE) and the International Bureau for Epilepsy (IBE). *Epilepsia*, 46(4), 470-472.

- Fitzgibbon, S. P., Powers, D. M., Pope, K. J., & Clark, C. R. (2007). Removal of EEG noise and artifact using blind source separation. *Journal of Clinical Neurophysiology*, 24(3), 232-243.
- Foldvary, N., Klem, G., Hammel, J., Bingaman, W., Najm, I., & Lüders, H. (2001). The localizing value of ictal EEG in focal epilepsy. *Neurology*, 57(11), 2022-2028.
- Frank, E. (1952). Electric Potential Produced by Two Point Current Sources in a Homogeneous Conducting Sphere. *Journal of Applied Physics*, 23(11), 1225-1228.
- Geffroy, D., Rivière, D., Denghien, I., Souedet, N., Laguitton, S., & Cointepas, Y. (2011). *BrainVISA: a complete software platform for neuroimaging*. Paper presented at the Python in neuroscience workshop.
- Gorodnitsky, I. F., George, J. S., & Rao, B. D. (1995). Neuromagnetic source imaging with FOCUSS: a recursive weighted minimum norm algorithm. *Electroencephalogr Clin Neurophysiol*, 95(4), 231-251.
- Gotman, J. (1982). Automatic recognition of epileptic seizures in the EEG. *Electroencephalogr Clin Neurophysiol*, 54(5), 530-540.
- Gramfort, A., Papadopoulos, T., Olivi, E., & Clerc, M. (2010). OpenMEEG: opensource software for quasistatic bioelectromagnetics. *Biomedical engineering online*, 9(1), 45.
- Gramfort, A., Papadopoulos, T., Olivi, E., & Clerc, M. (2011). Forward field computation with OpenMEEG. *Computational intelligence and neuroscience*, 2011.
- Grech, R., Cassar, T., Muscat, J., Camilleri, K. P., Fabri, S. G., Zervakis, M., . . . Vanrumste, B. (2008). Review on solving the inverse problem in EEG source analysis. *Journal of neuroengineering and rehabilitation*, 5(1), 25.
- Groppe, D. M., Makeig, S., & Kutas, M. (2009). Identifying reliable independent components via split-half comparisons. *Neuroimage*, 45(4), 1199-1211.
- Habib, M. A., Ibrahim, F., Mohktar, M. S., Kamaruzzaman, S. B., Rahmat, K., & Lim, K. S. (2016). Ictal EEG source imaging for presurgical evaluation of refractory focal epilepsy. *World neurosurgery*, 88, 576-585.
- Habib, M. A., Ibrahim, F., Mohktar, M. S., Lim, K. S., & Kamaruzzaman, S. B. (2014). A comparison of five free software solutions for generating realistic human head models from magnetic resonance imaging.
- Habib, M. A., Mohktar, M. S., Kamaruzzaman, S. B., Lim, K. S., Pin, T. M., & Ibrahim, F. (2014). Smartphone-based solutions for fall detection and prevention: challenges and open issues. *Sensors*, 14(4), 7181-7208.
- Hallez, H., Vanrumste, B., Grech, R., Muscat, J., De Clercq, W., Vergult, A., . . . Van Huffel, S. (2007). Review on solving the forward problem in EEG source analysis. *Journal of neuroengineering and rehabilitation*, 4(1), 46.

- Hämäläinen, M. S., & Ilmoniemi, R. J. (1994). Interpreting magnetic fields of the brain: minimum norm estimates. *Medical and biological engineering and computing*, 32(1), 35-42.
- Hamalainen, M. S., & Sarvas, J. (1989). Realistic conductivity geometry model of the human head for interpretation of neuromagnetic data. *IEEE Transactions on Biomedical Engineering*, 36(2), 165-171.
- He, B., & Ding, L. (2013). Electrophysiological Mapping and Neuroimaging. In B. He (Ed.), *Neural Engineering* (pp. 499-543). Boston, MA: Springer US.
- He, B., Musha, T., Okamoto, Y., Homma, S., Nakajima, Y., & Sato, T. (1987). Electric dipole tracing in the brain by means of the boundary element method and its accuracy. *IEEE Transactions on Biomedical Engineering*(6), 406-414.
- Helmholtz, H. v. (1853). Ueber einige Gesetze der Vertheilung elektrischer Ströme in körperlichen Leitern mit Anwendung auf die thierisch-elektrischen Versuche. *Annalen der Physik*, 165(6), 211-233.
- Himberg, J., Hyvärinen, A., & Esposito, F. (2004). Validating the independent components of neuroimaging time series via clustering and visualization. *Neuroimage*, 22(3), 1214-1222.
- Holmes, M. D., Brown, M., & Tucker, D. M. (2004). Are “generalized” seizures truly generalized? Evidence of localized mesial frontal and frontopolar discharges in absence. *Epilepsia*, 45(12), 1568-1579.
- Holmes, M. D., Tucker, D. M., Quiring, J. M., Hakimian, S., Miller, J. W., & Ojemann, J. G. (2010). Comparing noninvasive dense array and intracranial electroencephalography for localization of seizures. *Neurosurgery*, 66(2), 354-362.
- Iatsenko, D., McClintock, P. V., & Stefanovska, A. (2015). Nonlinear mode decomposition: A noise-robust, adaptive decomposition method. *Physical Review E*, 92(3), 032916.
- Iriarte, J., Urrestarazu, E., Artieda, J., Valencia, M., LeVan, P., Viteri, C., & Alegre, M. (2006). Independent component analysis in the study of focal seizures. *Journal of Clinical Neurophysiology*, 23(6), 551-558.
- Iriarte, J., Urrestarazu, E., Valencia, M., Alegre, M., Malanda, A., Viteri, C., & Artieda, J. (2003). Independent component analysis as a tool to eliminate artifacts in EEG: a quantitative study. *Journal of Clinical Neurophysiology*, 20(4), 249-257.
- James, C. J., & Hesse, C. W. (2005). Independent component analysis for biomedical signals. *Physiological measurement*, 26(1), R15-R39.
- Jasper, H. H. (1958). The ten twenty electrode system of the international federation. *Electroencephalogr Clin Neurophysiol*, 10, 371-375.

- Jatoi, M. A., Kamel, N., Malik, A. S., Faye, I., & Begum, T. (2014). A survey of methods used for source localization using EEG signals. *Biomedical Signal Processing and Control*, 11, 42-52.
- Jayakar, P., Duchowny, M., Resnick, T. J., & Alvarez, L. A. (1991). Localization of seizure foci: pitfalls and caveats. *Journal of Clinical Neurophysiology*, 8(4), 414-431.
- Jung, K.-Y., Kang, J.-K., Kim, J. H., Im, C.-H., Kim, K. H., & Jung, H.-K. (2009). Spatiotemporospectral characteristics of scalp ictal EEG in mesial temporal lobe epilepsy with hippocampal sclerosis. *Brain research*, 1287, 206-219.
- Jung, T.-P., Makeig, S., Westerfield, M., Townsend, J., Courchesne, E., & Sejnowski, T. J. (2000). Removal of eye activity artifacts from visual event-related potentials in normal and clinical subjects. *Clinical neurophysiology*, 111(10), 1745-1758.
- Jung, T. P., Makeig, S., Humphries, C., Lee, T. W., Mckeown, M. J., Iragui, V., & Sejnowski, T. J. (2000). Removing electroencephalographic artifacts by blind source separation. *Psychophysiology*, 37(2), 163-178.
- Kaiboriboon, K., Lüders, H. O., Hamaneh, M., Turnbull, J., & Lhatoo, S. D. (2012). EEG source imaging in epilepsy—practicalities and pitfalls. *Nature Reviews Neurology*, 8(9), 498-507.
- Kazemi, K., & Noorizadeh, N. (2014). Quantitative comparison of SPM, FSL, and BrainSuite for brain MR Image segmentation. *Journal of Biomedical Physics and Engineering*, 4(1 Mar).
- Khanna, A., Pascual-Leone, A., Michel, C. M., & Farzan, F. (2015). Microstates in resting-state EEG: current status and future directions. *Neuroscience & Biobehavioral Reviews*, 49, 105-113.
- Klauschen, F., Goldman, A., Barra, V., Meyer-Lindenberg, A., & Lundervold, A. (2009). Evaluation of automated brain MR image segmentation and volumetry methods. *Human brain mapping*, 30(4), 1310-1327.
- Klem, G. H., Lüders, H. O., Jasper, H., & Elger, C. (1999). The ten-twenty electrode system of the International Federation. *Electroencephalogr Clin Neurophysiol*, 52(3), 3-6.
- Kobayashi, K., Akiyama, T., Nakahori, T., Yoshinaga, H., & Gotman, J. (2002). Systematic source estimation of spikes by a combination of independent component analysis and RAP-MUSIC: I: Principles and simulation study. *Clinical neurophysiology*, 113(5), 713-724.
- Koessler, L., Benar, C., Maillard, L., Badier, J.-M., Vignal, J. P., Bartolomei, F., . . . Gavaret, M. (2010). Source localization of ictal epileptic activity investigated by high resolution EEG and validated by SEEG. *Neuroimage*, 51(2), 642-653.
- Koles, Z. J. (1998). Trends in EEG source localization. *Electroencephalogr Clin Neurophysiol*, 106(2), 127-137.

- Koles, Z. J., Lind, J., & Soong, A. (1995). Spatio-temporal decomposition of the EEG: a general approach to the isolation and localization of sources. *Electroencephalogr Clin Neurophysiol*, 95(4), 219-230.
- Kovac, S., Chaudhary, U. J., Rodionov, R., Mantoan, L., Scott, C. A., Lemieux, L., . . . Diehl, B. (2014). Ictal EEG source imaging in frontal lobe epilepsy leads to improved lateralization compared with visual analysis. *Journal of Clinical Neurophysiology*, 31(1), 10-20.
- Krishnaveni, V., Jayaraman, S., Anitha, L., & Ramadoss, K. (2006). Removal of ocular artifacts from EEG using adaptive thresholding of wavelet coefficients. *Journal of neural engineering*, 3(4), 338.
- Lantz, G., Grave de Peralta, R., Spinelli, L., Seeck, M., & Michel, C. M. (2003). Epileptic source localization with high density EEG: how many electrodes are needed? *Clin Neurophysiol*, 114(1), 63-69.
- Lantz, G., Michel, C., Seeck, M., Blanke, O., Landis, T., & Rosén, I. (1999). Frequency domain EEG source localization of ictal epileptiform activity in patients with partial complex epilepsy of temporal lobe origin. *Clinical neurophysiology*, 110(1), 176-184.
- Lantz, G., Spinelli, L., Seeck, M., de Peralta Menendez, R. G., Sottas, C. C., & Michel, C. M. (2003). Propagation of interictal epileptiform activity can lead to erroneous source localizations: a 128-channel EEG mapping study. *Journal of Clinical Neurophysiology*, 20(5), 311-319.
- Lawn, N. D., Bamlet, W., Radhakrishnan, K., O'Brien, P., & So, E. (2004). Injuries due to seizures in persons with epilepsy A population-based study. *Neurology*, 63(9), 1565-1570.
- Leal, A. J., Dias, A. I., & Vieira, J. P. (2006). Analysis of the EEG dynamics of epileptic activity in gelastic seizures using decomposition in independent components. *Clinical neurophysiology*, 117(7), 1595-1601.
- Lemieux, L., McBride, A., & Hand, J. W. (1996). Calculation of electrical potentials on the surface of a realistic head model by finite differences. *Physics in Medicine and Biology*, 41(7), 1079.
- Lin, F.-H., Witzel, T., Ahlfors, S. P., Stufflebeam, S. M., Belliveau, J. W., & Hämäläinen, M. S. (2006). Assessing and improving the spatial accuracy in MEG source localization by depth-weighted minimum-norm estimates. *Neuroimage*, 31(1), 160-171.
- Lu, Y., Yang, L., Worrell, G. A., Brinkmann, B., Nelson, C., & He, B. (2012). Dynamic imaging of seizure activity in pediatric epilepsy patients. *Clinical neurophysiology*, 123(11), 2122-2129.
- Lu, Y., Yang, L., Worrell, G. A., & He, B. (2012). Seizure source imaging by means of FINE spatio-temporal dipole localization and directed transfer function in partial epilepsy patients. *Clinical neurophysiology*, 123(7), 1275-1283.

- Luders, H. O., Najm, I., Nair, D., Widdess-Walsh, P., & Bingman, W. (2006). The epileptogenic zone: general principles. *Epileptic Disord*, 8 Suppl 2, S1-9.
- MacKinnon, C. D., Verrier, M. C., & Tatton, W. G. (2000). Motor cortical potentials precede long-latency EMG activity evoked by imposed displacements of the human wrist. *Experimental brain research*, 131(4), 477-490.
- McMenamin, B. W., Shackman, A. J., Maxwell, J. S., Bachhuber, D. R., Koppenhaver, A. M., Greischar, L. L., & Davidson, R. J. (2010). Validation of ICA-based myogenic artifact correction for scalp and source-localized EEG. *Neuroimage*, 49(3), 2416-2432.
- Meijs, J., Bosch, F., Peters, M., & Da Silva, F. L. (1987). On the magnetic field distribution generated by a dipolar current source situated in a realistically shaped compartment model of the head. *Electroencephalogr Clin Neurophysiol*, 66(3), 286-298.
- Menninghaus, E., Lutkenhoner, B., & Gonzalez, S. L. (1994). Localization of a dipolar source in a skull phantom: realistic versus spherical model. *IEEE Transactions on Biomedical Engineering*, 41(10), 986-989.
- Merlet, I., & Gotman, J. (2001). Dipole modeling of scalp electroencephalogram epileptic discharges: correlation with intracerebral fields. *Clinical neurophysiology*, 112(3), 414-430.
- Michel, C. M., & Murray, M. M. (2012). Towards the utilization of EEG as a brain imaging tool. *Neuroimage*, 61(2), 371-385.
- Michel, C. M., Murray, M. M., Lantz, G., Gonzalez, S., Spinelli, L., & de Peralta, R. G. (2004). EEG source imaging. *Clinical neurophysiology*, 115(10), 2195-2222.
- Miller, C. E., & Henriquez, C. S. (1990). Finite element analysis of bioelectric phenomena. *Critical reviews in biomedical engineering*, 18(3), 207-233.
- Moshe, S. L., Perucca, E., Ryvlin, P., & Tomson, T. (2015). Epilepsy: new advances. *Lancet*, 385(9971), 884-898.
- Mosher, J. C., Baillet, S., & Leahy, R. M. (1999). EEG source localization and imaging using multiple signal classification approaches. *J Clin Neurophysiol*, 16(3), 225-238.
- Mosher, J. C., & Leahy, R. M. (1998). Recursive MUSIC: a framework for EEG and MEG source localization. *IEEE Transactions on Biomedical Engineering*, 45(11), 1342-1354.
- Mosher, J. C., Lewis, P. S., & Leahy, R. M. (1992). Multiple dipole modeling and localization from spatio-temporal MEG data. *IEEE Transactions on Biomedical Engineering*, 39(6), 541-557.
- Nam, H., Yim, T. G., Han, S. K., Oh, J. B., & Lee, S. K. (2002). Independent component analysis of ictal EEG in medial temporal lobe epilepsy. *Epilepsia*, 43(2), 160-164.

- Ngugi, A. K., Bottomley, C., Kleinschmidt, I., Sander, J. W., & Newton, C. R. (2010). Estimation of the burden of active and life-time epilepsy: a meta-analytic approach. *Epilepsia*, 51(5), 883-890.
- Nunez, P. L., & Srinivasan, R. (2006). *Electric fields of the brain: the neurophysics of EEG*: Oxford University Press, USA.
- O'Brien, T. J., Brinkmann, B. H., Mullan, B. P., So, E. L., Hauser, M. F., O'Connor, M. K., . . . Jack, C. R. (1999). Comparative study of 99mTc-ECD and 99mTc-HMPAO for peri-ictal SPECT: qualitative and quantitative analysis. *Journal of Neurology, Neurosurgery & Psychiatry*, 66(3), 331-339.
- Onton, J., Westerfield, M., Townsend, J., & Makeig, S. (2006). Imaging human EEG dynamics using independent component analysis. *Neuroscience & Biobehavioral Reviews*, 30(6), 808-822.
- Oostenveld, R., Fries, P., Maris, E., & Schoffelen, J.-M. (2011). FieldTrip: open source software for advanced analysis of MEG, EEG, and invasive electrophysiological data. *Computational intelligence and neuroscience*, 2011, 1.
- Oostenveld, R., & Praamstra, P. (2001). The five percent electrode system for high-resolution EEG and ERP measurements. *Clinical neurophysiology*, 112(4), 713-719.
- Pascual-Marqui, R. D. (2002). Standardized low-resolution brain electromagnetic tomography (sLORETA): technical details. *Methods Find Exp Clin Pharmacol*, 24(Suppl D), 5-12.
- Pascual-Marqui, R. D., Michel, C. M., & Lehmann, D. (1994). Low resolution electromagnetic tomography: a new method for localizing electrical activity in the brain. *International Journal of psychophysiology*, 18(1), 49-65.
- Pascual-Marqui, R. D., Sekihara, K., Brandeis, D., & Michel, C. (2009). Imaging the electrical neuronal generators of EEG/MEG. In C. M. Michel (Ed.), *Electrical neuroimaging* (pp. 49-78). New York: Cambridge University Press, Cambridge, UK.
- Pelvig, D., Pakkenberg, H., Stark, A., & Pakkenberg, B. (2008). Neocortical glial cell numbers in human brains. *Neurobiology of aging*, 29(11), 1754-1762.
- Petros, N., Gwenaél, B., Francesca, P., M., M. C., Karl, S., Serge, V., . . . Margitta, S. (2017). Source localization of ictal epileptic activity based on high-density scalp EEG data. *Epilepsia*, 58(6), 1027-1036.
- Plummer, C., Harvey, A. S., & Cook, M. (2008). EEG source localization in focal epilepsy: where are we now? *Epilepsia*, 49(2), 201-218.
- Praveen, S., Michael, S., H., P. L., Martin, F., Guido, R., Birthe, P., . . . Sándor, B. (2018). Ictal and interictal electric source imaging in presurgical evaluation: a prospective study. *European Journal of Neurology*, 0(ja).

- Rankine, L., Stevenson, N., Mesbah, M., & Boashash, B. (2005). *A quantitative comparison of non-parametric time-frequency representations*. Paper presented at the Signal Processing Conference, 2005 13th European.
- Ray, A., Tao, J. X., Hawes-Ebersole, S. M., & Ebersole, J. S. (2007). Localizing value of scalp EEG spikes: a simultaneous scalp and intracranial study. *Clinical neurophysiology*, 118(1), 69-79.
- Raz, J., Turetsky, B., & Fein, G. (1988). Confidence intervals for the signal-to-noise ratio when a signal embedded in noise is observed over repeated trials. *IEEE Transactions on Biomedical Engineering*, 35(8), 646-649.
- Reyes, B., Charleston-Villalobos, S., Gonzalez-Camarena, R., & Aljama-Corrales, T. (2008). *Time-frequency representations for second heart sound analysis*. Paper presented at the Engineering in Medicine and Biology Society, 2008. EMBS 2008. 30th Annual International Conference of the IEEE.
- Riviere, D., Régis, J., Cointepas, Y., Papadopoulos-Orfanos, D., Cachia, A., & Mangin, J.-F. (2003). A freely available Anatomist/BrainVISA package for structural morphometry of the cortical sulci. *Neuroimage*, 19(2), e1825-e1826.
- Rodríguez-Rivera, A., Van Veen, B. D., & Wakai, R. T. (2003). Statistical performance analysis of signal variance-based dipole models for MEG/EEG source localization and detection. *IEEE Transactions on Biomedical Engineering*, 50(2), 137-149.
- Romero, S., Mañanas, M. A., & Barbanoj, M. J. (2008). A comparative study of automatic techniques for ocular artifact reduction in spontaneous EEG signals based on clinical target variables: a simulation case. *Computers in biology and medicine*, 38(3), 348-360.
- Rosenfeld, M., Tanami, R., & Abboud, S. (1996). Numerical solution of the potential due to dipole sources in volume conductors with arbitrary geometry and conductivity. *IEEE Transactions on Biomedical Engineering*, 43(7), 679-689.
- Rosenow, F., & Luders, H. (2001). Presurgical evaluation of epilepsy. *Brain*, 124(Pt 9), 1683-1700.
- Roth, B. J., Balish, M., Gorbach, A., & Sato, S. (1993). How well does a three-sphere model predict positions of dipoles in a realistically shaped head? *Electroencephalogr Clin Neurophysiol*, 87(4), 175-184.
- Safieddine, D., Kachenoura, A., Albera, L., Birot, G., Karfoul, A., Pasnicu, A., . . . Merlet, I. (2012). Removal of muscle artifact from EEG data: comparison between stochastic (ICA and CCA) and deterministic (EMD and wavelet-based) approaches. *EURASIP Journal on Advances in Signal Processing*, 2012(1), 127.
- Sarvas, J. (1987). Basic mathematical and electromagnetic concepts of the biomagnetic inverse problem. *Physics in Medicine and Biology*, 32(1), 11.
- Scherg, M. (1994). From EEG source localization to source imaging. *Acta Neurol Scand Suppl*, 152, 29-30.

- Scherg, M., & Von Cramon, D. (1985). A new interpretation of the generators of BAEP waves I–V: results of a spatio-temporal dipole model. *Electroencephalography and Clinical Neurophysiology/Evoked Potentials Section*, 62(4), 290-299.
- Schimpf, P., Haueisen, J., Ramon, C., & Nowak, H. (1998). Realistic computer modelling of electric and magnetic fields of human head and torso. *Parallel Computing*, 24(9), 1433-1460.
- Schneider, M. R. (1972). A multistage process for computing virtual dipolar sources of EEG discharges from surface information. *IEEE Transactions on Biomedical Engineering*(1), 1-12.
- Shattuck, D. W., & Leahy, R. M. (2002). BrainSuite: an automated cortical surface identification tool. *Medical image analysis*, 6(2), 129-142.
- Soldati, N., Calhoun, V. D., Bruzzone, L., & Jovicich, J. (2013). The use of a priori information in ICA-based techniques for real-time fMRI: an evaluation of static/dynamic and spatial/temporal characteristics. *Frontiers in human neuroscience*, 7, 64.
- Srinivasan, R., Tucker, D. M., & Murias, M. (1998). Estimating the spatial Nyquist of the human EEG. *Behavior Research Methods, Instruments, & Computers*, 30(1), 8-19.
- Stok, C. J. (1987). The influence of model parameters on EEG/MEG single dipole source estimation. *IEEE Transactions on Biomedical Engineering*(4), 289-296.
- Stolze, H., Klebe, S., Zechlin, C., Baecker, C., Friege, L., & Deuschl, G. (2004). Falls in frequent neurological diseases. *Journal of neurology*, 251(1), 79-84.
- Sweeney, K. T., Ayaz, H., Ward, T. E., Izzetoglu, M., McLoone, S. F., & Onaral, B. (2012). A methodology for validating artifact removal techniques for physiological signals. *IEEE transactions on information technology in biomedicine*, 16(5), 918-926.
- Sweeney, K. T., Ward, T. E., & McLoone, S. F. (2012). Artifact removal in physiological signals—Practices and possibilities. *IEEE transactions on information technology in biomedicine*, 16(3), 488-500.
- Tadel, F., Baillet, S., Mosher, J. C., Pantazis, D., & Leahy, R. M. (2011). Brainstorm: A User-Friendly Application for MEG/EEG Analysis. *Computational intelligence and neuroscience*, 2011, 13.
- Tarantola, A. (2005). *Inverse Problem Theory and Methods for Model Parameter Estimation*: Society for Industrial and Applied Mathematics (SIAM).
- Tenke, C. E., & Kayser, J. (2015). Surface Laplacians (SL) and phase properties of EEG rhythms: Simulated generators in a volume-conduction model. *International Journal of psychophysiology*, 97(3), 285-298.

- Thevenet, M., Bertrand, O., Perrin, F., Dumont, T., & Pernier, J. (1991). The finite element method for a realistic head model of electrical brain activities: preliminary results. *Clinical Physics and Physiological Measurement*, 12(A), 89.
- Thurman, D. J., Beghi, E., Begley, C. E., Berg, A. T., Buchhalter, J. R., Ding, D., . . . Epidemiology, I. C. o. (2011). Standards for epidemiologic studies and surveillance of epilepsy. *Epilepsia*, 52 Suppl 7, 2-26.
- Tsang, O., Gholipour, A., Kehtarnavaz, N., Gopinath, K., Briggs, R., & Panahi, I. (2008). *Comparison of tissue segmentation algorithms in neuroimage analysis software tools*. Paper presented at the Engineering in Medicine and Biology Society, 2008. EMBS 2008. 30th Annual International Conference of the IEEE.
- Urigüen, J. A., & Garcia-Zapirain, B. (2015). EEG artifact removal—state-of-the-art and guidelines. *Journal of neural engineering*, 12(3), 031001.
- Urrestarazu, E., Iriarte, J., Alegre, M., Valencia, M., Viteri, C., & Artieda, J. (2004). Independent component analysis removing artifacts in ictal recordings. *Epilepsia*, 45(9), 1071-1078.
- Valdes-Sosa, P., Marti, F., Garcia, F., & Casanova, R. (2000). Variable Resolution Electric-Magnetic Tomography. In C. J. Aine, G. Stroink, C. C. Wood, Y. Okada, & S. J. Swithenby (Eds.), *Biomag 96: Volume 1/Volume 2 Proceedings of the Tenth International Conference on Biomagnetism* (pp. 373-376). New York, NY: Springer New York.
- Van Oosterom, A. (1991). History and evolution of methods for solving the inverse problem. *Journal of Clinical Neurophysiology*, 8(4), 371-380.
- Vigario, R., & Oja, E. (2008). BSS and ICA in neuroinformatics: from current practices to open challenges. *IEEE Reviews in biomedical engineering*, 1, 50-61.
- Vigário, R. N. (1997). Extraction of ocular artefacts from EEG using independent component analysis. *Electroencephalogr Clin Neurophysiol*, 103(3), 395-404.
- Wallstrom, G. L., Kass, R. E., Miller, A., Cohn, J. F., & Fox, N. A. (2004). Automatic correction of ocular artifacts in the EEG: a comparison of regression-based and component-based methods. *International Journal of psychophysiology*, 53(2), 105-119.
- Wang, Y., & Gotman, J. (2001). The influence of electrode location errors on EEG dipole source localization with a realistic head model. *Clinical neurophysiology*, 112(9), 1777-1780.
- Waser, M., & Garn, H. (2013). *Removing cardiac interference from the electroencephalogram using a modified Pan-Tompkins algorithm and linear regression*. Paper presented at the Engineering in Medicine and Biology Society (EMBC), 2013 35th Annual International Conference of the IEEE.
- Wennberg, R., Valiante, T., & Cheyne, D. (2011). EEG and MEG in mesial temporal lobe epilepsy: where do the spikes really come from? *Clinical neurophysiology*, 122(7), 1295-1313.

- Xu, X.-L., Xu, B., & He, B. (2004). An alternative subspace approach to EEG dipole source localization. *Physics in Medicine and Biology*, 49(2), 327.
- Yang, L., Wilke, C., Brinkmann, B., Worrell, G. A., & He, B. (2011). Dynamic imaging of ictal oscillations using non-invasive high-resolution EEG. *Neuroimage*, 56(4), 1908-1917.
- Yvert, B., Bertrand, O., Echallier, J., & Pernier, J. (1995). Improved forward EEG calculations using local mesh refinement of realistic head geometries. *Electroencephalogr Clin Neurophysiol*, 95(5), 381-392.

University of Malaya

LIST OF PUBLICATIONS AND PAPERS PRESENTED

The following articles have been published/submitted in the journals indexed by Thomson Reuters Web of Science (WoS) and contributed toward achieving the research objectives:

- a) Habib, M. A., Ibrahim, F., Mohktar, M. S., Kamaruzzaman, S. B., Rahmat, K., & Lim, K. S. (2017). Recursive ICA-decomposition of ictal EEG to select the best ictal component for EEG source imaging. *Clinical Neurophysiology*. (Under Review, Tier-1 ISI, I.F-3.866, Publisher: Elsevier Inc.)
- b) Habib, M. A., Ibrahim, F., Mohktar, M. S., Kamaruzzaman, S. B., Rahmat, K., & Lim, K. S. (2015). Ictal EEG Source Imaging for Presurgical Evaluation of Refractory Focal Epilepsy. *World Neurosurgery*. (Published, Tier-1 ISI, I.F-2.878, Publisher: Elsevier Inc.)
- c) Habib, M. A., Mohktar, M. S., Kamaruzzaman, S. B., Lim, K. S., Pin, T. M., & Ibrahim, F. (2014). Smartphone-based solutions for fall detection and prevention: challenges and open issues. *Sensors*, 14(4), 7181-7208. (Published, Tier-1 ISI, I.F-2.245, Publisher: MDPI)

Furthermore, the following articles have been published in the international conference proceedings:

- a) Habib, M.A., Ibrahim, F., Mohktar, M.S., Kamaruzzaman, S.B., & Lim, K.S. (Dec. 2015) Effects of Coherent Noise on Ictal Component Selection for EEG source Imaging, in *International Conference for Innovation in Biomedical Engineering and Life Sciences (ICIBEL)*, Putrajaya, Malaysia. (Published, Indexed by ISI Proceedings of Thomson Reuters)

- b) Habib, M.A., Ibrahim, F., Mohktar, M.S., Kheng Seang Lim, & Kamaruzzaman, S.B. (Nov. 2014) A comparison of five free software solutions for generating realistic human head models from magnetic resonance imaging, *in 5th Brunei International Conference on Engineering and Technology (BICET 2014)*, Bandar Seri Begawan, Brunei. (Published, Indexed in IEEE Xplore Digital Library and IET Digital Library)

University of Malaya